Probing the Solar Corona at High Temporal and Spatial Resolution with the Low Frequency Array

A dissertation submitted to the University of Dublin
for the degree of Doctor of Philosophy

Pearse Murphy, B.A. (Mod.)
School of Physics, Trinity College Dublin

Supervisor:
Prof. Peter T. Gallagher
Co-Supervisor:
Dr. Eoin P. Carley

April 2022

Trinity College Dublin
Coláiste na Tríonóide, Baile Átha Cliath
The University of Dublin

Declaration

I agree to deposit this thesis in the University's open access institutional repository or allow the Library to do so on my behalf, subject to Irish Copyright Legislation and Trinity College Library conditions of use and acknowledgement.

I consent to the examiner retaining a copy of the thesis beyond the examining period, should they so wish (EU GDPR May 2018).

Name: Pearse Murphy

Signature: ..... **Date:** 13/04/2022

Summary

The solar corona is the outermost layer of the Sun's atmosphere. Advancements in radio astronomy over the last 50 years have revealed a number of radio phenomena which occur in the corona each with different temporal and spectral characteristics. Current generation interferometers such as the LOw Frequency ARray (LOFAR) give an unprecedented insight into the fine spatial, spectral and temporal structure of these radio bursts. Of particular interest are what are known as type III radio bursts, which are indicative of electrons propagating along open magnetic field lines in the solar corona. Observations of type III bursts allow for the remote sensing of the plasma at various heights in the corona due to the relation between emission at the plasma frequency and electron density. High spatial resolution observations of radio bursts give insight into the role of radio wave scattering on the observed source sizes while high temporal and spectral resolution observations can be used to determine the power density of electron density fluctuations in the corona.

Key results of this thesis come from observations of solar radio emission at the highest temporal, spectral and spatial resolutions to date. Firstly, the REALtime Transient Acquisition backend (REALTA) was developed and installed at the Irish LOFAR station (I-LOFAR) to record the raw voltages from the station at 5.12μs temporal resolution. This is among the most advanced data acquisition clusters installed at an international LOFAR station to date. First light observations from REALTA are shown, including a variety of solar radio bursts showcasing fine temporal and spectral structure. The installation of REALTA allows for observations of solar radio bursts at some of the highest temporal resolutions to date and is a key resource in investigating the fine temporal structure of solar radio emission.

Secondly, a new technique was implemented to directly measure the size of radio bursts from their interferometric visibilities. This is the first time that such a technique has been used to study a type IIIb radio burst. Spectroscopic analysis of the fine frequency structure of a type IIIb burst is used to calculate an expected a source size of 3.18 arcsec. The full width at half maximum height (FWHM) along the major and minor axes of the burst at 34.76 MHz is found to be 18.8 $\pm$ 0.1 arcmin and 10.2 $\pm$ 0.1 arcmin respectively. The new fitting technique used in this analysis removes the need for interferometric imaging and as such, these results indicate that the large size observed for the type IIIb radio burst is due to radio wave scattering in the corona. It is also determined that this effect may be over estimated by previous tied array imaging observations.

Finally, this technique was utilised to determine the size and shape of 29 type III bursts and compare them to predictions from state-of-the-art radio wave scattering simulations. It is found that these bursts have a mean size along the major and minor axis of $\mathrm{FWHM_x} = 16.27$ arcmin and $\mathrm{FWHM_y} = 11.96$ arcmin respectively. No trend of source size with respect to helioprojective longitude

is found, which is in contrast to predictions from modelling of anisotropic scattering from a point source. I attribute this discrepancy to an intrinsic source size of type III bursts. These results underscore the necessity for thorough comparison between radio observations and radio wave scattering simulations before one can be used to infer information from the other.

I highlight some future work that could be built upon the research presented in this thesis to further advance the knowledge of radio wave generation and propagation in the solar corona.

For my grandparents.

Acknowledgements

I would firstly like to thank my supervisors Peter Gallagher and Eoin Carley. Your guidance and support throughout my PhD has been constant and has saved me from sounding foolish on more than one occasion. It has been a pleasure working with you both over the last four years.

Operations at I-LOFAR, and my understanding thereof, would not be where they are today without Joe McCauley. Thank you for always being on hand to troubleshoot failed observations.

Brian Coghlan was an invaluable resource during the installation of REALTA and the development of recording data from the Transient Buffer Boards at I-LOFAR. I am grateful for your patience while I was finding my feet as a PhD student.

I want to express my gratitude to Sophie Murray and Shane Maloney. You've opened my eyes to the wonderful world of open source software and "basic version control techniques". Thank you, also, for many great ideas from many long group meetings.

I have been incredibly lucky to spend some of my time as a PhD student in a place as steeped in myth as the astrophysics student office at Trinity College Dublin. Here I met some amazing people who I am truly honoured to call friends. Laura Hayes and Aoife McCloskey, you are both everything I aspire to be as a scientist and as a person. Thank you for making me feel welcome from the moment I first walked into the office. Dúalta Ó Fionnagáin and Ioana Boian, I still find it hard that I don't see you every day. Thank you both for many geography quizzes and to Dúalta in particular for getting me interested in, and subsequently losing money to, cryptocurrencies. To Rob Kavanagh, Stephen Carolan, Eoin Farrell and Amanda Mesquita. Although our time together was cut short by a move to a new institute you are all part of the many great memories I made throughout the last four years. To Tadhg Garton, thank you for being a wall to bounce ideas off and introducing me to your slightly worrying sense of humour/coping mechanism.

During my PhD I have had the fortune to share my time with many wonderful people at the Dublin Institute for Advanced Studies (#DIASDiscovers). There are too many to name but I'm going to try anyway. Alberto, Anton, David, Eoin, Jeremy, Johnny, Maria K, Maria M, Mario, Ruben, Sam and Shilpi.

I started this PhD in the company of four people who have made the last four years incredibly enjoyable. Laura Murphy, Brendan Clarke, Aoife Ryan and Ciara Maguire, sharing this journey with you has been a blessing. I

don't know how I would have made it this far without you all, thank you. In particular I want to thank Aoife and Ciara for answering my almost constant stream of questions about radio interferometry and for putting up with impromptu drum solos on my desk.

My thanks also go to Conor, Marlon, John, Dan, the former residents of 40 Greenmount Road and the Mullinguardians of the Galaxy.

To my family Noel and Siobhan, Conor and Éadaoin. Thank you for everything. Your love and support has brought me to where I am today and I am eternally grateful for that.

Finally I want to say thank you to Camille Stock. Despite having written tens of thousands of words to describe solar radio physics, I don't know what to say to express how much you mean to me. In the most bleak moments of writing this thesis you have picked me up off the floor both metaphorically and literally. I am incredibly lucky to be loved by someone as generous, kind and caring as you. Thank you.

List of Publications

Publications

1. Corentin K. Louis, Caitriona M. Jackman, Jean-Mathias Griessmeier, Olaf Wucknitz, David. J. McKenna, **Pearse C. Murphy**, Peter T. Gallagher, Eoin Carley, Dúalta Ó Fionnagáin, Aaron Golden, Joe McCauley, Paul Callanan, Matt Redman, Christian Vocks.
"Observing Jupiter's radio emissions using multiple LOFAR stations: a first case study of the Io-decametric emission using the Irish IE613, French FR606 and German DE604 stations"
Royal Astronomical Society Techniques and Instruments journal (2021 submitted)

2. **P. C. Murphy**, P. Callanan, J. McCauley, D. J. McKenna, D. Ó Fionnagáin, C. K. Louis, M. P. Redman, L. A. Cañizares, E. P. Carley, S. A. Maloney, B. Coghlan, M. Daly, J. Scully, J. Dooley, V. Gajjar, C. Giese, A. Brennan, E. F. Keane, C. A. Maguire, J. Quinn, S. Mooney, A. M. Ryan, J. Walsh, C. M. Jackman, A. Golden, T. P. Ray, J. G. Doyle, J. Rigney, M. Burton, P. T. Gallagher.
"First Results from the REAL-time Transient Acquisition backend (REALTA) at the Irish LOFAR station",
Astronomy and Astrophysics Volume 655, A16 (2021)

3. A. M. Ryan, P. T. Gallagher, E. P. Carley, M. A. Brentjens, **P. C. Murphy**, C. Vocks, D. E. Morosan, H. Reid, J. Magdalenic, F. Breitling, P. Zucca, R. Fallows, G. Mann, A. Kerdraon, R. Halfwerk.
"LOFAR imaging of the solar corona during the 2015 March 20 solar eclipse",
Astronomy and Astrophysics, Volume 648, A43 (2021)

4. **Pearse C. Murphy**, Eoin P. Carely, Aoife Maria Ryan, Pietro Zucca, Peter T. Gallagher.
"LOFAR Observations of Radio Burst Source Sizes and Scattering in the Solar Corona",
Astronomy and Astrophysics, Volume 645, A11 (2021)

5. Vishal Gajjar, Andrew Siemion, Steve Croft, Bryan Brzycki, Marta Burgay, Tobia Carozzi, Raimondo Concu, Daniel Czech, David DeBoer, Julia DeMarines, Jamie Drew, J. Emilio Enriquez, James Fawcett, Peter Gallagher, Michael Gerret, Nectaria Gizani, Greg Hellbourg, Jamie Holder, Howard Isaacson, Sanjay Kudale, Brian Lacki, Matthew Lebofsky, Di Li, David H. E. MacMahon, Joe McCauley, Andrea Melis, Emilio Molinari, **Pearse Murphy**, Delphine Perrodin, Maura Pilia, Danny C. Price, Claire Webb, Dan Werthimer, David Williams, Pete Worden, Philippe Zarka, and Yunfan Gerry Zhang.
"The Breakthrough Listen Search for Extraterrestrial Intelligence ",

Astro2020: Decadal Survey on Astronomy and Astrophysics, APC white papers, no. 223; Bulletin of the American Astronomical Society, Vol. 51, Issue 7, id. 223 (2019)

6. David M. Long, **Pearse C. Murphy**, Georgina Graham, Eoin P. Carley, David Pérez-Suárez.
"A Statistical Analysis of the Solar Phenomena Associated with Global EUV Waves",
Solar Physics, Volume 292 , Issue 185, (2017).

Contents

List of Figures

List of Tables

1

Introduction

Ancient passage tombs in Ireland show evidence that thousands of years ago, humans had an understanding of the movement of the Sun in the sky at different times of the year. These tombs are constructed such that only on the day of a solar solstice or equinox, is the passageway illuminated in full. Today the Sun is still a source of curiosity and has more than once shown that us humans are not the centre of the universe. The light and heat from the Sun are the essential source of energy for life on our planet however, our proximity to this star also comes with a risk. Explosive and energetic events such as coronal mass ejections and solar flares occur with varying frequency and intensity over the course of an eleven year cycle. Their effects on Earth were made known in a spectacular fashion in 1859 with the so called *Carrington Event*. This was a solar eruptive event, the magnitude of which has not been seen in the subsequent 162 years. It induced currents into telegraph wires causing them to operate even though they had been removed from a power source. It also caused aurorae to be seen as close to the equator as Cuba and bright enough at higher latitudes that a newspaper could be read at night time under their light.

The Sun emits across the electromagnetic spectrum, however the focus of this thesis is low frequency radio waves. Similar mechanisms that drive large energy releases like the Carrington Event also generate radio wave emission in the form of solar radio bursts. These solar radio bursts can be used as a remote diagnostic of the Sun's atmosphere and to determine physical processes in plasma in the outer layers of the solar atmosphere. This chapter highlights some fundamental concepts of solar physics, different types of radio emission from the Sun and the implications of their study.

1.1 The Sun

The Sun is our nearest star and the centre of our solar system however, apart from these distinctions it is an average star. It is a G2 type star located on the main sequence of the

Hertzsprung Russell diagram. It has a luminosity of $(3.83 \pm 0.04) \times 10^{26}$ W and a radius $R_\odot = (6.959 \pm 0.007) \times 10^8$ m (Foukal, 2013). The Sun's mass of $(1.9889 \pm 0.0003) \times 10^{30}$ kg comprises $> 99\%$ of the solar system's total mass (Foukal, 2013). At the time of writing, the Sun is ~ 5 billion years old. Formed from a cooling cloud of gas and dust 4.6 billion years ago, the Sun now has a core with a temperature of 15 MK. This temperature is hot enough for nuclear fusion to occur and will continue to do so until the Sun's supply of hydrogen runs out. The Sun will remain on the main sequence for a further ~ 5 billion years before expanding into a Red Giant.

Due to our proximity to the Sun, we are able to observe a vast array of phenomena, many of which have direct terrestrial impacts. These phenomena take place in the solar atmosphere and shall be described briefly below. The study of these phenomena is a study of the plasma and magnetic field structure of the solar atmosphere and gives insights into energy generation and transport.

1.1.1 The Photosphere

The layer of the Sun at 1 $R_\odot$ is known as the photosphere and is what would be called the surface of the Sun. The temperature of the photosphere, alternatively the surface temperature of the Sun, is ~ 6000 K and has a number density of the order of 10^{17}cm^{-3}, at which point the mean free path of visible photons becomes much greater than the distance between the Sun and the Earth and can be thought as coming directly from the solar surface.

The most distinct feature of the photosphere in white light are sunspots. Sunspots are seen as dark regions in the photosphere and are the manifestation of of solar activity. Sunspot magnetic fields are much stronger than the surrounding magnetic field of the photosphere and as such, inhibit heat transfer. This means that sunspots are cooler ~ 4200 K (McLean & Labrum, 1985) than the surrounding plasma.

Above the photosphere the temperature and density profile change dramatically, see Figure 1.1, throughout the remaining layers of the Sun's atmosphere; the chromosphere, the transition region and the corona.

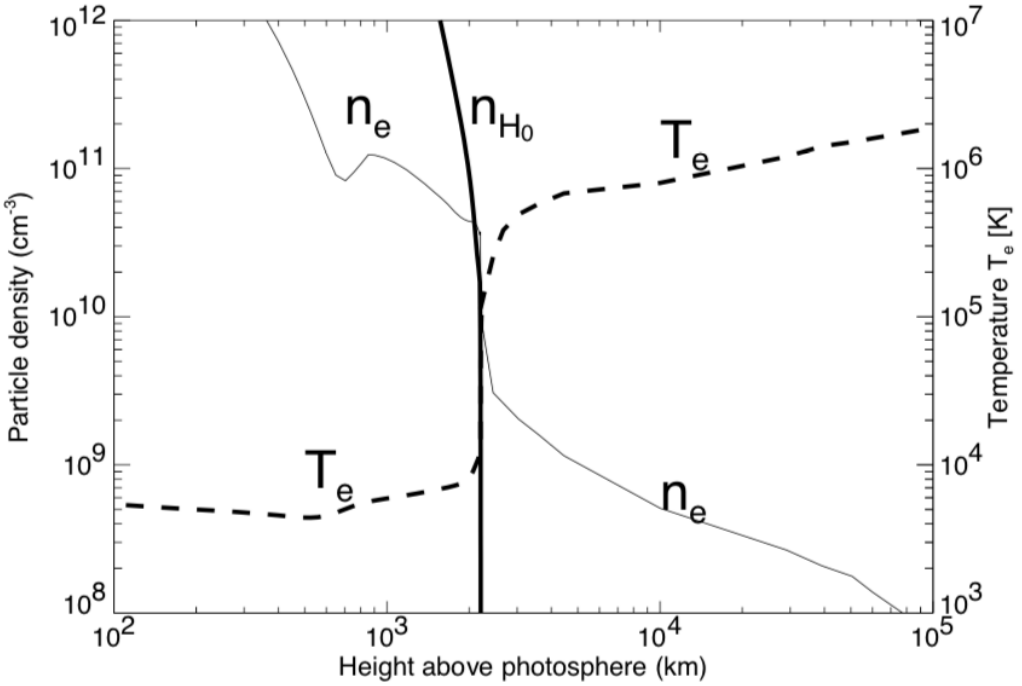

Figure 1.1: Model of electron density and temperature with height in the solar atmosphere. The x axis shows height above the chromosphere in kilometres while the y axes show particle density in cm^{-3} and temperature in Kelvin. The chromosphere begins ~ 500 km above the photosphere. The region around 2000 km showing a sharp rise in temperature and sharp fall in electron density is known as the transition region. Above this height plasma becomes fully ionised and is known as the corona. Image from Aschwanden (2004).

1.1.2 The Chromosphere

In traditional plane-parallel models, the chromosphere extends to $\sim$ 2000 km above the photosphere. Its name is derived from the Greek word for colour, $\chi\rho\omega\mu\alpha$ (*chroma*), in reference to the red-coloured rim visible during solar eclipses. This red colour originates from the dominant hydrogen-α (Hα) transition at 656.3 nm. Temperatures in the chromosphere show a decrease with distance to a local minimum of $\sim$ 4400 K at $\sim$ 500 km above the photosphere. The temperature then rises again to a maximum of $\sim 20,000$ K at its upper boundary. These temperatures are low enough that most of the hydrogen in the chromosphere remains neutral.

The chromosphere exhibits numerous structures and dynamics often observed in emission lines such as Hα, the Ca II H and K lines and the Lyman-α transition of hydrogen. The most prominent structural features of the quiet chromosphere include the chromospheric network on the disk and small, almost ubiquitous, jets of plasma known as spicules on the limb. The chromospheric network forms along the boundaries of supergranular cells where magnetic fields are concentrated. The magnetic field strength in the network can reach hundreds of millitesla although the average field strength of the chromosphere is $\sim$ 3 mT (McLean & Labrum, 1985).

1.1.3 The Transition Region

The transition region occurs between the chromosphere and corona. Rather than a geometric layer, it is more accurate to consider the transition region as the region where the temperature rapidly increases (over distances as short as $\sim$ 100 km) from $\sim 20,000$K to $\sim$ 0.8 MK. Because the pressure remains approximately constant over this distance, the electron number density drops dramatically as is shown in Figure 1.1. The transition region is also the part of the solar atmosphere where plasma changes from being partially ionised and collisionally dominated to fully ionised and collisionless. Network structures are also visible in low transition region images and are generally larger than those of the chromosphere, suggesting an expansion of magnetic flux tubes

with height. However, the network completely disappears in higher altitude images hence, the magnetic field structure transitions from being ordered in the chromosphere to being extremely complex in the corona (Tian, 2017). Emission from the transition region is predominantly in the ultraviolet and extreme ultraviolet.

1.1.4 The Corona

The outermost layer of the solar atmosphere is called the corona. It contains hot, tenuous, inhomogeneous and time-varying plasma which extends from the top of the transition region into interplanetary space. The electron density in the corona ranges from 10^9 cm^{-3} at the base to 10^6 cm^{-3} at distances of 1 R$_\odot$ from the solar surface. Densities vary throughout the corona. Sparse, underdense regions at the base of the corona known as coronal holes exhibit densities of $\sim (0.5 - 1.0) \times 10^8$ cm^{-3} whereas areas of high magnetic activity known as active regions have electron densities of $\sim 2 \times 10^9$ cm^{-3} (Aschwanden, 2004). Active regions are the coronal counterpart to sunspots and are best seen in EUV images of the Sun. The complex magnetic fields in active regions drive many of the solar phenomena such as solar flares and coronal mass ejections (CMEs).

Observing the white light corona is done with a number of ground-based and space-based instruments called coronagraphs, that emulate the effect of a total eclipse. The Large Angle and Spectrometric Coronagraph (LASCO; Brueckner et al., 1995) on board the Solar and Heliospheric Observatory (SOHO) is one such instrument and allows the corona to be observed from distances of 2-32 R$_\odot$. The corona is also observed in extreme ultraviolet (EUV) lines, soft X-rays and at radio wavelengths. Observations at various wavelengths show a plethora of structure in the corona both on disk and on the limb that exist on varying time scales of a few minutes to a number of days. All particle acceleration events that produce radio emission of interest to this thesis occur in the solar corona. Figure 1.2 shows the corona and other layers of the solar atmosphere observed with the Atmospheric Imaging Assembly (AIA; Lemen et al., 2012).

The sun observed at low radio frequencies looks different to that in EUV images,

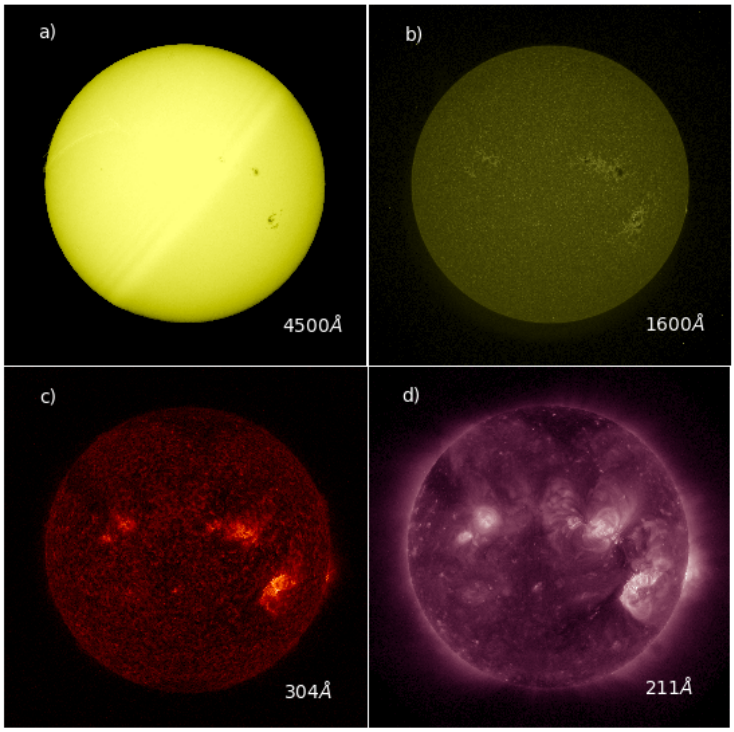

Figure 1.2: The Sun observed with AIA in four different wavelengths and thus in four different layers of its atmosphere. Panel a shows the photosphere at 4500Å, a group of sunspots is visible towards the southwestern limb of the sun. Panel b shows the chromosphere at 1600Å and exhibits the chromospheric network. Panel c shows the upper chromosphere and transition region at 304Å. Panel d shows the upper corona at 211Å the active region is noticeable as the bright region in the same location as the sunspot group as in panel a.

mostly due to the reduced spatial resolution of radio images. However, some key features of the solar corona are still seen in radio image, as depicted in Figure 1.3. Here the contours show radio emission between 140 and 160 MHz and are overlaid on a 193Å image taken with AIA. The peak in the contours is seen to overlap with a small active region while coronal holes show no radio emission.

The high temperature of the corona remains one of the greatest mysteries in all of solar physics. Energetic events in the corona such as solar flares and CMEs, described in 1.2 and 1.3, are observed across the electromagnetic spectrum. They are studied in order to understand how particles are accelerated, how energy is released and ultimately, why the corona has such an unaccountably high temperature.

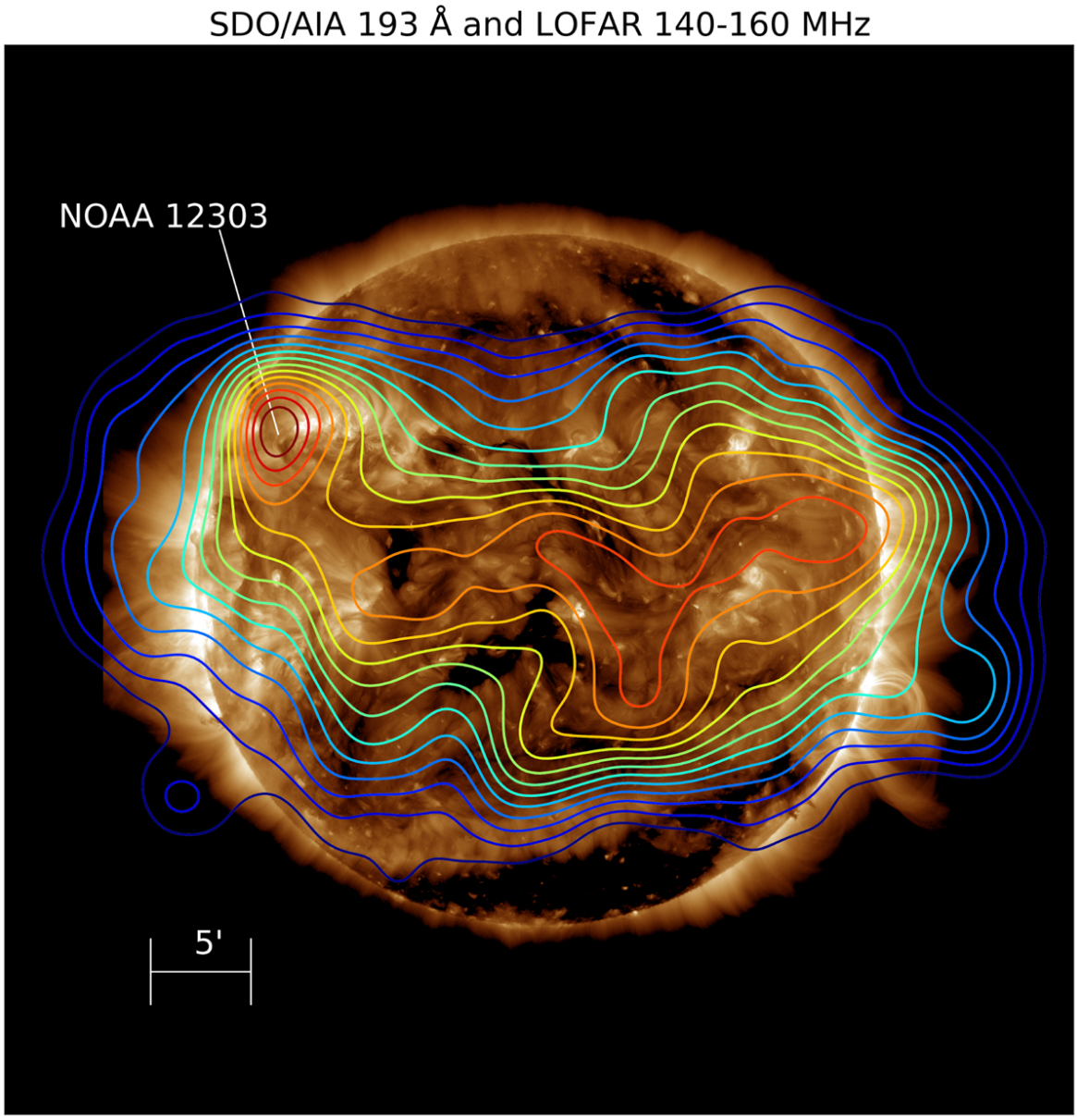

Figure 1.3: The solar corona observed at low radio frequencies overlayed on a 193 Å AIA image of the corona. The contours show the radio emission tracing out features in the solar corona, e.g. and intense peak above an active region and no emission around coronal holes. Image from Ryan et al. (2021).

1.1.5 The Plasma Beta Parameter

The plasma beta parameter is effectively a ratio of pressure due to the plasma and the magnetic field pressure. It is given, in SI units, as

$$\beta = \frac{nk_BT}{B^2/2\mu_0} \tag{1.1}$$

where n is the electron density, k_B is the Boltzmann constant, T is the plasma temperature, B is the magnetic field strength and μ_0 is the permeability of free space. Using values of n and T from Figure 1.1 and typical values for the magnetic field strength in the chromosphere ($\sim$ 100 G) and corona ($\sim$ 10 G) we can see that the value for β changes from values > 1 in the chromosphere to < 1 in the corona. In low β environments the magnetic pressure dominates and plasma is confined along magnetic field lines. It is for this reason that the magnetic field structure of the solar corona gives rise to acceleration events in energetic phenomena such as solar flares and coronal mass ejections.

1.2 Solar Flares

Solar flares are massive releases of magnetic energy commonly believed to be due to a reconfiguration in the complicated magnetic field structure in an active region. They are some of the most energetic events in the solar system, releasing $\sim 10^{25}$ J of energy over a matter of minutes. Flares are observed across the electromagnetic spectrum from radio waves to γ rays with energies > 10 MeV. They are classified by the amount of X-ray flux (W m^{-2}) detected by the Geostationary Operational Environmental Satellite (GOES) 1-8 Å band on a logarithmic scale as being A, B, C, M or X class with A being the lowest flux (10^{-8} W m^{-2}) and X the highest (10^{-4} W m^{-2}). Each class is further subdivided into a linear scale. A timeseries of X-ray flux from a solar flare is often called a lightcurve and has three characteristic phases; a pre-flare phase which shows X-ray flux associated with the active region where the flare occurs, an impulsive

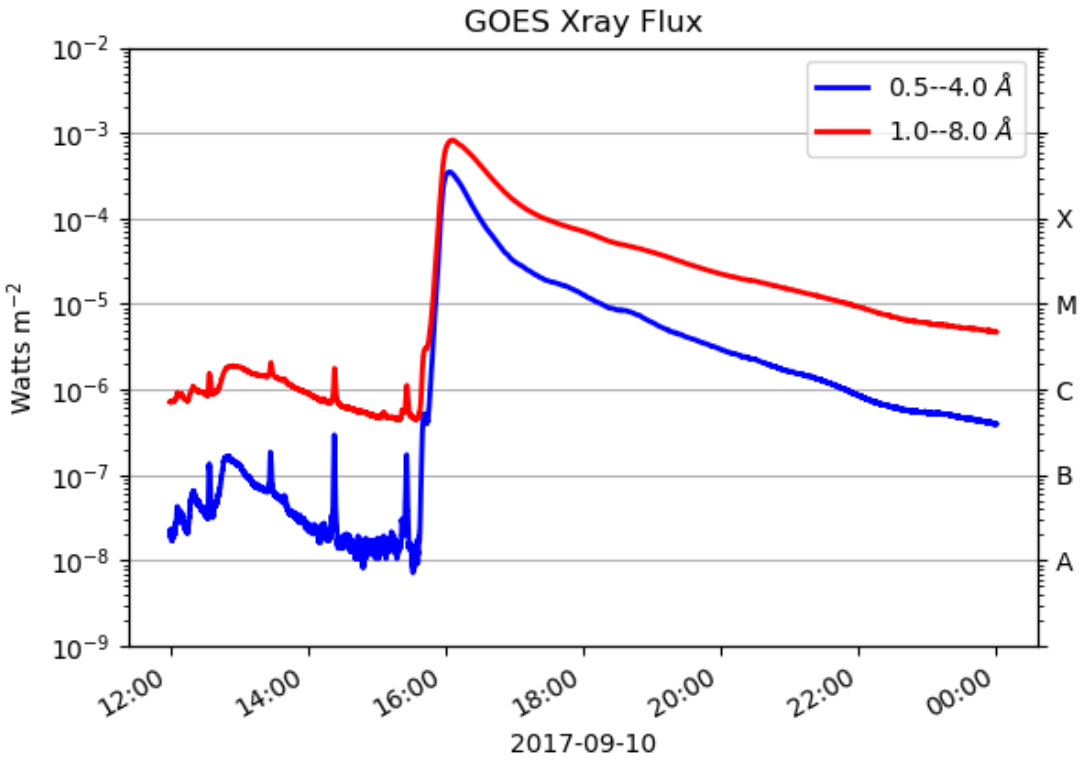

Figure 1.4: The GOES lightcurve of the X9 flare that occurred on 10 September 2017. The x axis indicates the time of day on 10 September 2017 while the y axes show the X-ray flux in Wm^{-2} and the flare classification. The red curve shows the 1-8 Å channel by which the flare is classified while the blue curve shows the 0.5-4 Å band. The three characteristic phases of a solar flare are clearly displayed here. The pre-flare phase before $\sim$ 16:00 UTC, the impulsive phase indicated by the sharp rise in flux and the gradual decay phase where X-ray flux gradually returns to the pre-flare level.

phase showing a sharp rise in X-ray flux corresponding to accelerated particles colliding with the solar surface, and a gradual decay phase where plasma heated by the flare gradually cools back to its pre-flare state. Figure 1.4 shows a GOES light curve of the X9 class flare that occurred on 10 September 2017 and the three flare phases described above.

During solar flares, magnetic structures known as coronal loops fill with hot plasma and begin to emit in soft X-rays. At the same time, electrons are accelerated towards the solar surface where their energy is converted to hard X-rays in the collision via bremsstrahlung.

1.3 Coronal Mass Ejections (CMEs)

In certain magnetic reconnection events, plasma suspended in a magnetic flux rope erupts from the corona into the heliosphere, the volume around the Sun where the interplanetary medium is dominated by particles flowing outward from the Sun. These eruption events are known as coronal mass ejections and accelerate 10^{15} g of charged particles at typical speeds of up to ~ 2500 km s^{-1} (Gopalswamy & Thompson, 2000). A "textbook" CME structure consists of a bright front that surrounds a dark cavity and a bright central core. CMEs are observed using coronagraphs as they are much fainter than the solar disk. An example of a CME observed using the LASCO C2 corona with a field of view from 1.5 $R_\odot$ to 6 $R_\odot$ can be seen in Figure 1.5. Ejected material from a CME can interact with the Earth's magnetosphere and is known to have caused adverse effects including satellite communication disruption, radio blackouts, widespread power outages and large inaccuracies in GPS postions (Eastwood et al., 2017). CMEs can travel faster than the local Alfvén speed in the corona leading to a shock which can accelerate particles.

1.4 Solar Radio Bursts

In 1942 while Britain was monitoring radar signals for the signs of enemy aircraft, a strong, noise-like and highly variable signal was noticed by radar operators. Upon investigation it was found that this jamming was in fact radio emission from the Sun. The discovery of this radio emission being associated with a major solar flare was kept secret until after the war and was published by Appleton & Hey (1946). Since then the field of solar radio astronomy has flourished and significant advancements in both instrumentation and theory have occurred. Worldwide, radio interferometers such as the LOw Frequency ARray (LOFAR; van Haarlem et al., 2013) and the Murchison Widefield Array (MWA; Lonsdale et al., 2009) have been built while next generation interferometers like the Square Kilometre Array (SKA; McMullin et al., 2020) are

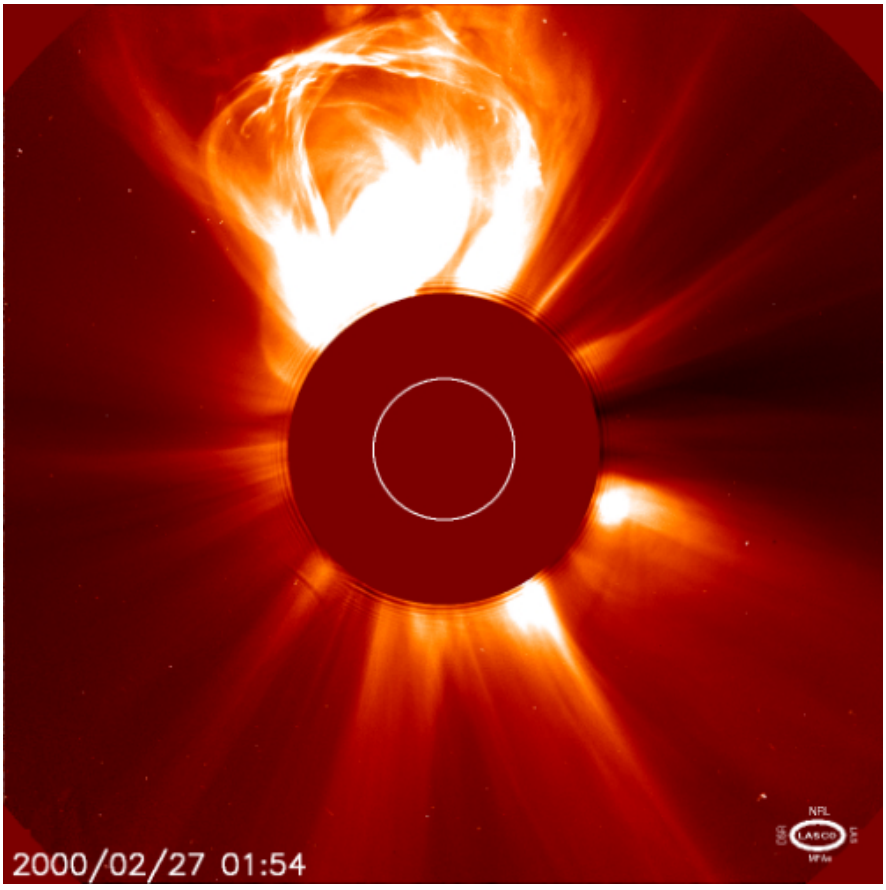

Figure 1.5: A coronal mass ejection (CME) observed with the LASCO C2 coronagraph on 27 February 2000. The area covered by the coronagraph is shown in the red disk in the centre of the image and the white circle represents the solar disk. The bright feature in the top of the image is the CME while less bright structures known as streamers are also seen.

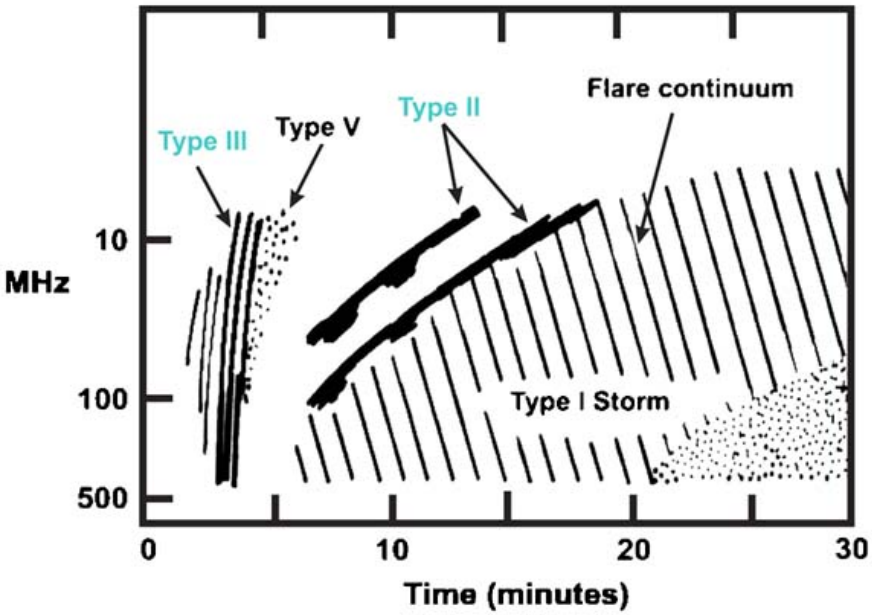

Figure 1.6: A cartoon of type I-V radio bursts. The x axis shows the time scale of the various bursts which can range from less than 1 minute to greater than 10 minutes. The y axis shows the typical frequency range of the bursts. The different drift rates of the different burst types are apparent. Image from Cliver & Ling (2009).

slowly being brought online. These telescopes offer a dramatic improvement on the spectral resolution and imaging capability of those that were first used to study solar radio emission.

Solar radio emission often comes in the form of bursts of varying time scales. These were initially classified into three types by Wild & McCready (1950) with a fourth and fifth type being discovered by Boischot (1957) and Wild et al. (1959) respectively. A wealth of other fine structure radio bursts are also observed, predominantly found in radio storms such as S bursts, drift pairs and stria (McConnell, 1980; Melrose, 1982; Nelson & Melrose, 1985). The fine structure of these bursts can often reveal information about small-scale turbulence in the corona (Reid & Kontar, 2021). Figure 1.6 shows a schematic of the five "classic" types of solar radio burst. A brief description of some solar radio phenomena is given below.

Type I bursts Type I emission can appear as bursts and/or a continuum originating from "storm centres" that are associated with active regions. Type I storms can last for many days. Emission from type I bursts is highly circularly polarised in the o-mode

(whereby light is circularly polarised in the opposite direction as electrons are gyrating about a magnetic field line) and is also particularly directional with an increase in intensity as active regions rotate to the centre of the disk. Unlike type II or III bursts, they do not exhibit a harmonic structure (McLean & Labrum, 1985).

Type II bursts Type II radio bursts are a form of radio emission seen from the Sun and are identified by a slow ($\sim$ 0.1 MHz s^{-1}) drift to lower frequencies in dynamic spectra. The frequency drift can be used to find the velocity of the shock causing a burst if the electron number density as a function of height is known. The velocities of type II bursts are often found to be $\sim$ 1000 km s^{-1}, which is faster than the Alfvén velocity in the quiet corona meaning a shock must be present (Nelson & Melrose, 1985). Other basic properties of type II bursts include:

1. Narrow bandwidths of up to $\sim$ 100 MHz from initial to final frequencies.

2. A harmonic structure of two bands with a frequency ratio slightly less than 2:1 at a fundamental, f_p, and harmonic, $2f_p$, frequency can be seen for most type II bursts. This structure is consistent with the idea that type II emission is due to plasma oscillations.

3. A large number of type II bursts contain band splitting into an upper and lower band for each of the harmonics in their spectra. The cause for this splitting is not fully understood but it is commonly thought that the two bands are related to emission upstream and downstream of the MHD shock front which causes the type II burst (Smerd et al., 1974; Nelson & Melrose, 1985; Vršnak et al., 2002).

4. Herringbone structure. Approximately 20% of type II bursts show a herringbone structure of rapidly drifting emission spikes shooting out of the "backbone" of the main frequency drift to higher and lower frequencies. These herringbones are thought to be due to electron beams being accelerated at the associated shock for the type II burst (Mann, 1995). While the backbone is poorly polarised, the herringbones have been found to be quite strongly ($\sim$ 70%) polarised. The level

of polarisation of herringbones determined by Suzuki et al. (1980) are similar to those of type III bursts. They suggest that this is evidence that herringbone structure is due to plasma emission from accelerated electron beams such as in the case of type III bursts.

5. Starting emission frequencies of the order of a few 100 MHz ending at frequencies above 20 MHz. This being said, type II bursts with starting frequencies of $\sim$ 100 kHz have also been observed. These lower frequency bursts are thought to be due to interplanetary shocks whereas higher frequency bursts are considered to be from shocks in the low corona.

6. Typical durations of 5-15 minutes. type II bursts that occur after a flare do so with a delay ranging from 2-20 minutes. Bursts with shorter durations generally have higher starting frequencies.

Based on these and a number of other properties discussed in greater detail by Nelson & Melrose (1985), type II radio bursts can be used as indicators for MHD shocks in the solar corona. Observational proof of frequency varying inversely with time in the solar wind, consistent with radiation being generated at f_p and $2f_p$ directly upstream from a CME-driven shock, was found by Reiner et al. (1997) and solidifies this argument.

Type III burst Observations of type III radio bursts (and their sub-categories) are of particular interest to this thesis and, as such, are described in Section 1.4.1.

Type IV burst Type IV bursts come in at least three sub-types with the general characteristic that they are of the from of broadband emission lasting for several hours. Early stationary type IV bursts (also known as the flare continuum) associated with the decay phase of solar flares, late stationary bursts which appear similar to type I emission, and moving type IV bursts which exhibit a smooth, wide-band spectrum (McLean & Labrum, 1985).

Type V burst The last of the broadband emission bursts, type V radio bursts typically have a duration of 1-3 minutes and appear as an afterglow from type III bursts. Type V emission is strictly less than 150 MHz and is accepted that it results from electrons that generate a type III burst and become trapped in a closed magnetic loop in the corona (McLean & Labrum, 1985).

Fine Structure: S bursts S bursts, initially called Fast Drift Storm (FDS) bursts, were first observed at the Culgoora Solar Observatory in 1967 (Ellis, 1969) They were later renamed by McConnell (1980) who likened them to Jovian S bursts. They have a narrow bandwidth of the order of 0.03 MHz and a drift rate of 1-2 MHz s^{-1} and durations much less than 1s. McConnell (1980) also concluded that S bursts are radiated at either the plasma frequency or its harmonic in a manner similar to type III bursts but that the implications of S burst fine structure and coronal scattering can only be defined once it is determined which harmonic of the plasma frequency they are radiated at. Melnik et al. (2010a) propose a model of S bursts being generated by coalescence of fast magnetosonic waves with Langmuir waves which agrees well with the analysis of Clarke et al. (2019). Modern observations of S bursts, such as those conducted using LOFAR's tied-array imaging mode (Morosan et al., 2015), can give greater insight into the spectral and temporal variability of S bursts and what this might mean for the environment they are generated in.

The spatial extent and fine spectral structure of type III radio bursts are the main focus of this thesis. In Section 1.4.1 below I outline the physical characteristics of type III bursts and their subcategories.

1.4.1 Type III Bursts

Type III bursts are possibly the most useful radio burst for studying properties of plasma in the corona. As we shall see, they offer a remote measurement of the plasma density of the region where they are emitted. This allows us to probe the solar corona

plasma using any of the many radio telescopes on Earth dedicated to solar radiophysics (e.g. Benz et al., 2005). Reid & Ratcliffe (2014) review the observational properties of type III bursts which are repeated in brief here. The defining characteristic of type III bursts is a drift from high to low frequencies in a dynamic spectrum. The drift rates for type III bursts are typically quite fast, of the order of ~ 10 MHz s^{-1} depending on the frequency. The frequency drift rate, df/dt, has been found to have various relations with frequency (Reid & Ratcliffe, 2014) but most agree that $df/dt \propto f^{\alpha}$, where α ranges in the literature from ~ 1 to ~ 2.7.

Ginzburg & Zhelezniakov (1958) proposed that type III bursts are emitted at the plasma frequency,

$$\omega_p^2 = \frac{N_e e^2}{m_e \varepsilon_0} \tag{1.2}$$

where N_e is the number density of electrons, m_e is the electron mass, e is the electron charge and ε_0 is the permittivity of free space. A more detailed description of the plasma emission process is given in Section 2.3. Although Eq. 1.2 is relatively simple, it contains an important relationship in plasma physics. Namely, the plasma frequency is proportional to the square root of the electron density. This means that plasmas at higher electron densities will oscillate at higher frequencies than those of lower densities. The drift in type III bursts, which are emitted at ω_p, is therefore an indication of the emission source moving from an area of high electron density to low density, i.e. from the lower to the upper corona. Using a model of electron density in the corona such as the Newkirk (1961) model, it can be inferred that the exciter of type III bursts has a speed of ~ 0.3 c.

Type III bursts are observed to be in two bands, a fundamental and harmonic band that are emitted at ω_p and $2\omega_p$ respectively. Both bands exhibit the same frequency drift although the flux of the harmonic band is usually less than that of the fundamental band (Wild et al., 1954; McLean & Labrum, 1985). The process of plasma emitting radio frequencies at ω_p and $2\omega_p$ will be explained in more detail in Chapter 2. Figure 1.7 shows type III radio bursts below 400 MHz observed by Zucca et al. (2012). A

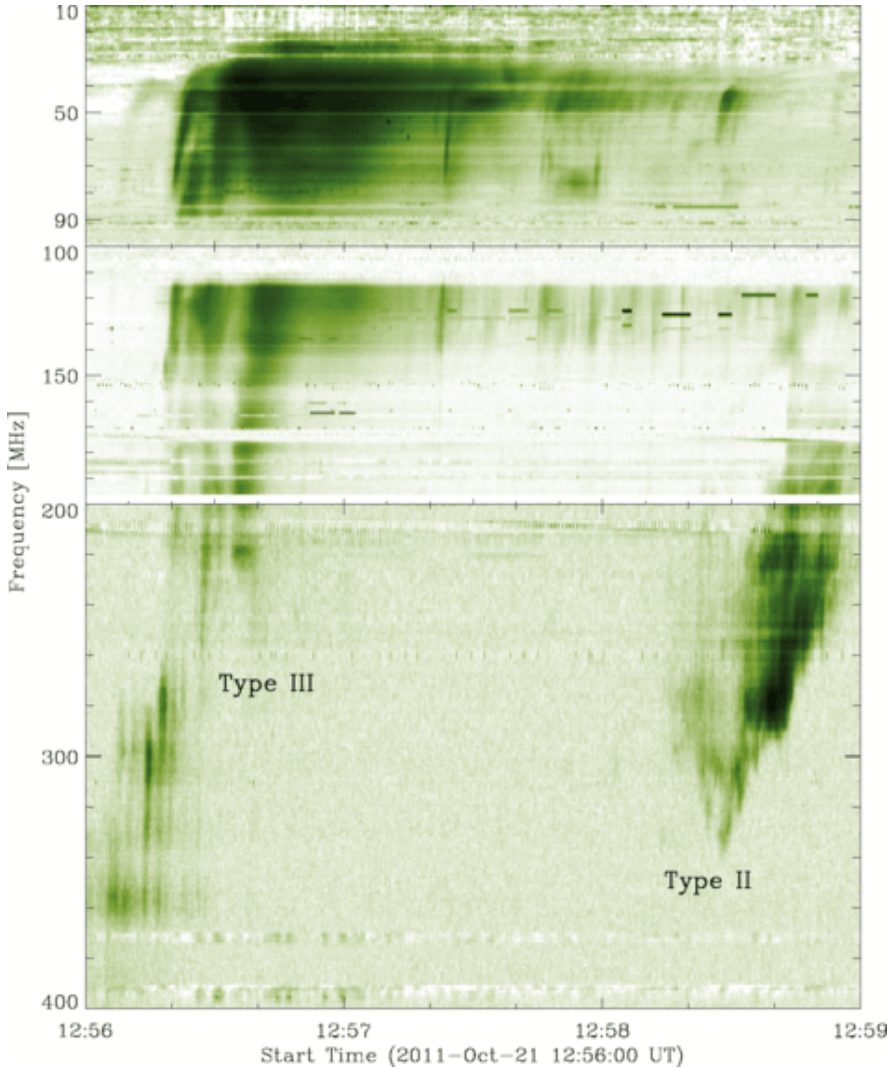

Figure 1.7: A number of type III bursts observed by Zucca et al. (2012) on 21 October 2011. The x axis gives the time on 21 October 2011 while the y axis shows the frequency in MHz. A number of type III bursts extend to frequencies below 200 MHz. A type II burst can be seen between 140 and 330 MHz later in the day.

type II burst was also observed between 140 and 330 MHz and exhibits a much slower frequency drift than the type III bursts. A type III storm can be seen below 200 MHz. This is when type III emission is continuous over the span of large time scales and can last days. Type III bursts come in a number of subcategories described below.

Reverse and bi-directional bursts. A typical type III burst is produced when an electron beam travels along a magnetic field line away from the Sun to areas of lower density. If, instead, electrons travel towards the Sun to areas of higher density a reversed frequency drift is observed. Bursts where both the regular and reverse drifts can be seen simultaneously are bi-directional bursts (Reid & Ratcliffe, 2014).

Type IIIb bursts. Fine frequency structures are sometimes seen in type III bursts. Type IIIb radio bursts are defined as a number of narrow, nearly horizontal, frequency bands called striae, or striations, in the envelope of a type III. The frequency width of an individual striae is typically 0.05 MHz (McLean & Labrum, 1985) and they have a frequency drift rate of $\lesssim 150$ kHz s^{-1}, which implies a speed of 0.6 Mm s^{-1} Sharykin et al. (2018). Figure 1.8 shows a dynamic spectrum of a type IIIb burst from Kontar et al. (2017). Individual striae can be clearly seen in panel b of Figure 1.8. The theory describing the origin of this fine frequency structure has recently been revisited by Reid & Kontar (2021) who found that the striations are due to turbulence in the corona and their drift a result of moving Langmuir waves.

Type U and J bursts. In the case where electrons are travelling along a closed magnetic field line, a turning point in the frequency drift of a type III burst can be observed. For electrons that generate radio emission down to the footpoint of the magnetic field line, a U burst is observed. A U burst can be identified as an inverted U on a dynamic spectrum. More often, electrons stop generating radio emission as they travel back down the magnetic field line so only the turning point in frequency drift is visible in dynamic spectra. These are known as J type bursts. U and J bursts are far less common than type III bursts, despite the similar number of open and closed

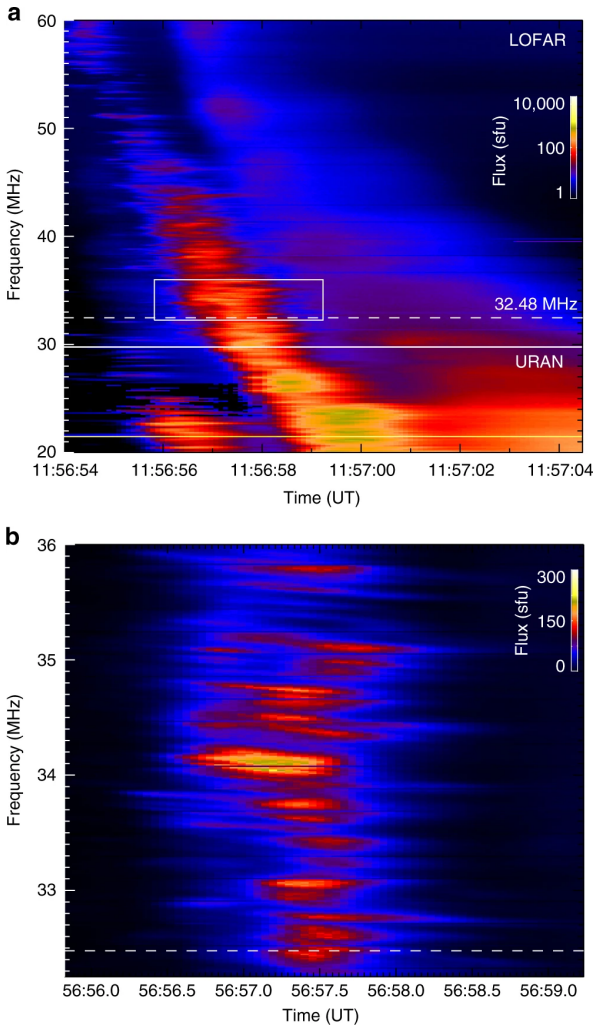

Figure 1.8: A type IIIb radio burst on 16 April 2015 analysed by Kontar et al. (2017). Here the x axes show the time and the y axes show frequency in MHz. The colourbars denote the flux of the radio burst measured in solar flux units (1 sfu = 10^4 Jy). Panel a shows the full duration of the type IIIb. Panel b is a zoom in of the 3 second wide box in panel a.

magnetic field lines along which electron beams can propagate. The reason for this proposed by Reid & Kontar (2017) is that the length of these closed loops is not long enough for the electron beam to become unstable to Langmuir waves.

The study of type III bursts offers an insight into the process of Langmuir wave generation in the solar corona and as such are an important tool in understanding the physics of coronal plasma (Reid & Ratcliffe, 2014). However, the effects of radio wave propagation from the source to the observer through the corona must but understood before inferences can be drawn from observations.

1.4.2 Low Frequency Radio Wave Scattering

Spectral analysis of short temporal radio bursts with small bandwidths at ~ 30 MHz suggests that source sizes in the corona are of the order $\lesssim 1$ arcmin (McConnell, 1980; Kontar et al., 2017). Radio images of the Sun at metric and decametric wavelengths have yet to reveal this level of spatial structure. This was mostly due to the limitations of angular resolution of radio telescopes at the time. Observations with modern interferometers at these frequencies however, still have not observed spatial structure at these scales. The suggestion that there is a fundamental limit imposed upon the level of resolution obtainable by scattering of radio waves in a turbulent corona (Bastian, 1994) has re-emerged in recent years (Thejappa et al., 2007; Thejappa & MacDowall, 2008; Kontar et al., 2017, 2019).

The development of scattering theory stems from Chandrasekhar (1952) description of light scattered by a thin screen and will be outlined further in Chapter 2. The implementation of this theory into computational modelling has also seen considerable development since the first ray tracing experiments by Fokker (1965). Steinberg et al. (1971) built upon this by including the effect of spherical refraction through the corona and were able to obtain the time response of a scattered pulse source.

Both Fokker (1965) and Steinberg et al. (1971) followed from Chandrasekhar (1952) and assumed density inhomogeneities in the corona had a Gaussian power spectrum.

However, it is now known that this assumption is incorrect. Bastian (1994) provides a review of the work by Coles & Harmon (1989) and others to determine the shape of density inhomogeneity power spectrum. At large scales, greater than a few hundred kilometres, the spectrum is well described with a power law index of -5/3, which agrees with the Kolmogorov description of turbulence (Kolmogorov, 1941) of density fluctuations with respect to size scale. For scales smaller than these but greater than a few kilometres, the spectrum becomes shallower and is better described with a power law index of ~ 3. Finally, on the smallest scales less than a few kilometres the spectrum steepens again. This steepening has been interpreted as the scale at which energy is dissipated by turbulence. Coles & Harmon (1989) also found that this inner scale increases with heliocentric distance. Bastian (1994) expanded on this description of the density inhomogeneity power spectrum and investigated the angular broadening of radio waves sources at centimetre wavelengths.

The latest development in the modelling of radio wave scattering is by Kontar et al. (2019). Rather than using the small scattering angle approximation of previous work, Kontar et al. (2019) build on the work of Arzner & Magun (1999) and Bian et al. (2019). In this approach, the effect of anisotropic density inhomogeneities is treated as photon diffusion in momentum space and the Hamiltonian equations for photon position and momentum can be solved iteratively to trace a photon's path. This allows for a continuous transition from weak to strong scattering, whereas previous work is limited to regime of small angle scattering.

Understanding radio wave propagation effects, in particular scattering, is important because they affect all observations made at radio wavelengths. Radio wave scattering has been shown to depend on the relative level of density fluctuations in the corona and as such, offers a chance to learn about its turbulent nature. By classifying the power spectral density of these fluctuations it may be possible to gain an understanding of the turbulent processes that transport energy to the microscopic scales and result in the heating of the corona.

1.5 Thesis Outline

The high spatial, temporal and spectral resolution of modern radio interferometers such as LOFAR and the launch of new space missions including Parker Solar Probe (PSP; Fox et al., 2016) and Solar Orbiter (Müller et al., 2020) has ushered in a new age of solar radio observations. By developing a computational backend and using a unique method for fitting interferometric visibilities, this thesis has furthered the capability of an international LOFAR station and extracted value from existing interferometric observations. This thesis outlines how such developments have improved our knowledge of radio wave propagation in the solar corona using observations at some of the highest spatial, spectral and temporal resolutions available. In Chapter 2 I outline the relevant background theory for the work presented in this thesis. Chapter 3 will describe the instrumentation used throughout this thesis, namely LOFAR, and the mathematical background for interferometric imagining.

The REALtime Transient Acquistion backend (REALTA), is a seven node computer cluster designed to record and analyse the raw beamformed data from international LOFAR stations in real-time. The development of REALTA for solar and a myriad of other observations formed a key part of this work. Chapter 4 describes the hardware and software of REALTA and showcases some first light observations.

The study of radio wave scattering in the solar corona has undergone a renaissance in recent years both in terms of computational modelling and observations. Chapter 5 will describe how, for the first time, LOFAR visibilities were fitted directly to determine the size and position of a type IIIb burst. This lead to a more subtle understanding of the root mean squared fluctuations of electron density in the solar corona, the key parameter necessary to quantify the effect of scattering.

In order to accurately compare between models of the solar corona, in Chapter 6 I present 29 type III radio bursts and determine their size and position using the visibility fitting technique with a Markov Chain Monte Carlo optimization. The results of this show that type III bursts exhibit an intrinsic source size greater than the size of a point

source that has been scattered and highlights discrepancies between observations and computational modelling.

Chapter 7 includes a discussion on the future work that can be carried out from the foundations of this thesis. It outlines the necessary further studies needed to further our knowledge of radio wave scattering and how to utilise even higher temporal resolution observations of the radio sun. Chapter 7 will also contain a summary and conclusion of the work presented in this thesis.

2

Theoretical Background

The following chapter describes the main theoretical concepts relevant to this thesis. In order to understand the corona, one must understand the plasma it is made of. Thus, I start in section 2.1 with some fundamental concepts of plasma physics and introduce the kinetic theory of plasmas by considering the distribution of many particles in a six dimensional phase space. This lays the groundwork for a fluid description of plasmas, magnetohydrodynamics (MHD), arguably the most useful description of a plasma in the context of the solar corona which is discussed in section 2.2. The MHD equations are investigated further to determine how longitudinal and transverse waves propagate in a plasma which is relevant for the subsequent discussion of Langmuir wave generation and the plasma emission mechanism of type III radio bursts in section 2.3. Section 2.4 gives an overview of the theory of radio wave scattering in the corona and concludes this chapter.

2.1 Introductory Concepts in Plasma Physics

Plasma was the name given by Langmuir to the new, exotic type of matter he was studying in the 1920s. It is essentially an ionized gas that exhibits quasi-neutrality on a macroscopic scale. The solar corona is a shell of hot plasma surrounding the Sun and as such, the study of emission from the corona is a study of the plasma itself. A plasma's tendency to remain in quasi-neutrality means that any change to the charge separation between electrons and ions generates an electric field which acts as a restoring force and thus oscillations are induced in the plasma. To determine the frequency of these oscillations imagine the following, a plasma with equal number density of electrons and ions $N_e = N_i = N_0$ is perturbed so that a group of electrons are moved by some distance x a restoring force $\mathbf{E} = q_e E_x$ acts to bring the electrons back to their initial position. Due to their mass, the electrons overshoot their initial position and the process begins again in the opposite direction. Here we have made the

safe assumption that, due to electrons being much lighter, the ions remain stationary. For electrons with mass m_e, Newton's second law gives us,

$$m_e \frac{d^2x}{dt^2} = q_e E_x. \tag{2.1}$$

Gauss' law for some closed, rectangular box surface, S, inside our perturbed plasma gives,

$$\oint_S \mathbf{E} \cdot d\mathbf{s} = \frac{Q}{\epsilon_0}$$

where Q is the total charge contained within the closed surface S. Given the equilibrium density of electrons, N_e, the total charge must be $Q = AxN_eq_e$ where A is the cross-sectional area of S. For $A = a\Delta z$, we can solve for E_x to find,

$$\oint_S \mathbf{E} \cdot d\mathbf{s} = -a\Delta z E_x = \frac{Q}{\epsilon_0} = \frac{ax\Delta z N_e q_e}{\epsilon_0} \rightarrow E_x = -\frac{xN_eq_e}{\epsilon_0}.$$

Using this with Equation 2.1 we obtain the ordinary differential equation,

$$m_e \frac{d^2x}{dt^2} + \frac{N_e q_e^2}{\epsilon_0} x = 0 \rightarrow \frac{d^2x}{dt^2} + \omega_p^2 x = 0. \tag{2.2}$$

The solution to this equation is the well known harmonic oscillator with an angular frequency ω_p which we call the electron plasma frequency or simply, the plasma frequency

$$\omega_p = \sqrt{\frac{N_e q_e^2}{\epsilon_0 m_e}}. \tag{2.3}$$

The plasma frequency leads us to an important criterion that a partially ionised gas must have to be considered a plasma. That is, plasma oscillations can only develop if the mean free time between collisions of electrons and ions with neutrals, τ_n, is longer than the oscillation period $\tau_p = 1/\omega_p$, or $\omega_p \tau_n > 1$.

Another implication of the quasi-neutrality of plasmas can be seen when one considers immersing a test particle of charge Q_+ inside an initially uniform plasma at time $t = 0$ such that, again, $N_i = N_e = N_0$. The electric potential in the plasma is that due

to the single test charge,

$$\Phi(\mathbf{r}) = \frac{1}{4\pi\epsilon_0}\frac{Q}{r},$$

assuming the test charge is at the origin of our spherical coordinate system. Once again we assume that because the ions are much more massive compared to the electrons in the plasma that their motion can be neglected. The electrons in the plasma are attracted to the test charge causing the electron density near the test charge to increase. The new potential distribution $\Phi(\mathbf{r})$ must be re-evaluated using Poisson's equation:

$$\nabla^2\Phi(\mathbf{r}) = -\frac{\rho}{\epsilon_0} = -\frac{q_e(N_e - N_i)}{\epsilon_0}, \tag{2.4}$$

where the excess free charge density near the test charge is $\rho = q_e(N_e - N_i)$. In spherical coordinates this leads to an electron density distribution of,

$$N_e(r) = N_0 e^{-q_e\Phi(r)/k_b T_e} \tag{2.5}$$

where k_B is Boltzman's constant and T_e is the electron temperature. Subbing into the spherical coordinate version of Equation 2.4 gives,

$$\frac{1}{r^2}\frac{d}{dr}\left(r^2\frac{d\Phi}{dr}\right) = -\frac{q_e N_0}{\epsilon_0}\left[\exp\left(\frac{-q_e\Phi(r)}{k_B T}\right) - 1\right], \; r > 0. \tag{2.6}$$

Assuming $|q_e\Phi| \ll k_b T$, Equation 2.6 can be expanded as a power series to give,

$$\frac{1}{r^2}\frac{d}{dr}\left(r^2\frac{d\Phi}{dr}\right) \simeq \left[\frac{N_0 q_e^2}{\epsilon_0 k_B T_e}\right]\Phi(r) = \frac{1}{\lambda_D^2}\Phi(r)$$

where λ_D, known as the Debye length, is defined to be

$$\lambda_D = \sqrt{\frac{\epsilon_0 k_B T_e}{N_0 q_e^2}}. \tag{2.7}$$

The solution to the above can be found to be

$$\Phi(r) = \left[\frac{1}{4\pi\epsilon_0}\frac{Q}{r}\right] e^{-r/\lambda_D}, \tag{2.8}$$

which shows that for $r \gg \lambda_D$, the potential of the test charge disappears. Thus the Debye length of a plasma can be used to define a second plasma criterion: an ionised gas can only be considered a plasma if the length scale of the system, L, is much greater than the Debye length.

2.1.1 Kinetic Theory

Armed with some knowledge of fundamental plasma behaviour, we jump forward through plasma theory to determine the collective properties of plasmas using averages over large numbers of particles. In order to do so, the positions and velocities of plasma particles are described using a distribution function in an approach called plasma kinetic theory. For now the exact form of this distribution function does not matter. We start by assuming that the position of each particle in our plasma is given by a vector $\mathbf{r}$ from the origin where,

$$\mathbf{r} = \hat{\mathbf{x}}x + \hat{\mathbf{y}}y + \hat{\mathbf{z}}z \tag{2.9}$$

and that each particle has a linear velocity,

$$\mathbf{v} = \hat{\mathbf{x}}v_x + \hat{\mathbf{y}}v_y + \hat{\mathbf{z}}v_z \tag{2.10}$$

so that the particle speed is $|\mathbf{v}| = v = \sqrt{v_x^2 + v_y^2 + v_z^2}$. Thus, at any given time, the position and velocity of a particle can be represented as a point in a six dimensional phase space determined by the coordinates x, y, z, v_x, v_y and v_z. Now consider a volume element $d\mathbf{r} = d^3r = dxdydz$ such that it is large enough to contain a great number of particles but small enough so that macroscopic quantities vary only slightly inside it. Also consider a time interval dt centred around time t, where dt is long compared to

the mean time for a particle to traverse $d\mathbf{r}$ but similarly short enough compared to the time scales of the macroscopic parameters of the plasma. The number of particles in $d\mathbf{r}$ averaged over dt is simply $N(\mathbf{r},t)d\mathbf{r}$ where $N(\mathbf{r},t)$ is the number density of particles. In the same manner, one can define a density of the number of particles in velocity space which we denote as $f(\mathbf{r},\mathbf{v},t)d\mathbf{r}$. From this, we can determine the number of particles at time t in the element $d\mathbf{r}$ and with velocities between $\mathbf{v}$ and $\mathbf{v}+d\mathbf{v}$ is $f(\mathbf{r},\mathbf{v},t)d\mathbf{r}d\mathbf{v}$ The function $f(\mathbf{r},\mathbf{v},t)$ is called the velocity distribution function and is the density of representative points in phase space. The total number of velocity points in all of velocity space can be found by summing the number of velocity points $f(\mathbf{r},\mathbf{v},t)d\mathbf{r}d\mathbf{v}$ in $d\mathbf{v}$ over all possible velocities. Following from this, we can obtain the number density of particles:

$$N(\mathbf{r},t)=\int_{-\infty}^{\infty} f(\mathbf{r},\mathbf{v},t)d\mathbf{v}. \tag{2.11}$$

Other macroscopic plasma parameters (e.g. mass density, flux, current) can be obtained using the velocity distribution function. Consider any property $g(\mathbf{r},\mathbf{v},t)$ of a particle. The average value of this quantity is given by

$$g_{\mathrm{av}}(\mathbf{r},t)=\langle g(\mathbf{r},\mathbf{v},t)\rangle=\frac{1}{N(\mathbf{r},t)}\int g(\mathbf{r},\mathbf{v},t)f(\mathbf{r},\mathbf{v},t)d\mathbf{v}. \tag{2.12}$$

The evolution of the velocity distribution function, which we henceforth refer to as the distribution function, or f, in time is determined by the Boltzmann Equation:

$$\frac{\partial f}{\partial t}+(\mathbf{v}\cdot\nabla_{\mathbf{r}})f+\left[\left(\frac{\mathbf{F}}{m}\right)\cdot\nabla_{\mathbf{v}}\right]f=\left(\frac{\partial f}{\partial t}\right)_{\mathrm{coll}} \tag{2.13}$$

where $\mathbf{F}=m\mathbf{a}$ is a force acting on the particles. The Boltzmann equation is essentially a statement on the conservation of points in phase space. The left hand side describes particle flow through the volume element $d\mathbf{r}d\mathbf{v}$ and it is balanced by the collisional term on the right hand side. By considering a homogeneous plasma in a steady-state (i.e. in thermal equilibrium) with no external forces, the terms on the left hand side of

the Boltzmann equation all become 0 and thus

$$\left(\frac{\partial f}{\partial t}\right)_{\text{coll}} = 0.$$

By considering the particle collisions in which energy must be conserved under the above assumptions it can be shown that the distribution function takes the form of the Maxwell-Boltzmann distribution:

$$f(\mathbf{r}, \mathbf{v}, t) = f(v) = N_0 \left(\frac{m}{2\pi k_B T}\right)^{\frac{3}{2}} e^{-mv^2/(2K_B T)}. \tag{2.14}$$

By substituting the Lorentz force into 2.13, assuming no collisions, gives the Vlasov equation:

$$\frac{\partial f}{\partial t} + (\mathbf{v} \cdot \nabla_{\mathbf{r}}) f + \frac{q}{m} \left[(\mathbf{E} + \mathbf{v} \times \mathbf{B}) \cdot \nabla_{\mathbf{v}}\right] f = 0. \tag{2.15}$$

The Vlasov equation, together with Maxwell's equations for $\mathbf{E}$ and $\mathbf{B}$ represent a complete set of self-consistent equations to describe a plasma interacting with an electromagnetical field. So far we have considered the derivatives of f with respect to a stationary reference frame. It is more convenient to consider a reference frame that moves with the fluid elements of a plasma. A derivative in this sense is known as a convective derivative or total time derivative and can be expressed for the distribution function as

$$\frac{df}{dt} = \frac{\partial f}{\partial t} + (\mathbf{v} \cdot \nabla_{\mathbf{r}}) f + \left(\frac{d\mathbf{v}}{dt} \cdot \nabla_{\mathbf{v}}\right) f. \tag{2.16}$$

Thich has the interesting result that the collisionless Boltzmann equation can be written as

$$\frac{df}{dt} = 0, \tag{2.17}$$

meaning that a particle moving through phase space will see a constant f in its local frame. This is known as Liouville's theorem. The Boltzmann equation allows us to determine the macroscopic transport equations of a plasma, which will form the foundations of the theory in the section to come. This is done not by solving the Boltzmann

equation itself but rather, multiplying it by various powers of $\mathbf{v}$ and integrating over velocity, i.e. "taking the moments of the Boltzmann equation"

$$\mu_n = \int \mathbf{v}^n \, [\text{Boltzmann Eq.}] \, dv,$$

where μ_n is the nth order moment. This procedure gives up our knowledge on the velocity distribution of particles in order to instead obtain single-value macroscopic particles of a plasma fluid. The main results for the first 3 moments are shown here [1]:

$\mu_0 \rightarrow$ continuity equation or conservation of mass

$\mu_1 \rightarrow$ momentum transport equation or conservation of momentum

$\mu_2 \rightarrow$ energy transport equation or conservation of energy

The moments of the Boltzmann equation allow us to develop the theory of plasmas as being made up of multiple fluids each of their different particle species, e.g. electrons and ions. Under certain conditions it is possible to consider the entire plasma as a single fluid and it is this approach, called magnetohydrodynamics, that I discuss next[2].

2.2 Magnetohydrodynamics

Magnetohydrodynamics (MHD) is a framework to describe the dynamics of an electrically conducting fluid in the presence of a magnetic field. It is a useful method that can be used to model large-scale, slowly varying plasma phenomena in a highly ionised plasma. For plasmas that are either collision-dominated or contain a strong external magnetic field the MHD description of a plasma is particularly appropriate. Given that these conditions are met in the solar corona, it is worth expanding upon some key ideas of MHD theory. For now we assume a collision-dominated plasma but the same

[1] The interested reader is referred to e.g. Inan & Golkowski (2010) for a full derivation of these equations.

[2] The derivations of the equations of motion for a two-fluid plasma and their subsequent combination to a single fluid are complex and tedious. I therefore once again refer an interested reader to e.g. Inan & Golkowski (2010)

ideas can be applied to collisionless plasmas with strong magnetic fields.

The single fluid equations, derived from the moments of the Boltzmann equation, and the generalised Ohm's law can be simplified using several approximations to form what are known as the simplified MHD equations.

$$\mathbf{J} = \sigma(\mathbf{E} + \mathbf{u}_m \times \mathbf{B}) \tag{2.18a}$$

$$\frac{\partial \rho_m}{\partial t} + \rho_{m0} \nabla \cdot \mathbf{u}_m = 0 \tag{2.18b}$$

$$\rho_m \frac{\partial \mathbf{u}_m}{\partial t} = -\nabla p + \mathbf{J} \times \mathbf{B} \tag{2.18c}$$

where $\mathbf{J}$ is the current density, σ is the electrical conductivity, ρ_m is the (variable) mass density, ρ_{m0} is the (relatively constant) mass density, $\mathbf{u}_m$ is the mass velocity and p is the pressure. The electromagnetic fields inside a plasma are governed by Maxwell's equations,

$$\nabla \cdot \mathbf{E} = \frac{\rho}{\epsilon_0} = 0 \tag{2.19a}$$

$$\nabla \cdot \mathbf{B} = 0 \tag{2.19b}$$

$$\nabla \times \mathbf{E} = -\frac{\partial \mathbf{B}}{\partial t} \tag{2.19c}$$

$$\nabla \times \mathbf{B} = \mu_0 \mathbf{J} \tag{2.19d}$$

where the assumption of no accumulation of charge inside the fluid gives rise to the charge density $\rho = 0$. Finally, by assuming an adiabatic equation of state,

$$\frac{d}{dt}\left(p \rho_m^{-\gamma}\right) = 0 \tag{2.20}$$

where γ is the adiabatic index. Equations 2.18, 2.19 and 2.20 form a closed system which can be solved for any of the fluid or electromagnetic variables. These equations can be used to describe some simple wave phenomena that MHD plasmas exhibit which are relevant to the later discussion of the plasma emission mechanism.

2.2.1 Waves in Plasmas

As we shall see shortly, the generation and propagation of waves in plasmas can result in the emission of electromagnetic radiation which, in turn, must travel through the plasma. Consequently, it is important to outline the basics of waves in plasmas. In the following we only consider waves of small amplitude superimposed on a background of a uniform, unmagnetised plasma. Background quantities will be denoted by a subsrcipt of '0', while the perturbed quantities will be given a subscript '1'. We also only consider the case where there is no steady fluid motion and no external electric field. Thus we can write the simplified MHD equations (assuming no collisions and an adiabatic equation of state) as

$$\frac{\partial N_1}{\partial t} + N_0 \nabla \cdot \mathbf{u} = 0 \tag{2.21a}$$

$$N_0 m \frac{\partial \mathbf{u}}{\partial t} = q N_0 (\mathbf{E} + \mathbf{u} \times \mathbf{B}_0) - \nabla p_1 \tag{2.21b}$$

$$\frac{p_1}{p_0} = \gamma \frac{N_1}{N_0} \rightarrow p_1 = \gamma k_B T N_1. \tag{2.21c}$$

Here N is the electron density, $\mathbf{u}$ is the fluid velocity, m is the particle mass, $\mathbf{B}$ is the magnetic field strength, p is the pressure, γ is the adiabatic index and T is the temperature. The assumption that each particle species is an isothermal gas with temperature T gives $p_0 = N_0 k_b T$. Maxwell's equations then become

$$\nabla \cdot \mathbf{E} = \frac{\rho_1}{\epsilon_0} \tag{2.22a}$$

$$\nabla \cdot \mathbf{B}_1 = 0 \tag{2.22b}$$

$$\nabla \times \mathbf{E} = -\frac{\partial \mathbf{B}_1}{\partial t} \tag{2.22c}$$

$$\nabla \times \mathbf{B}_1 = \mu_0 \mathbf{J} + \epsilon_0 \frac{\partial \mathbf{E}}{\partial t} \tag{2.22d}$$

In order to study plane waves, solutions of the above where all perturbation quantities vary proportionally to $e^{i(\omega t - \mathbf{k}\cdot\mathbf{r})}$ are sought. In the following we use the fact that for solutions of this form $\partial/\partial t \rightarrow i\omega$ and $\nabla \rightarrow -i\mathbf{k}$. For a cold plasma with $T = 0$ the

equation of motion of the electrons is reduced to

$$m_e i\omega \mathbf{u}_e = q_e \mathbf{E} \tag{2.23}$$

Taking the divergence of 2.23 and using 2.21a gives

$$N_1 = \frac{N_0 q_e}{m_e \omega^2} \nabla \cdot \mathbf{E} \rightarrow \rho_1 = N_1 q_e - \frac{N_0 q_e^2}{m_e \omega^2} \nabla \cdot \mathbf{E}. \tag{2.24}$$

For a longitudinal wave $\nabla \cdot \mathbf{E} \neq 0$ and thus, using 2.22a, we must have

$$\omega^2 = \frac{N_0 q_e^2}{m_e \epsilon_0} \equiv \omega_p^2 \tag{2.25}$$

which is the plasma frequency we found earlier from our discussion at the beginning of Section2.1! Note also that, because ω does not depend on $\mathbf{k}$, the group velocity $v_g = d\omega/dk$ of this wave is 0. This means that the plasma oscillation does not propagate from the location where they are generated. For a magnetised plasma with finite temperature the dispersion relation of Langmuir waves becomes

$$\omega^2 = \omega_p^2 (1 + \gamma \lambda_D^2 k^2), \tag{2.26}$$

where γ is the adiabatic index. This propagating plasma oscillation is known as a Langmuir wave and will be instrumental in describing the process of plasma emission in a type III radio burst.

Electromagnetic waves travelling through a plasma have their own dispersion relation which can be found from the refractive index

$$\mu \equiv \frac{kc}{\omega} = \left(1 - \frac{\omega_p^2}{\omega^2}\right)^{\frac{1}{2}} \tag{2.27}$$

to be

$$\omega = (\omega_p + k^2 c^2)^{\frac{1}{2}}. \tag{2.28}$$

Here it is obvious that ω_p acts as a cutoff frequency, below which electromagnetic waves become evanescent and are rapidly attenuated. To further demonstrate this effect, consider the group velocity of radio waves travelling through a plasma

$$\begin{aligned} v_g &= \frac{\partial \omega}{\partial k} = \frac{\partial}{\partial k}(\omega_p + k^2c^2)^{\frac{1}{2}} \\ &= \frac{1}{2}(\omega_p + k^2c^2)^{-\frac{1}{2}}(2kc^2) \\ &= \frac{kc^2}{\omega} = c\mu. \end{aligned} \tag{2.29}$$

For a radio wave at the plasma frequency ω_p, $\mu = 0$ and thus the group velocity is 0. Therefore radio waves at the plasma frequency cannot travel through the corona, this explains why the ratio for fundamental to harmonic emission mentioned in section 1.4.1 is less than 2:1.

2.3 The Plasma Emission Mechanism

The plasma emission mechanism occurs over a number of stages. First, an instability must be generated in the velocity distribution function. This leads to the growth of Langmuir waves before finally these Langmuir waves are converted to transverse electromagnetic waves. In a type III radio burst a high velocity, low density, electron beam passes through the background plasma to form a "bump on tail" distribution. This distribution is unstable and leads to the growth of Langmuir waves. These Langmuir waves in turn generate electromagnetic waves by coalescing with other Langmuir waves or by decaying. The electromagnetic waves are the radio bursts that are observed. In this section the generation of Langmuir waves in 1D and the process of plasma emission are discussed under the framework of quasi-linear theory.

2.3.1 Generation of Langmuir Waves

During magnetic reconnection electrons can be accelerated along magnetic field lines. As these beams of electrons propagate, faster electrons begin to outpace slower elec-

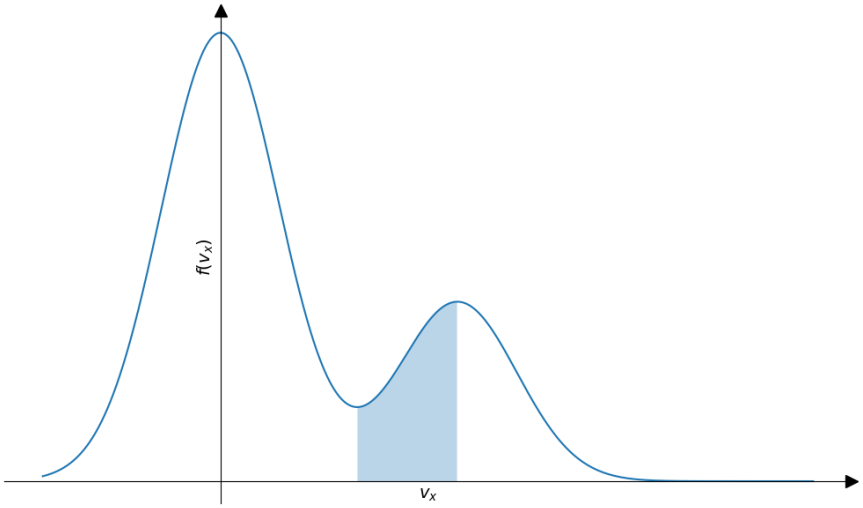

Figure 2.1: The 1D electron velocity distribution function of a background plasma and a low density, high velocity electron beam. The x axis is velocity while the y axis is the electron distribution function. This plot shows what is known as the "bump on tail" distribution. The shaded region indicates where the gradient of the distribution function is positive and can excite Langmuir waves in the background plasma.

trons and stationary ions in the background plasma. This leads to a second peak on the Maxwell-Boltzmann distribution of velocities as seen in Figure 2.1. Energy is transferred from electrons travelling at the phase velocity, v_ϕ , to Langmuir waves creating a resonance. The positive velocity gradient of this resonance means that there are more electrons with velocity greater than v_ϕ than there are electrons with velocities less than v_ϕ (where energy is transferred from the wave to the particles), this causes Langmuir waves to become unstable and their magnitudes to grow exponentially. Particles with velocities near v_ϕ are in resonance with the Langmuir waves and drive this instability.

In the following, the electron velocity distribution function is described as the sum of a slowly varying part f_0 and a rapidly oscillating part f_1, where $|f_1| \ll f_0$

$$f(\mathbf{r}, \mathbf{v}, t) = f_0(\mathbf{v}) + f_1(\mathbf{r}, \mathbf{v}, t). \tag{2.30}$$

Equation 2.30 can now be substituted into the Vlasov Equation (Equation 2.15), where we note that $\mathbf{E}$ and f_1 are perturbation quantities. By neglecting second order terms and assuming an unmagnetised plasma, i.e. $\mathbf{B} = 0$, we obtain the linearalised Vlasov

Equation

$$\frac{\partial f_1}{\partial t} + (\mathbf{v} \cdot \nabla) f_1 + \frac{q_e}{m_e} \mathbf{E} \cdot \nabla_{\mathbf{v}} f_0 = 0. \tag{2.31}$$

It can be shown that in 1D the electron distribution function, $f(v,t)$ where $\int f(v,t)dv = n_e$, and the spectral energy density of Langmuir waves, $W(v,t)$ such that $\int W(v,t)dv = E_L$ the total energy density, can be expressed as follows (Vedenov, 1963; Reid & Ratcliffe, 2014),

$$\frac{\partial f(v,t)}{\partial t} = \frac{4\pi^2 e^2}{m_e^2} \frac{\partial}{\partial v} \left(\frac{W}{v} \right) \frac{\partial f(v,t)}{\partial v} \tag{2.32}$$

$$\frac{\partial W(v,t)}{\partial t} = \frac{\pi \omega_p}{n_e} v^2 W \frac{\partial f(v,t)}{\partial v} \tag{2.33}$$

Equation 2.33 shows that the growth rate of Langmuir waves is proportional to $\frac{\partial f(v,t)}{\partial v}$, hence a positive gradient in the Maxwell Boltzmann distribution leads to a growth in Langmuir waves. The right hand side of Eq. 2.32 has a diffusion operator $D = \frac{W}{v}$. This states that the transfer of energy from particles to waves and back leads to the distribution function being smoothed out and eventually becoming a plateau. The evolution of $f(v,t)$ and $W(v,t)$ with time is shown in Figure 2.2. As time progresses, a plateau is formed in the distribution function and a broadening of the spectral energy density develops. This process is known as quasi-linear relaxation (Melrose, 1987).

2.3.2 Wave-Wave Interaction

Now that we know how Langmuir waves are generated by an unstable distribution, we must discuss how these Langmuir waves are converted to electromagnetic waves via wave-wave interactions. Wave-wave interaction concerns the processes by which three types of waves interact. These are: transverse (T) waves, Langmuir (L) waves and ion sound (S) waves, and have the following, respective, dispersion relations:

$$\omega_T = (\omega_p^2 + k^2 c^2)^{\frac{1}{2}}$$

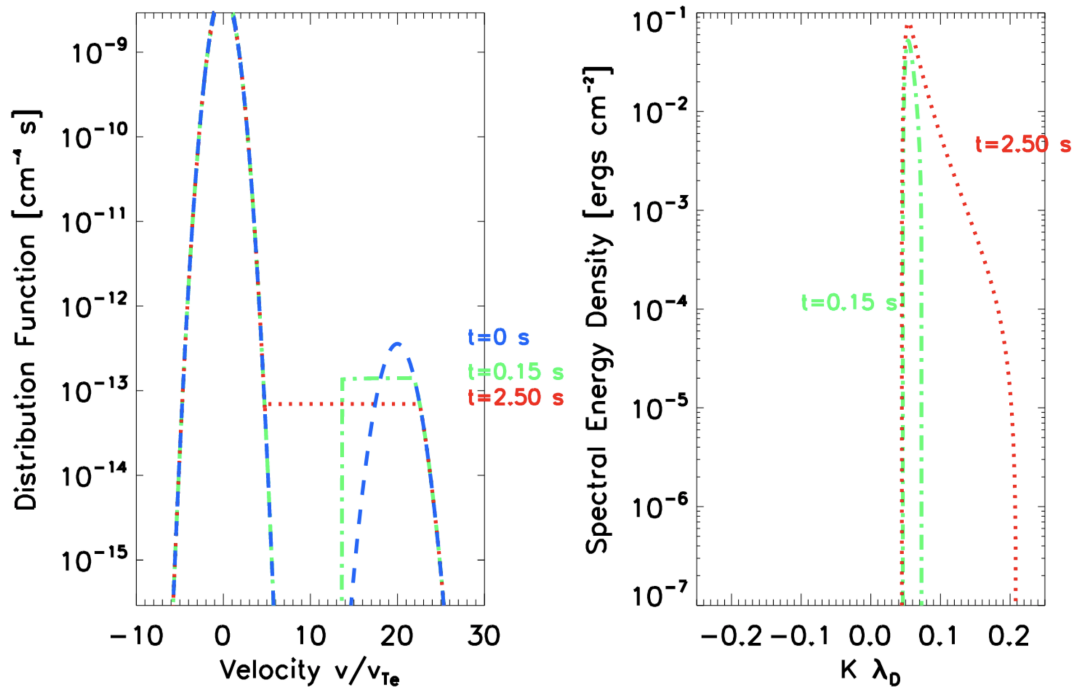

Figure 2.2: Modelled evolution of the electron distribution function (cm^{-4} s) and spectral energy density (erg cm^{-2}) with time. Left: Evolution of distribution function in time where the x axis is velocity normalised by the electron thermal velocity $v_{Te} = V_e$. The diffusive term in Equation 2.32 causes the bump-on-tail Gaussian to turn into a plateau, thereby eliminating the instability caused by the positive velocity gradient. Right: The spectral energy density of generated Langmuir waves, x axis is wave number normalised to the Debye length $\lambda_D = \sqrt{\frac{\epsilon_0 k_B T_e}{e^2 n_e}}$. Each panel shows successive times of t=0.15s (green, dot-dashed line) and t=2.50s (red, dotted line). Figure taken from Reid & Ratcliffe (2014).

$$\omega_L \cong \omega_p + \frac{3k^2V_e^2}{2\omega_p}$$

$$\omega_S = kv_s$$

where V_e is the thermal velocity of electrons in the plasma, v_s is the ion sound speed and k is the wave vector. Only transverse waves with $\omega > \omega_p$ can escape and thus a plasma emission mechanism is a process that generates these transverse waves.

As mentioned in Section 1.4.1, type III bursts have a harmonic structure associated with plasma emission at the plasma frequency and the second harmonic. Both of these transverse waves are formed in different three-wave processes that will now be discussed. In a plasma, due to scattering from other wave modes and ions in the plasma, a wave mode can be changed from one to the other (McLean & Labrum, 1985;

Melrose, 1987). This is expressed in the equation

$$\sigma \rightleftarrows \sigma' + \sigma''$$

where σ, σ' and σ'' represent different wave modes. Conservation of energy and momentum state (McLean & Labrum, 1985),

$$\omega^{\sigma}(k) = \omega^{\sigma'}(k') + \omega^{\sigma''}(k'')$$

$$k = k' + k''$$

where $\omega^{\sigma}(k)$ is the frequency of a particular wave mode with the wave vector k. For Langmuir (L), ion sound (S) and transverse (T) wave modes the allowed processes are (Melrose, 1987):

$$L + S \rightarrow L'$$

$$L + S \rightarrow T$$

$$L \rightarrow T + S$$

$$L \rightarrow L' + S$$

$$T + S \rightarrow L$$

$$T + S \rightarrow T'$$

$$L + L' \rightarrow T.$$

Of these L+S→T and L→T+S are responsible for fundamental emission while harmonic emission is associated with the three-wave process L+L′ →T (Melrose, 1987).

Originally Ginzburg & Zhelezniakov (1958) considered fundamental emission to be due to Langmuir waves scattering off of thermal ions in the plasma. It is now commonly accepted that the biggest cause of fundamental emission is due to the three-wave processes of a Langmuir wave coalescing with an ion sound wave generated by L→L′+S or when a Langmuir wave decays into an ion sound wave and an electromagnetic trans-

verse wave. The process L→T+S can be visualised as in Figure 2.3. In solar radio physics it is often assumed that $k_L \gg k_T$, knowing this and that the wave vectors must satisfy $\mathbf{k}_L \pm \mathbf{k}_s = \mathbf{k}_T$ (+ for L+S→T , − for L→T+S) implies $\mathbf{k}_s \approx \mp \mathbf{k}_L$.

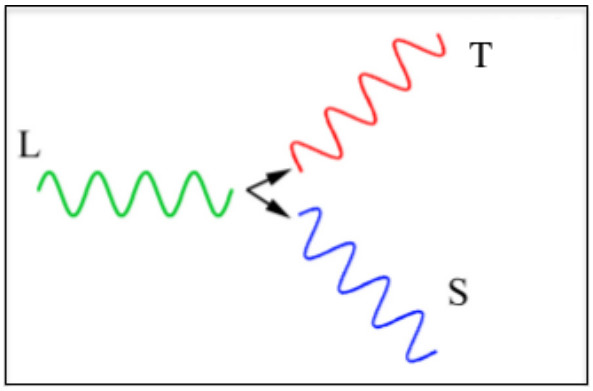

Figure 2.3: A three-wave process of fundamental plasma emission L→T+S. A Langmuir wave decaying into an ion sound wave and an electromagnetic transverse wave at the plasma frequency. (Figure adapted from Solar (interplanetary) Radio Bursts: the Generation of Radio Waves, an oral presentation by David Malaspina at the Jean Louis Steinberg International Workshop on Solar, Heliospheric and Magnetospheric Radioastronomy, November 2017)

Second harmonic emission occurs when two Langmuir waves coalesce in the process L+L′ →T, shown in Figure 2.4. Conservation of momentum requires that $\mathbf{k}_L + \mathbf{k'}_L = \mathbf{k}_T$ and for second harmonic (H) generation, $k_T = k_H \approx \frac{\sqrt{3}\omega_p}{c}$. The phase speed v_ϕ of Langmuir waves is much less than $\frac{c}{\sqrt{3}}$ meaning that $k_L \gg k_T$ which results in $\mathbf{k}_L \approx -\mathbf{k'}_L$. This means that for a transverse wave at the second harmonic to be created, two Langmuir waves must coalesce almost exactly head on. These backward propagating Langmuir waves are generated in the three-wave processes of L+S→L′ and L→L′+S, i.e. scattering off of thermal ions, and by refraction at density inhomogeneities.

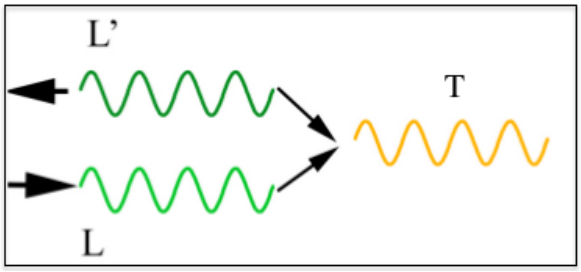

Figure 2.4: Three-wave process of second harmonic plasma emission L+L' → T. A Langmuir wave (L) and a backwards propagating Langmuir wave (L') coalesce to form a transverse wave (T) at $2\omega_p$. (Figure adapted from Solar (interplanetary) Radio Bursts: the Generation of Radio Waves, an oral presentation by David Malaspina at the Jean Louis Steinberg International Workshop on Solar, Heliospheric and Magnetospheric Radioastronomy, November 2017)

2.4 Scattering of radio waves in the solar corona

Chandrasekhar (1952) outlined a statistical description of "stellar scintillation" in order to account for observations with astronomical seeing. The basis of this description is that a plane wave front travels through a turbulent layer whose refractive index, μ, is subject to random fluctuations. The auto correlation function of these fluctuations at two different points $\mathbf{r_1}$ and $\mathbf{r_2}$ is given by

$$\frac{\langle \delta\mu(\mathbf{r_1})\delta\mu(\mathbf{r_2})\rangle}{\langle \delta^2\mu\rangle},$$

and can be defined to be some function $M(r)$ only of the distance between the two points $r = |\mathbf{r_1} - \mathbf{r_2}|$. For the remainder of this section I will describe the Chandrasekhar (1952) treatment of scintillations for a "disturbed layer" in the atmosphere and how this was adopted by Fokker (1965), Steinberg et al. (1971) and Riddle (1974) to explain observed characteristics of radio bursts before finally discussing the modern approach to radio wave scattering.

Under the assumptions of homogeneity and isotropy, the correlation between refractive index fluctuations in the layer will depend only on distance between two points. Thus

$$\langle \delta\mu(\mathbf{r_1})\delta\mu(\mathbf{r_2})\rangle = \langle \delta^2\mu\rangle M(r), \tag{2.34}$$

where $\langle \delta^2\mu\rangle$ is the mean squared fluctuation of refractive index and $M(r)$ is some (even) function of r. Notably, $M(r)$ defines a "micro-scale" r_0 such that $M(r)$ becomes negligible for $r \gg r_0$.

One of the key quantities of interest is the angular deflection of the ray from its linear trajectory. These are denoted as ψ_1 and ψ_2 in the planes containing x_1 and x_2 respectively. Since there is no correlation between deflections in the directions x_1 and x_2 the mean square total deflection can be written as

$$\langle \psi^2(s)\rangle = \langle \psi_1^2(s)\rangle + \langle \psi_2^2(s)\rangle = 2\langle \psi_1^2(s)\rangle \tag{2.35}$$

Following the derivation of Chandrasekhar (1952) it can be shown that

$$\langle \psi^2(s) \rangle = 4\alpha \langle \delta^2 \mu \rangle \left(\frac{s}{r_0} \right), \tag{2.36}$$

where $\alpha = \sqrt{\pi}$ in the case $M(r) = \exp(-r^2/r_0^2)$.

This framework was first used by Fokker (1965) to statistically model rays in a spherically stratified corona, however they did not include the effects of spherical refraction which are relevant when describing radio bursts that are produced near where $\mu = 0$. Hollweg (1967) extended upon the Chandrasekhar (1952) description in particular, for the case $\mu \neq 1$. Using this, Steinberg et al. (1971) consider an unmagnetised, spherical corona with an electron density distribution not dissimilar to Newkirk (1961) and performed a similar ray tracing experiment to Fokker (1965) in order to determine the centre to limb variation of the apparent source intensity, the brightness distribution over a scattered image and its time variability. Steinberg et al. (1971) describe the correlation of refractive index functions in an identical manner to Equation 2.34 with $M(r) = \exp(-r^2/r_0^2)$. They also introduce the variable

$$\varepsilon = \left(\frac{\langle \delta n^2 \rangle}{n} \right)^{1/2},$$

which is the root mean squared (r.m.s) relative fluctuation of electron density n and note that all observable quantities from their model vary as ε^2/r_0 only. For convenience, I will use the lower case n for electron density for the remainder of the section as the upper case N is needed to describe photon number, as we shall see.

The modelling by Steinberg et al. (1971) made some of the first predictions of the effect of radio wave scattering on the source size of a solar radio burst some of which are still used to date (e.g. Chrysaphi et al., 2018). Thejappa et al. (2007) were the first to perform a similar analysis using improved knowledge of the power spectrum of density fluctuations (Coles & Harmon, 1989). Modern treatments of radio wave scattering are done under a Fokker-Planck framework (Arzner & Magun, 1999; Bian et al., 2019). This approach is based on the Hamiltonian equations of the evolution of a wave vector

$\mathbf{k}$ and position $\mathbf{r}$

$$\frac{d\mathbf{r}}{dt} = v_g = \frac{\partial\omega}{\partial\mathbf{k}} = \frac{c^2}{\omega}\mathbf{k} \tag{2.37}$$

$$\frac{d\mathbf{k}}{dt} = -\frac{\partial\omega}{\partial\mathbf{r}} = -\frac{\omega_p}{\omega}\frac{\partial\omega_p}{\partial\mathbf{r}} \tag{2.38}$$

using the dispersion relation for an electromagnetic wave in a plasma given in Equation 2.28. The spectral number density (photon number) $N(\mathbf{k}, \mathbf{r}, t)$ can be described using a Fokker-Planck equation

$$\frac{\partial N}{\partial t} + \frac{d\mathbf{r}}{dt}\cdot\frac{\partial N}{\partial\mathbf{r}} + \frac{d\mathbf{k}}{dt}\cdot\frac{\partial N}{\partial\mathbf{k}} = \frac{\partial}{\partial k_i}D_{ij}\frac{\partial N}{\partial k_j} - \gamma N, \tag{2.39}$$

where k_i are the Cartesian coordinates of $\mathbf{k}$ and γ is the collisional absorption coefficient for radio waves in a plasma. The diffusion tensor, D_{ij}, is given by

$$\begin{aligned} D_{ij} &= \frac{\pi\omega_p^4}{4\omega^2}\int q_i q_j S(\mathbf{q})\delta(\mathbf{q}\cdot\mathbf{v}_g)\frac{d^3q}{(2\pi)^3} \\ &= \frac{\pi\omega_p^4}{4\omega c^2}\int q_i q_j S(\mathbf{q})\delta(\mathbf{q}\cdot\mathbf{k})\frac{d^3q}{(2\pi)^3}, \end{aligned} \tag{2.40}$$

where $\mathbf{q}$ is the wavevector of electron density fluctuations and $S(\mathbf{q})$ is the electron density fluctuation spectrum normalised to the relative density fluctuation variance

$$\varepsilon^2 = \int S(\mathbf{q})\frac{d^3q}{(2\pi)^3}. \tag{2.41}$$

Kontar et al. (2019) solve the Fokker-Planck equation 2.39 numerically for a spherical solar corona with an anisotropic spectrum of density fluctuations. They found that for particular values of ε and $\alpha = h_\perp/h_\parallel$, the ratio of perpendicular and parallel correlation lengths (the "micro-scale" or r_0 in the Chandrasekhar (1952) description of scattering), their results match the typical sizes of radio bursts measured in observations. Zhang et al. (2021) explored the parameter space of this scattering model further but obtained different values for ε and α.

The ultimate goal of scattering simulations and theory is to understand the microscopic processes in the solar corona. Observations of solar radio bursts provide and excellent opportunity to determine the plasma properties of the corona remotely. Thus, in the next chapter I detail one such instrument that can be used to this end and describe the mathematical background of radio interferometry and imaging.

3

Instrumentation and Interferometric Imaging

Solar Radio bursts in the corona can be studied in both spectra and images using observations from radio telescopes and interferometers. This chapter describes the instrumentation used throughout the work for this thesis, namely the LOw Frequency ARray (LOFAR). In order to study the spatial extent of radio bursts, a number of LOFAR stations are used together to create interferometric images. High temporal resolution spectra can be recorded using a single LOFAR station during "local mode". I begin with a description of the entire LOFAR array and give a detailed description of the digital signal processing pipeline of an international LOFAR station such as the Irish LOFAR station (I-LOFAR) in Birr, County Offaly. Finally, I outline the mathematical background for radio interferometry and give a brief description of a common deconvolution algorithm to generate interferometric images.

3.1 The LOw Frequency ARray (LOFAR)

The LOw Frequency ARray (LOFAR; van Haarlem et al., 2013) is a radio interferometer located in eight countries across Europe. The majority of the LOFAR stations exist in a dense cluster in the Netherlands known as the core. There are a total of 52 LOFAR stations; 24 core stations, 14 remote stations (also in the Netherlands), and 14 international stations (spread across Europe). The planned construction of an additional international station in Italy will increase this to a total of 53 LOFAR stations. A subset of densely packed core stations known as the "superterp" is shown in Figure 3.1. Although it is not dedicated to solar observations, LOFAR is the ideal instrument with which to observer solar radio bursts in the frequency range of 10 - 240 MHz. The temporal, spectral and spatial resolution are significantly improved upon the instruments first used to observe solar radio bursts from 60 years ago and, as

such, has reinvigorated the study of low frequency radio emission from the solar corona. In particular, the Solar and Space Weather Key Science Project (KSP) for LOFAR has secured observational time to overlap with the perihelion passes of both the Parker Solar Probe (PSP; Fox et al., 2016) and Solar Orbiter (Müller et al., 2020), allowing for simultaneous remote and *in situ* observations of coronal plasma at distances $< 10R_{\odot}$ for the first time in human history.

Figure 3.1: A dense collection of LOFAR core stations known as the "superterp". The large black tiles are the HBAs while the smaller grey squares mark the locations of the LBAs. A moat is dug around the superterp to keep the antennas above the ground water. Image credit ASTRON/LOFAR.

The frequency bandwidth of LOFAR is split into two bands, each observed with a different type of antenna, both of which can be seen in Figure 3.1. The range 10 - 90 MHz is observed with the Low Band Antennas (LBAs) and the range 110 - 240 MHz is observed with the High Band Antennas (HBAs). The gap between the two bands is included to avoid observing in the FM band, which is dominated by noise from commercial radio broadcasting. The observations in Chapters 5 and 6 were made

using the LBAs while monitoring of solar radio activity with the I-LOFAR uses both the LBAs and HBAs simultaneously, as discussed in section 3.2. I now discuss the antennas and recording process for an international LOFAR station.

3.1.1 Low Band Antenna

The LBA is a cross-dipole antenna in an inverted V shape consisting of two lengths of orthogonal copper wire. This enables measurements from two linear polarisations in the X and Y direction. LBAs are oriented such that the X polarisation is in the Northeast to Southwest direction while the Y polarisation runs Northwest to Southeast. Each wire is connected to a low-noise amplifier inside of a radio frequency interference (RFI) shielded moulding on top of a 1.7m PVC pipe. The pipe is kept upright under tension from the wires which are attached to the ground with synthetic imrubber straps and polyester rope. The LBA is placed on top of a steel ground plane made out of concrete reinforcement rods, which acts as a reflector for radio light. Figure 3.2 shows LBAs at I-LOFAR. The low-noise amplifiers receive power over two coaxial cables, which also carry signals measured from the LBA.

Each arm of the dipole is 1.38m long which results in a 52MHz resonance peak however, due to the impedance of the amplifier, this is increased to 58MHz. A typical LBA power spectrum showing this resonance peak can be seen in Figure 3.3.

3.1.2 High Band Antenna

The spectrum above the FM band is observed by the HBA. In order to reduce system noise, the HBA design is drastically different to the simple design of the LBA. One HBA is a 5m x 5m tile consisting of a 4 $\times$ 4 array of 16 bow-tie cross dipole antenna elements supported in an expanded polystyrene structure. The HBA sits on top of a 5cm $\times$ 5cm wire mesh ground plane, which acts as a reflector to radio waves at these higher frequencies. The HBA tile is encased in two overlapping polypropylene foil layers in order to protect it from the weather. Figure 3.5 shows a fully assembled

Figure 3.2: Low Band Antennas on a rare sunny day at I-LOFAR. These dipole antennas observe between 10 and 90 MHz. The dipoles are connected to a preamplifier on top of a PVC pipe via coaxial cables which run underground to the station container in the background.

HBA tile before the tile lid is placed. The 4×4 grid of antenna elements expanded polystyrene structure is clearly seen.

Each antenna element in a HBA tile is connected to a front-end which performs preamplification and analogue beamforming. Each front-end is then connected to a summator (one for each polarisation) where the signals from all antenna elements are summed before being sent for further signal processing in the station container, see section 3.2.1. The effect of analogue beamforming means that HBA observations are only sensitive to particular directions on the sky. Further to this, the regular gridding of the antenna elements leads to diffraction effects which makes all sky imaging with HBAs

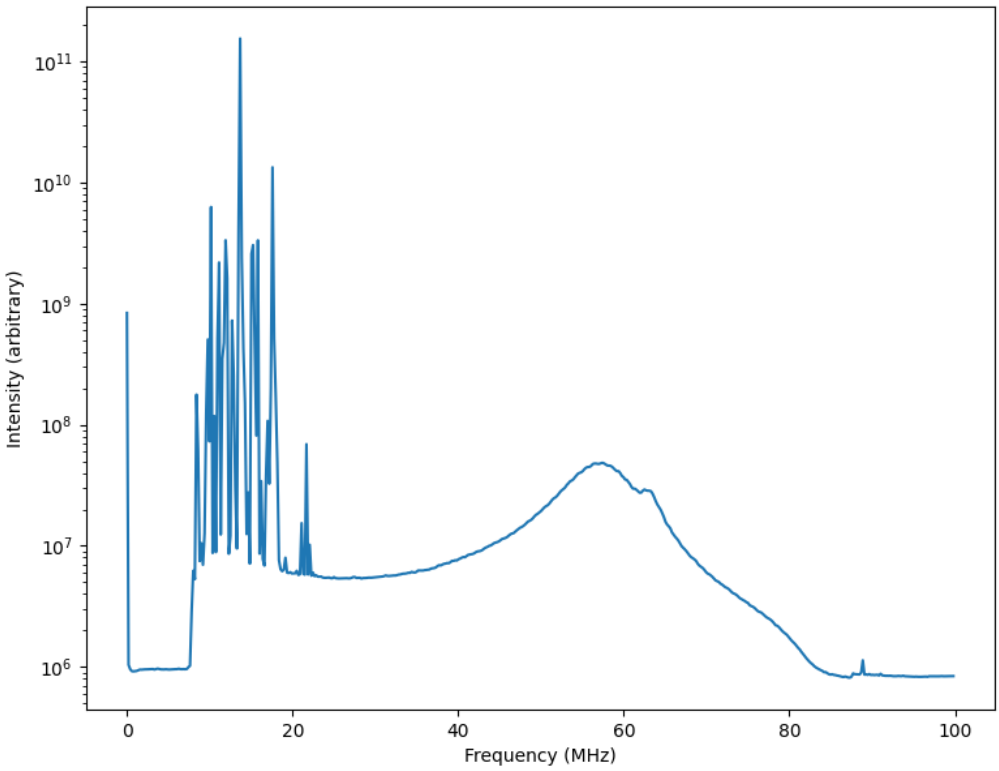

Figure 3.3: Typical power spectrum for an LBA. The x axis shows frequency in MHz while the y axis is the intensity in arbitrary units. The peak at 58 MHz is determined by the length of the dipole arms and the impedance of the low-noise amplifier. The 'knee' in the spectrum at ~ 63 MHz is due to the wires being turned up at the ends.

a less common observation type. The diffraction effects can be minimised by randomly excluding antenna elements however this reduces the sensitivity of such observations.

3.1.3 Remote Station Processing Boards (RSPs)

The Remote Station Processing boards (RSPs) perform the bulk of digital signal processing in a LOFAR station. Each LOFAR station consists of 24 RSP boards capable of channelising, beamforming and correlating raw voltage data recorded by either the LBAs or HBAs. A polyphase filter converts recorded data into 1024 complex subband signals which, because the signal is real, is fully described by the positive 512 subbands. These 512 subbands offer $\sim$ 195kHz frequency resolution across the band. In order to perform beamforming, all RSPs are connected together in a ring. Data is passed along

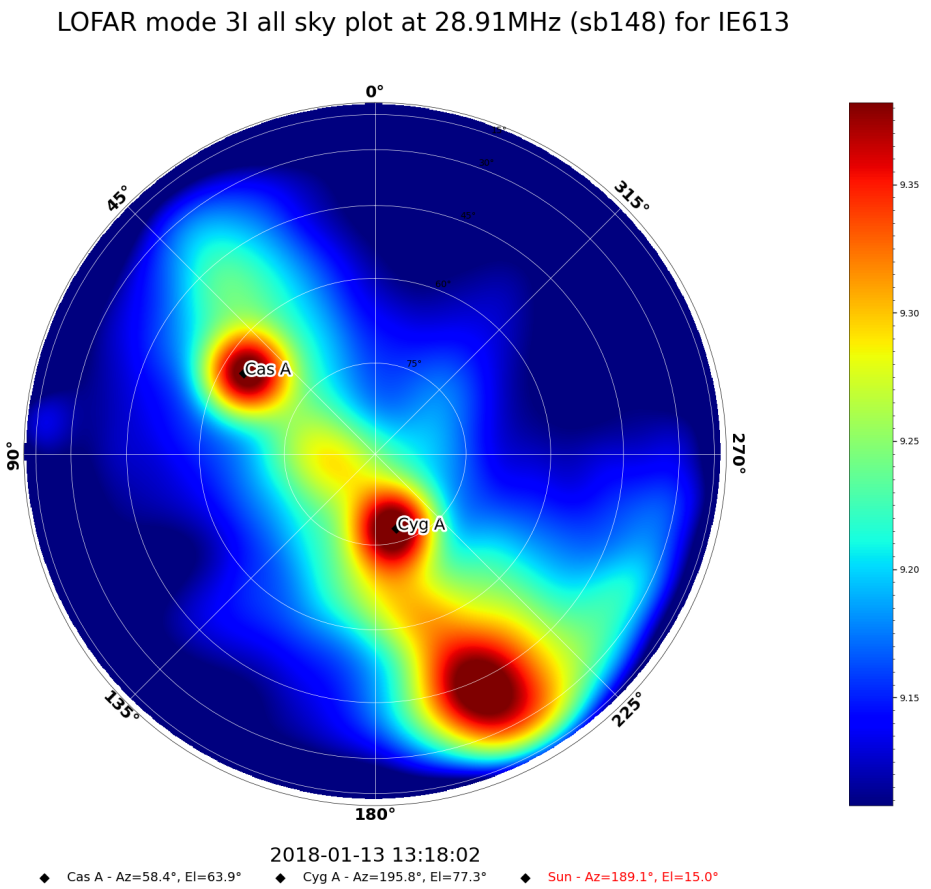

Figure 3.4: An all-sky image taken with I-LOFAR LBAs at 28.91 MHz. The wide field of view of the LBAs allows the entire sky to be imaged at once. The colourbar shows intensity in arbitrary units. The positions of Cassiopeia A and Cygnus A are shown to line up well with the brightest parts of the image.

this ring and summed in each RSP where a phase correction is also applied in order to "point" the telescope beam. A maximum of 488 subbands can be used to create beamlets, beams pointed in a particular direction observing in a particular frequency. Data from this process is streamed to an external storage node from 4 points in the ring (i.e. from 4 RSPs) each containing one quarter of the beamlets computed by the RSP boards. Figure 3.7 shows a single RSP board from I-LOFAR.

3.1.4 Transient Buffer Boards (TBBs)

One of the lesser-used pieces of LOFAR hardware are the Transient Buffer Boards (TBBs). TBBs are RAM buffers that can temporarily store data at its natively sampled 5ns time resolution. Each LOFAR station contains a total of 12 TBBs ranging from

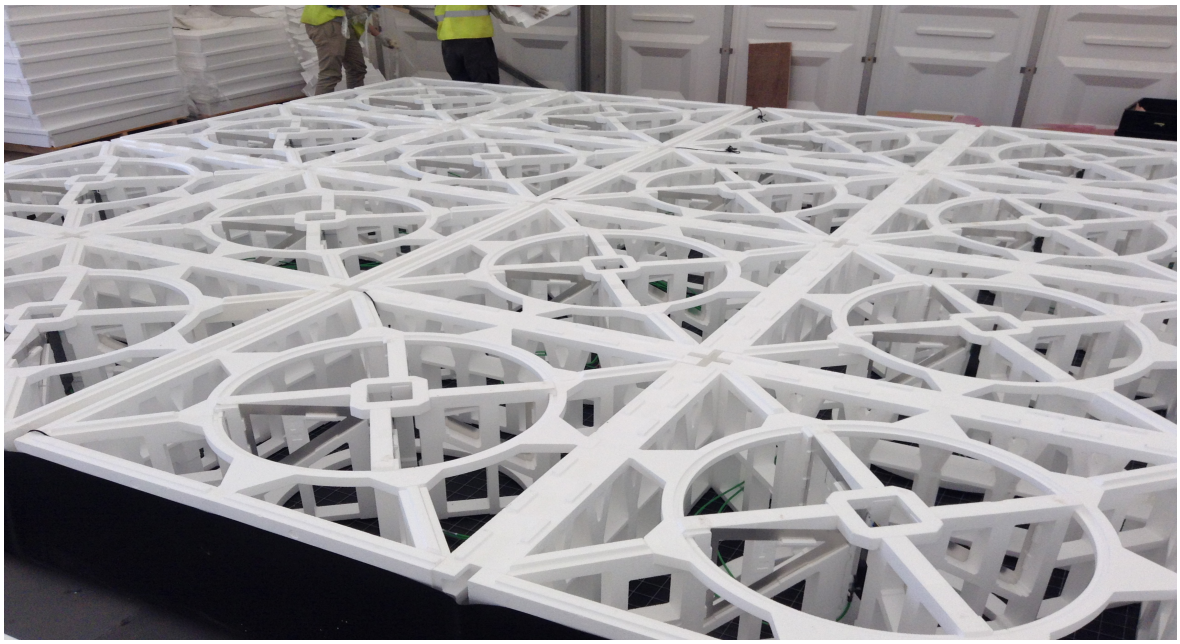

Figure 3.5: A High Band Antenna before the tile lid has been placed. These antennas measure radio frequencies from 110 - 240 MHz. The 4 × 4 grid of bow-tie cross dipole antenna elements is clearly visible inside the expanded polystyrene casing.

1 GB to 32GB of memory. More recently completed stations such as I-LOFAR have 32GB TBBs while the older Dutch stations usually have less than 16GB. A 32GB TBB can store up to 5 seconds worth of data recorded by a LOFAR station although this can be increased if fewer inputs or polarisations are recorded. TBBs are currently used in analysing cosmic ray showers (Mulrey et al., 2020) and lightning storms (Hare et al., 2018) but have yet to become a mainstream tool for solar physics, despite their potential. Recording the radio Sun at 5ns has never been attempted before and as such could offer a wealth of never before studied phenomena or cast new light onto long standing questions. While the next generation telescopes like the Square Kilometre Array (SKA) and the Murchison Widefield Array (MWA) sample at higher rates than 5ns, none of them store full time resolution data. This gives LOFAR the unprecidented abiltiy to capture transient events at the highest temporal resolution ever. Figure 3.8 shows a single TBB.

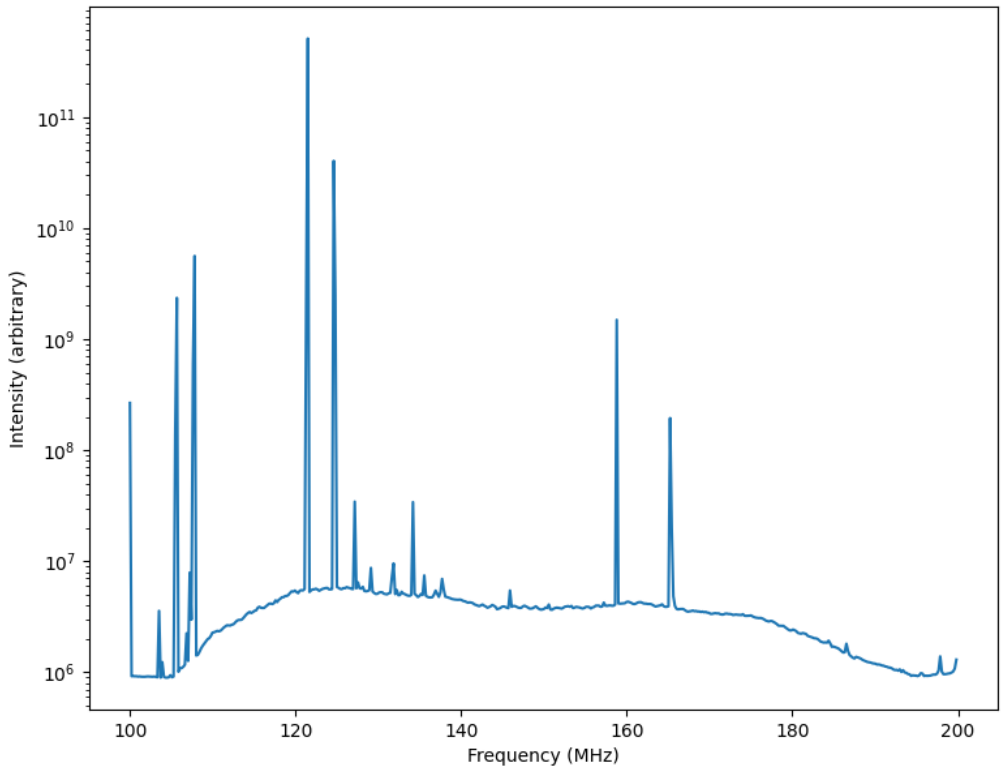

Figure 3.6: Typical power spectrum for a HBA in the frequency range 100 - 200 MHz. The x axis shows frequency in MHz while the y axis is the intensity in arbitrary units. Large peaks here are typically associated with noise from digital audio broadcasting (DAB) radio and other sources of RFI.

3.2 I-LOFAR: The Irish LOw Frequency ARray

Construction of the Irish LOFAR station (I-LOFAR) was completed in July 2017 on the demesne of Birr Castle, County Offaly, in the Irish Midlands. An international LOFAR station such as I-LOFAR consists of 96 dual-polarisation dipole antennas known as Low Band Antennas (LBAs) which record radio frequencies of 10 MHz to 90 MHz and 96 High Band Antenna (HBA) tiles which each contain 16 bow-tie antennas connected to an analogue summator and record in the frequency range 110 MHz to 250 MHz (see van Haarlem et al., 2013, for a full description of LOFAR antennas). In the following values are given for a clock frequency of 200 MHz, values in brackets are for a clock frequency of 160 MHz. Data recorded by the antennas are then channelised into 512

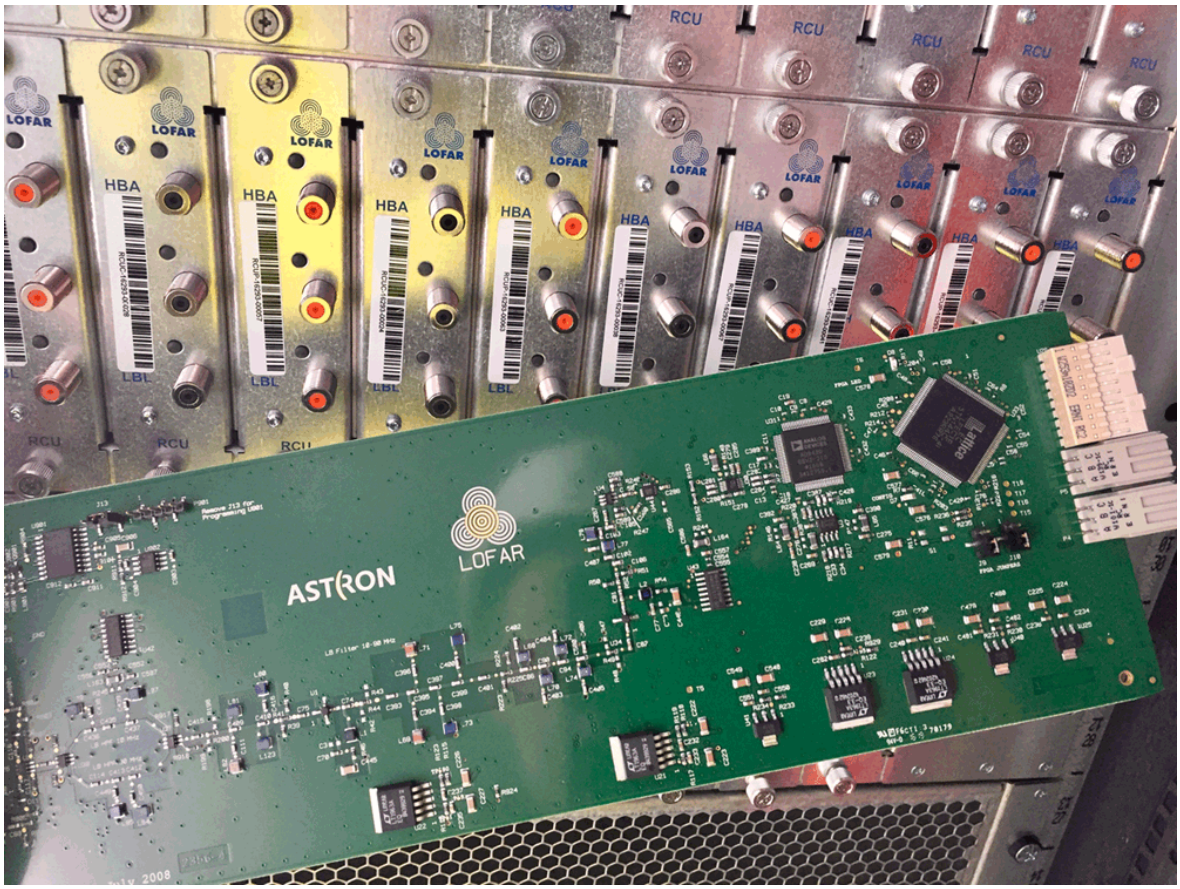

Figure 3.7: A Remote Station Processing board from I-LOFAR. This is used to perform beamforming with the array and to channelise incoming data.

subbands of 195.3125 kHz (156.25 kHz) frequency resolution at 5.12 µs (6.4 µs) temporal resolution depending on the clock rate used to sample data, either 200 MHz or 160 MHz (van Haarlem et al., 2013). The signal from each antenna is then digitally beamformed (BF) to a direction on the sky to create beamlets. A beamlet is a specific location on the sky observed at a specific subband. An international LOFAR station can record and process data in either 8 bits or 16 bits, corresponding to a maximum of 488 or 244 beamlets respectively because the lower bit rate allows for a greater number of beamlets to be recorded. The term to describe how many bits are used during an observation is the bitmode. It is also possible to record and process at 4 bits. Beamlets are recorded at 3.2 Gbps. When I-LOFAR is in local mode, the BF data is sent along a fibre connection to a local control room. Figure 3.9 shows an aerial photograph of I-LOFAR.

The total available bandwidth for I-LOFAR (and other international LOFAR sta-

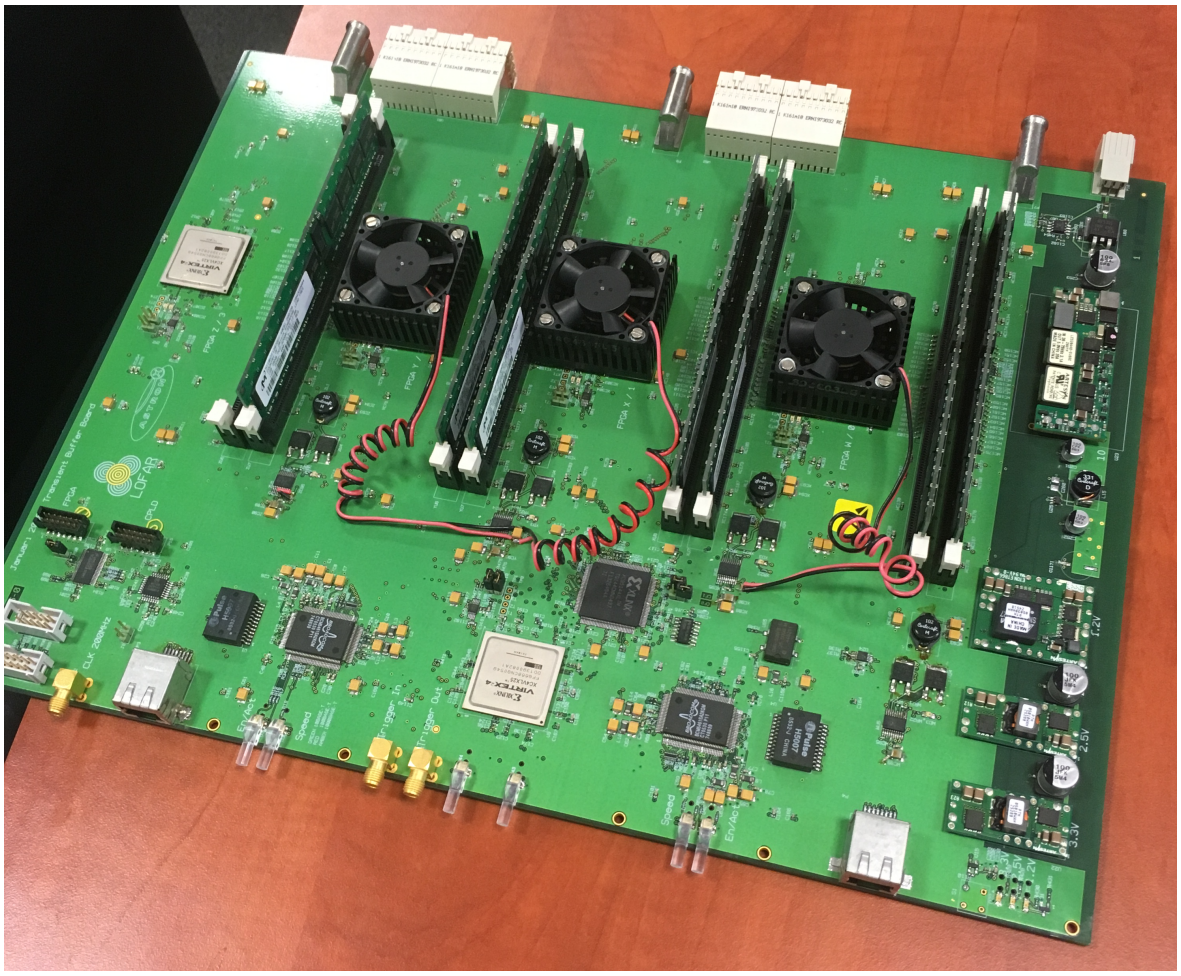

Figure 3.8: A photograph of a Transient Buffer Board taken at the LOFAR data school 2018. This is used to store up to 5 s of raw voltages from LOFAR antennas at 5 ns temporal resolution.

tions) observations is determined by the bitmode used. This corresponds to a bandwidth of ~ 47 $(95, 190)$ MHz for 16 (8, 4) bit data. However, it is not necessary that the frequencies of each beamlet be sequential, which allows a wider range of frequencies to be achieved. This is utilised in 'mode 357', developed at the Kilpisjärvi Atmospheric Imaging Receiver Array (KAIRA; McKay-Bukowski et al., 2015). In mode 357, beamlets are formed such that 200 beamlets from 10 MHz to 90 MHz, 200 beamlets from 110 MHz to 190 MHz and 88 beamlets from 210 MHz to 240 MHz are recorded. In order to achieve this recording scheme, the number of antennas used for each frequency range is reduced. This leads to a lower sensitivity in mode 357. Mode 357 is particularly useful for observations of solar radio bursts, which typically occur across the entire LOFAR spectrum.

I-LOFAR produces a number of one second temporal resolution statistics files which

are stored locally on the station's Local Control Unit (LCU). These are sub-band statistics (SSTs), which give the power spectrum for each antenna, beamlet statistics (BSTs), which give the power in each beamlet formed by the LOFAR station, and crosslet statistics (XSTs), the correlation coefficients between each antenna. These low-resolution data can be employed for system monitoring but are also sufficient for some astrophysical applications, for example, the XST data can be used to create snapshot all-sky images, and BST data have been used to study solar radio bursts (Maguire et al., 2020). The desire to use the full capabilities of the station, by accessing the full resolution is the motivation to develop a computational backend for the capture, processing, and storage, of stand-alone BF data.

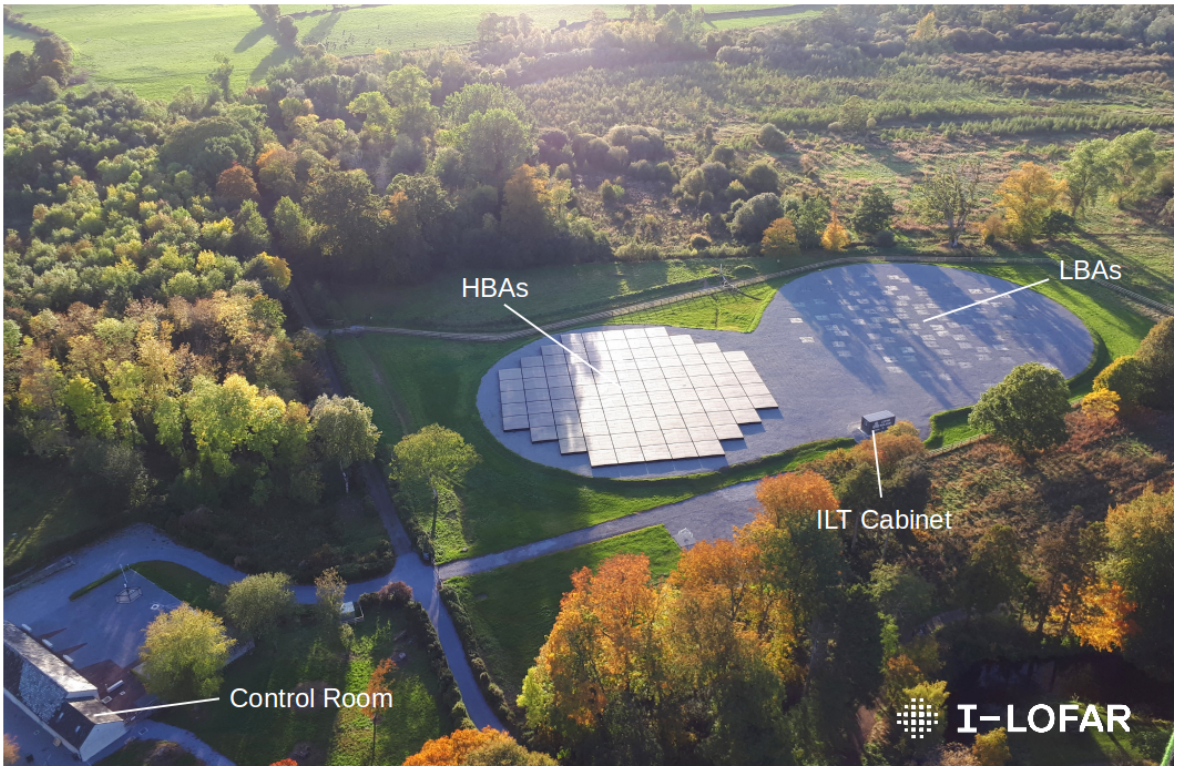

Figure 3.9: Aerial photograph of the Irish Low Frequency Array station IE613 (I-LOFAR) at Birr Castle, County Offaly. Data from the LBAs and HBAs are transferred to the ILT Cabinet (centre right) via coaxial cables where they are amplified, filtered and digitised. In international mode, data are transported to Groningen in the Netherlands at ∼3.2 Gbps. In local mode, data are processed using REALTA in the I-LOFAR Control Room (bottom left). Image credit: Alison Delaney (Birr Castle).

One of the many benefits to using LOFAR as a radio telescope is that each station can be used independently in Single Station Mode which, in the case of international stations, gives freedom to the host countries to make specific observations that may

not be covered in a LOFAR observing cycle. Not only this, but Single Station mode offers the flexibility of the raw complex voltage data before it has passed through any averaging or calibration pipelines that occur during international observing mode.

This allows direct access to raw voltage data meaning any form of data processing imaginable can be performed. The only limit to this is the computer power and data storage available, two extremely non-trivial problems with LOFAR data. Recording complex raw voltage data from the RSPs requires a 10Gbps fibre optic link between the LOFAR cabinet and a powerful computer cluster. Due to the unpredictable nature of solar radio bursts, the only way to guarantee they will be recorded is to observe for many hours. Data quickly become terabytes in size which becomes challenging to perform any amount of post-analysis. Another disadvantage of using Single Station mode is that, because the main appeal of LOFAR are its long baseline capabilities, little has been developed for Single Station use which only has a maximum baseline of $\sim$ 300m. However, for spectral work this is less of an issue.

3.2.1 Digital Signal Processing for a Single LOFAR Station

The LOFAR digital signal processing pipeline for a single station is outlined in Figure 3.10. Analogue signal is received by the HBAs or LBAs. This is sampled at 200 MHz and converted to a digital signal by a 12 bit A/D converter inside the station's Receiver Units (RCUs). Each RCU digitises data for 1 antenna feed (X or Y polarisation) so there are $96 \times 2 = 192$ RCUs in total. The digitised data is then sent to the RSP boards. In a standard LOFAR observation while the station is in International LOFAR Telescope (ILT) mode, data from 8 RCUs are channelised into 512 subbands by a polyphase filter bank. This results in raw complex voltage data at 195.3125kHz frequency resolution and 5.12μs temporal resolution which are then phase shifted and added together in order to beamform to a particular location on the sky (see 3.3.1). The output from each of the 24 RSP boards are added in a ring before being sent along a 10Gbps fibre link to Groningen and passed into the COBALT2.0 processing cluster where the data can be further channelised and correlated to produce interferometric

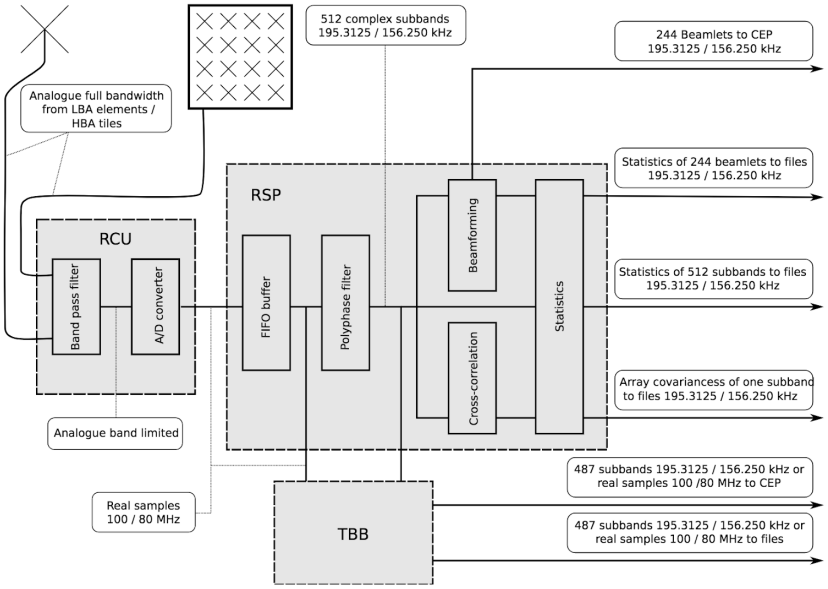

Figure 3.10: Digital signal processing pipeline of an individual LOFAR station. Data is first digitised in the ReCiever Unit (RCU) before being sent to the RSP board. Here data is channelised by a polyphase filter and beamformed before being sent to the CEntral Processor (CEP) in the Netherlands. Also featured is the TBB which stores data in a ring buffer unless it is read out to an external storage system.

or beamformed data products. The digital signal processing pipeline is much the same in Single Station Mode, however data is averaged out to 1 second before being saved as various "statistics" files. These include subband statistics, which give the power spectrum for each antenna; beamlet statistics, give the power in each beamlet formed by the LOFAR station; and crosslet statistics, the correlation coefficients between each antenna which can be used to create all sky images. Parallel to this, the raw voltage signal with the full 5ns temporal resolution is stored in the memory of a TBB. A single LOFAR station has 12 TBBs which each take 2 RSP boards as inputs. The buffer will constantly overwrite itself until it is frozen and dumped either by an internal/external trigger signal or through sending a dump command manually.

3.3 Radio Interferometry

Rayleigh's criterion states that for an object to be resolved, the maximum of its interference pattern must overlap the minimum of another. This leads to the mathematical

relationship (assuming a circular aperture),

$$\theta \approx 1.22\frac{\lambda}{D}$$

where θ is the angular resolution of an object, λ is the wavelength observed in and D is the aperture diameter of the telescope. For telescopes observing optical wavelengths, this limit is often superseded by the "seeing" of the atmosphere. Adaptive optics help overcome this challenge and bring optical telescopes close to the diffraction limit. For radio telescopes at low frequencies, the challenge becomes one of structural engineering. For a radio telescope observing at 30 MHz to have a similar resolution to the Hubble Space telescope, for example, it would need an aperture diameter of 41,000 km. Fortunately, two radio antennas placed some distance apart has the same angular resolution as single dish with the same diameter. This technique is known as radio interferometry and to explain how it works I first discuss the coherence of the electric field of an astronomical object before introducing the most fundamental radio interferometer, the two element interferometer.

An astronomical object at some position $\mathbf{R}$ radiating radio electromagnetic waves with a time variable electric field of the form $\mathbf{E}(\mathbf{R}, t)$ is observed by an astronomer at some point $\mathbf{r}$. In order to disregard the time variable nature of the electric field we consider only the coefficients of the Fourier series of $\mathbf{E}(\mathbf{R}, t)$ which we denote as $\mathbf{E}_\nu(\mathbf{R})$, the quasi-monochromatic components of $\mathbf{E}(\mathbf{R}, t)$ at frequency ν, and note that these are complex values (Taylor et al., 1999). We make the assumption that the object is sufficiently far away so that the field strength of the source can be described as the field strength on some imaginary "celestial sphere" with radius $R = |\mathbf{R}|$ within which there is no additional radiation. The field strength observed at $\mathbf{r}$ can be expressed in terms of the field strength on this sphere, $\mathcal{E}_\nu(\mathbf{R})$, via

$$E_\nu(\mathbf{r}) = \int \mathcal{E}_\nu(\mathbf{R}) \frac{e^{2\pi i\nu|\mathbf{R}-\mathbf{r}|/c}}{|\mathbf{R}-\mathbf{r}|} dS, \tag{3.1}$$

where dS is the surface area element on the celestial sphere. The correlation of the field

at two points $\mathbf{r}_1$ and $\mathbf{r}_2$ is defined as $\mathsf{V}_\nu(\mathbf{r}_1, \mathbf{r}_2) = \langle E_\nu(\mathbf{r}_1) E_\nu^*(\mathbf{r}_2) \rangle$, where the asterisk denotes the complex conjugate. Substituting in Equation 3.1 gives

$$\mathsf{V}_\nu(\mathbf{r}_1, \mathbf{r}_2) = \left\langle \int\int \mathcal{E}_\nu(\mathbf{R}_1) \mathcal{E}_\nu^*(\mathbf{R}_2) \frac{e^{2\pi i\nu|\mathbf{R}_1 - \mathbf{r}_1|/c}}{|\mathbf{R}_1 - \mathbf{r}_1|} \frac{e^{-2\pi i\nu|\mathbf{R}_2 - \mathbf{r}_2|/c}}{|\mathbf{R}_2 - \mathbf{r}_2|} dS_1 dS_2 \right\rangle. \tag{3.2}$$

If we assume that the radiation from the astrophysical source is spatially incoherent, then $\langle \mathcal{E}_\nu(\mathbf{r}_1) \mathcal{E}_\nu^*(\mathbf{r}_2) \rangle = 0$ for $\mathbf{R}_1 \neq \mathbf{R}_2$ and Equation 3.1 can be simplified to

$$\mathsf{V}_\nu(\mathbf{r}_1, \mathbf{r}_2) = \int \langle |\mathcal{E}_\nu(\mathbf{R})^2| \rangle |\mathbf{R}|^2 \frac{e^{2\pi i\nu|\mathbf{R} - \mathbf{r}_1|/c}}{|\mathbf{R} - \mathbf{r}_1|} \frac{e^{-2\pi i\nu|\mathbf{R} - \mathbf{r}_2|/c}}{|\mathbf{R} - \mathbf{r}_2|} dS. \tag{3.3}$$

By introducing the unit vector $\mathbf{s} = \mathbf{R}/|\mathbf{R}|$ and writing the observed intensity $I_\nu(\mathbf{s}) = \rangle \mathcal{E}_\nu(\mathbf{r})^2 | \rangle |\mathbf{R}|^2$ and ignoring terms of order $|\mathbf{r}/\mathbf{R}|$, such that

$$|\mathbf{R} - \mathbf{r}| = \sqrt{|\mathbf{R}|^2 + |\mathbf{r}|^2 - 2\mathbf{r} \cdot \mathbf{R}} \approx |\mathbf{R}| - \frac{\mathbf{r} \cdot \mathbf{R}}{|\mathbf{R}|},$$

we finally arrive at a useful form of $\mathsf{V}_\nu(\mathbf{r}_1, \mathbf{r}_2)$

$$\mathsf{V}_\nu(\mathbf{r}_1, \mathbf{r}_2) \approx \int I_\nu(\mathbf{s}) e^{-2\pi i\nu \mathbf{s} \cdot (\mathbf{r}_1 - \mathbf{r}_2)/c} d\Omega, \tag{3.4}$$

where the surface element dS is given by $|\mathbf{R}|^2 d\Omega$.

The most important conclusion to draw from Equation 3.4 is that it depends only on the distance between the two points, not their absolute position. Thus, $\mathsf{V}_\nu(\mathbf{r}_1, \mathbf{r}_2)$ can be determined from only one pair of points. The function V_ν for a single separation $\mathbf{r}_1 - \mathbf{r}_2$ is called the spatial coherence function and is all that needs to be measured to study the emitting astronomical source.

How then does one measure the spatial coherence function? Let's imagine putting two radio antennas (antenna 1 and antenna 2) at points $\mathbf{r}_1$ and $\mathbf{r}_2$. The vector distance between these antennas is given by $\overrightarrow{\mathbf{b}} = \mathbf{r}_1 - \mathbf{r}_2$. As shown in Figure 3.11, a radio wave approaching the antennas from direction $\hat{\mathbf{s}}$ will hit antenna 2 first then antenna

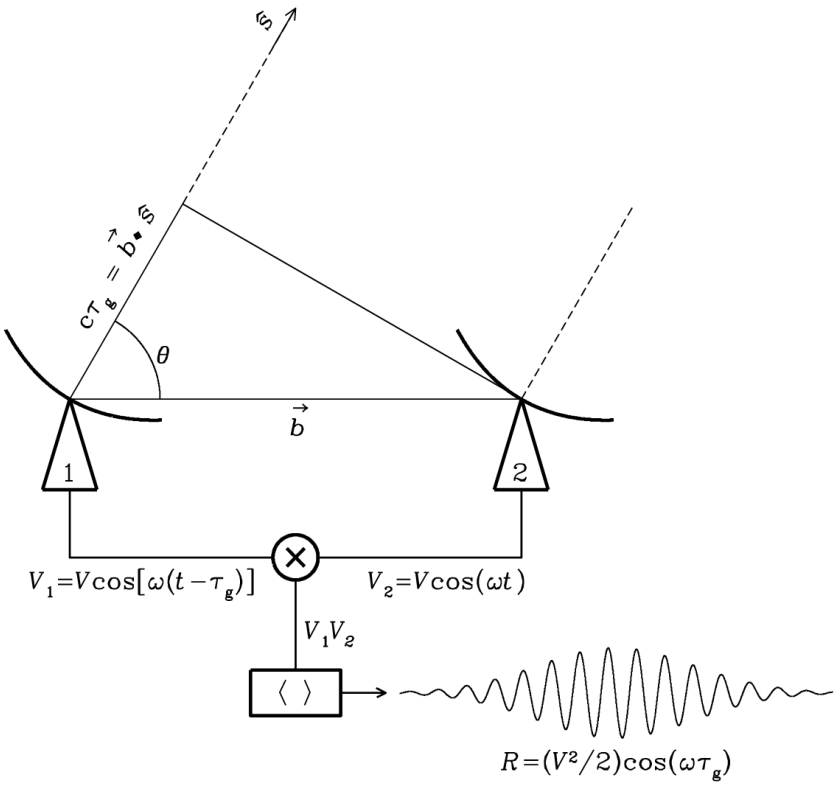

Figure 3.11: A two element interferometer separated by a baseline $\vec{\mathbf{b}}$. The signal reaches antenna 1 a time of τ_g after it reaches antenna 2. The signal from each antenna is correlated by first multiplying the two voltages then time averaging them. This gives a cosine response R_c. Figure from Condon & Ransom (2016).

1 after a time delay of τ_g such that,

$$\tau_g = \frac{\vec{\mathbf{b}} \cdot \hat{\mathbf{s}}}{c} \tag{3.5}$$

where c is the speed of light. The output from each antenna is a voltage $V_1 = V\cos\omega(t-\tau_g)$ and $V_2 = V\cos\omega t$.

The total response, R_c of the interferometer is the correlation or multiplication and time average of these two voltages, $\langle V_1 V_2 \rangle$.

$$R_c = \langle V_1 V_2 \rangle = \frac{V^2}{2}\cos\omega\tau_g$$

Furthermore, if a 90° phase shift is added to the output of one antenna, the response

becomes

$$R_s = \langle V_1 V_2 \rangle = \frac{V^2}{2} \sin \omega \tau_g.$$

A complex visibility can be defined as the complex sum of the two responses $V(\hat{\mathbf{s}}) = R_c - iR_s$. Using Euler's formula, the complex visibilty of an extended source, at a particular frequency, is given by:

$$V_\nu(\hat{\mathbf{s}}) = \int I_\nu(\hat{\mathbf{s}}) \exp(-i\omega\tau_g) d\Omega = \int I_\nu(\hat{\mathbf{s}}) \exp(-2\pi i \frac{\overrightarrow{\mathbf{b}} \cdot \hat{\mathbf{s}}}{\lambda}) d\Omega \tag{3.6}$$

where I_ν is the sky brightness distribution at frequency ν. Notice now how Equation 3.6 is identical to Equation 3.4 once it has been rewritten in terms of wavelength. Thus, the output of a complex correlator *is* the spatial coherence function!

We now choose a convenient coordinate system to describe this measurement. In this coordinate system, the separation between antennas is measured in terms of wavelength $\mathbf{r}_1 - \mathbf{r}_2 = \lambda(u, v, w = 0)$ and the components of the unit vector $\mathbf{s}$ become $(l, m, n = 1)$. In this uvw coordinate system, $d\Omega$ becomes $dldm$ and Equation 3.6 becomes

$$V_\nu(u, v) = \int I_\nu(l, m) e^{-2\pi i(ul+vm)} dldm. \tag{3.7}$$

Here we see that the complex visibility (a.k.a spatial coherence function) is the Fourier transform of the sky brightness distribution.

Before describing how to invert this Fourier transform, I take a moment to describe the uvw coordinate system a bit further. As we saw, the components of the unit vector $\mathbf{s}$ of the source in the sky are given by *(l,m,n)*. These are directional cosines and determine a position on the sky in terms of the direction cosines to that position. First we introduce the concept of a *phase centre*, a position on the sky to which the main response of the antennas is pointed either by physically steering the antennas or introducing appropriate phase delay in the correlation described above. *l,m,n* can then

be defined as

$$
\begin{aligned}
l &= \cos\delta \sin\Delta\alpha \\
m &= \sin\delta \cos\delta_0 - \cos\delta \sin\delta_0 \cos\Delta\alpha \\
n &= \sqrt{1 - l^2 - m^2}
\end{aligned}
$$

where δ, δ_0 are the declinations of an object and the phase centre, respectively, and $\Delta\alpha = \alpha - \alpha_0$ is the difference between the right ascension of the object and the right ascension of the phase centre.

Baselines in radio interferometry are described using the uvw coordinate system. For baseline $\overrightarrow{\mathbf{b}} = \mathbf{r}_1 - \mathbf{r}_2$ where the compenents of $\mathbf{r}$ are (x, y, z), the uvw coordinates can be found from the matrix below.

$$
\begin{bmatrix} u \\ v \\ w \end{bmatrix} = \frac{1}{\lambda} \begin{bmatrix} \sin H & \cos H & 0 \\ -\sin\delta\cos H & \sin\delta\sin H & \cos\delta \\ \cos\delta\cos H & -\cos\delta\sin H & \sin\delta \end{bmatrix} \begin{bmatrix} b_x \\ b_y \\ b_z \end{bmatrix}
$$

Here, H is the hour angle of an object, δ is its declination, $\overrightarrow{\mathbf{b}} = (b_x, b_y, b_z) = (x_2 - x_1, y_2 - y_1, z_2 - z_1)$ is the baseline or distance between two antennas and λ is the wavelength of the radio waves being observed. An often appropriate assumption to make for interferometers of short enough baselines is that all measurements are made in a plane where $w = 0$ called the uv plane.

So far I've been vague as to how to invert our measurement of complex visibilities into an image of the observed object, commenting only that they are the Fourier transform of each other. One would think then that one can simply perform the inverse Fourier transform via the readily available fast Fourier transform (FFT) algorithm. Unfortunately, this is only the case if uv space is perfectly sampled . In real life, when measuring the spatial coherence function with a two element interferometer, we do so for one position in uv space only. Adding more antennas to our interferometer will add more points to the uv plane, though in reality it will remain sparsely sampled. We can

represent the sampling of the uv plane by a sampling function $S(u,v)$ which is zero everywhere, except for the baseline positions, i.e. a collection of dirac deltas. We then represent the Fourier transform of our sampled visibilities as a *dirty image*

$$I_\nu^D(l,m) = \int\int V_\nu(u,v)S(u,v)e^{2\pi i(ul+vm)}dudv. \tag{3.8}$$

By use of the convolution theorem we see that

$$I_\nu = I_\nu^D * B \tag{3.9}$$

where B is the point spread function (PSF) of the interferometer or, in other words, the Fourier transform of the sampling function

$$B(l,m) = \int\int S(u,v)e^{2\pi i(ul+vm)}dudv. \tag{3.10}$$

Figure 3.12 shows the relationship between $I_\nu^D(l,m)$, $I_\nu(l,m)$, $V_\nu(u,v)$ and $S(u,v)$. We will discuss methods for undoing this convolution shortly but first, a brief digression on the topic of beamforming with a phased array interferometer such as LOFAR.

3.3.1 Phase Delays and Beamforming

For steerable antennas, pointing at a phase centre is simply a matter of steering the antennas to that direction. For phased arrays such as LOFAR, and in particular the LBAs, this is unsurprisingly not possible. Instead, a time delay is digitally added to the signal from each antenna. For example, in order to maximise the response of the two element interferometer in Figure 3.11 to the direction $\hat{\mathbf{s}}$, a delay of $\tau_0 = \tau_g$ must be added to the signal of antenna 2. This is illustrated in Figure 3.13.

Beamforming is a signal processing technique whereby all the signals are added together coherently to give a maximum sensitivity in a particular direction. The beamformed signal at the phase centre (subscript pc) can be described as (Chen et al.,

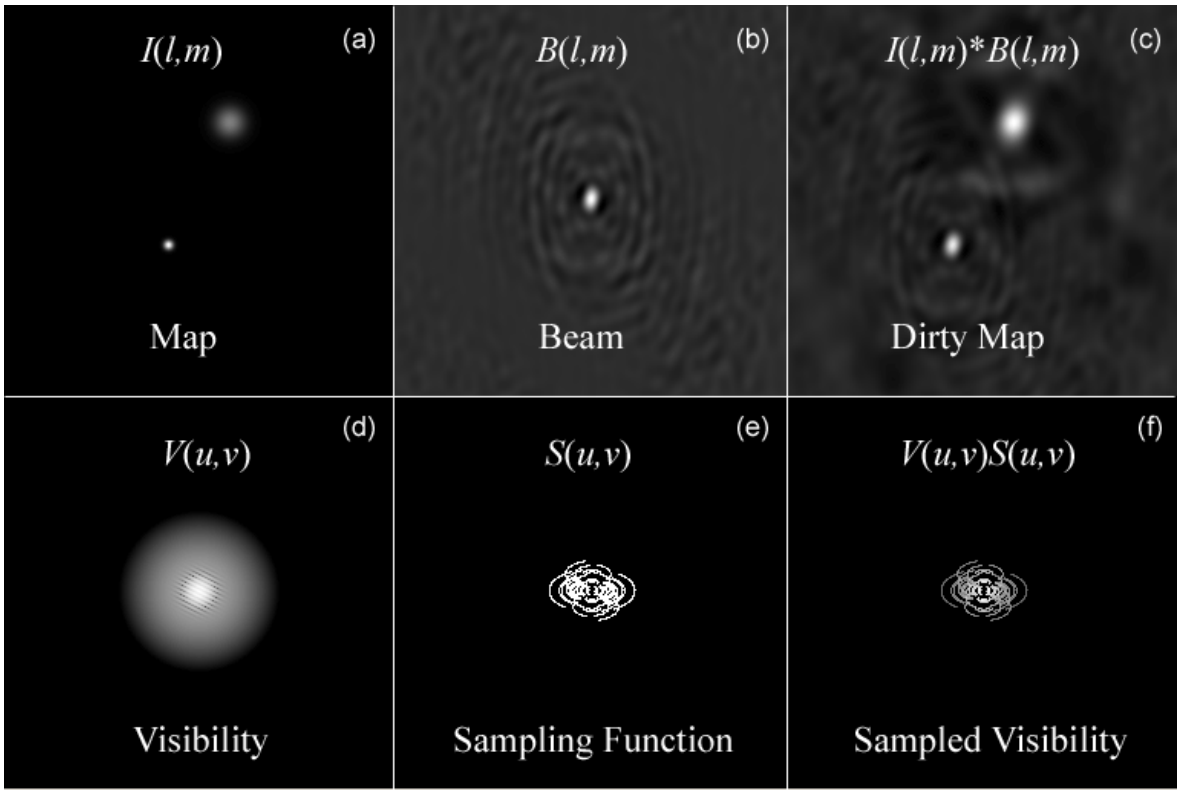

Figure 3.12: The Fourier relationship between visibilities and a radio image. Panels along the top are the Fourier transform of panels along the bottom. Panel a shows a model sky brightness distribution, panel b is the PSF or beam of the interferometer and panel c is the dirty image. Panel d is the model visibilities of the sky, panel e is the sampling function and panel f shows the sampled visibilities. Figure from Dale Gary's radio astronomy course.

2021)

$$F(t_{pc}) = \sum_{n=1}^{N} f(t_{pc} - \tau_n) w(\tau_n) \tag{3.11}$$

for an array of N antennas. Here the a delay correction $w(\tau_n)$ is made to the signal from each antenna $f(t_{pc} - \tau_n)$ before they are summed together. The time delay τ_n has the same form as Equation 3.5 for $\overrightarrow{\mathbf{b}} = \mathbf{r}_n - \mathbf{r}_{pc}$. Beamforming is implemented on LOFAR in a slightly different manner. Rather than correct this delay in the time domain, the Fourier transform of the outputs of each antenna are multiplied by a phase delay $e^{-i\omega\tau}$ before being summed.

3.3.2 Image Deconvolution

We now return to the discussion of radio interferometric imaging. Real measurements from interferometers are bound to contain some amount of noise, ϵ. Thus, Equation

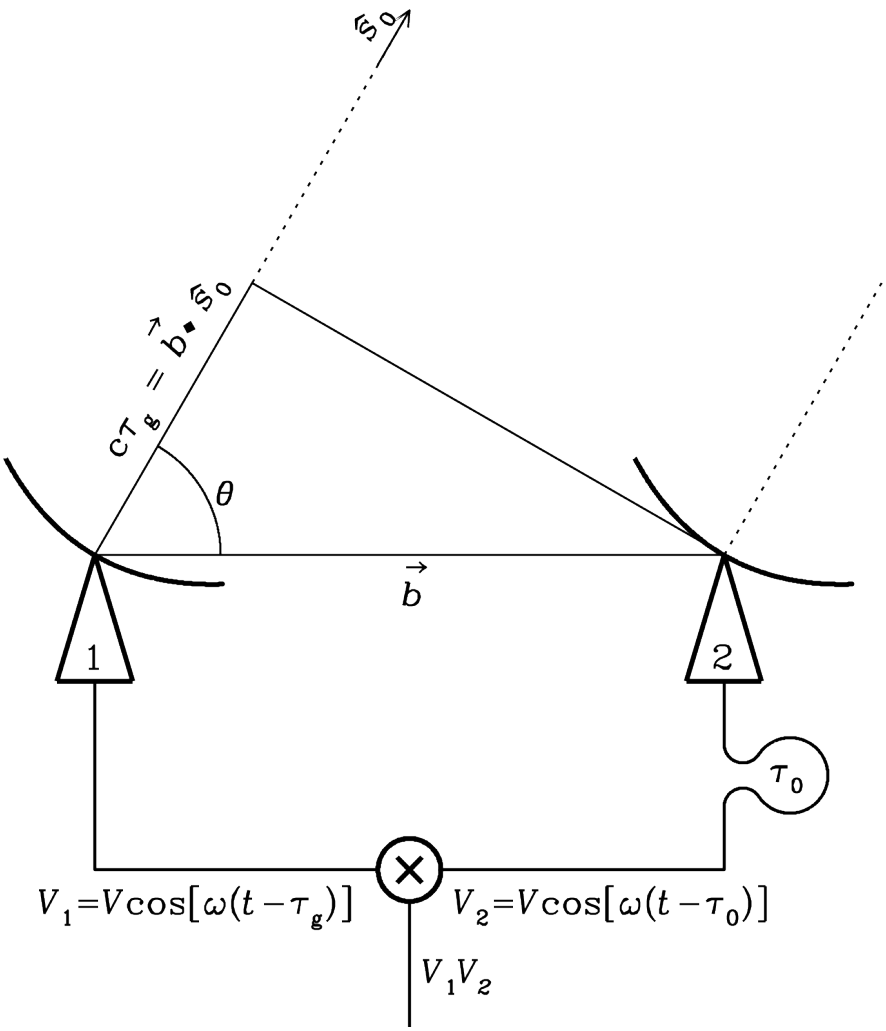

Figure 3.13: The same interferometer from Figure 3.11. Here a time delay of τ_0 is introduced to the signal of antenna 2 by increasing the length of cable. Figure from Condon & Ransom (2016).

3.9 is more accurately written as

$$I_\nu = I_\nu^D * B + \epsilon. \tag{3.12}$$

It is for this reason that the real image cannot be obtained by simply applying the convolution theorem. The most common method of solving this deconvolution problem is known as the CLEAN algorithm first introduced by Högbom (1974). By assuming that true image to be made of a collection of point sources a simple iterative process over the dirty image can recreate the true image. The algorithm is outlined below:

1. The location and value of the brightest peak in the dirty image is found.

2. The PSF is multiplied by the intensity of this peak and what is known as the

gain factor $0 < \gamma < 1$ and subtracted from the dirty image at the position of the peak.

3. The position and magnitude of the subtracted point source is recorded in a model.

4. Go to (1) unless the peak is below some predefined flux value OR a user defined number of iterations has been reached. The remaining image is now called the residual image or, simply, the residuals.

5. Convolve the accumulated model points with an idealised PSF called the CLEAN beam. This is usually a Gaussian fitted to the main lobe of the original PSF.

6. Add the residuals to the image from (5) to form the final CLEAN image.

You may have noticed that this is performed entirely in the image domain. This has some significant disadvantages, specifically because the PSF must be offset before subtraction, which limits how much of the image that can be deconvolved. An implementation of CLEAN in the visibility domain was developed by Clark (1980) and operates in two cycles, a major and minor cycle. The major cycle starts as above by finding the position of the brightest peak. The minor cycle is then run by implementing a partial Högbom clean with the threshold set based on the first sidelobe of the PSF. The output model from the minor cycle and the PSF are both Fourier transformed and multiplied. This product is then inverse Fourier transformed and subtracted from the dirty image and the major cycle begins again. This method relies heavily on the FFT algorithm which requires the visibilities to be on a regular grid. The effect of gridding can lead to aliasing errors in the deconvolved image.

The final implementation of the CLEAN algorithm that I will discuss, and the one that is in prevalent use in modern radio imaging software, is the Cotton-Schwab implementation from Schwab (1984). It follows the same major cycle-minor cycle format as the Clark clean, however the ungridded visibilities are computed for the sky model. This is done in two methods, for observations with only a few sources in the sky model, the direct Fourier transform is taken. In the more likely case of a large number

of sources in the sky model, the visibilities are de-gridded after they have undergone an FFT. These model visibilities are then subtracted from the observed visibilities to produce residual visibilities. These are then imaged and the next iteration occurs.

3.3.3 Calibration of Interferometric Visibilities.

Interferometric visibilities require calibration in order to account for the effects of the ionosphere. For LOFAR data this is performed using the Default Pre-Processing Pipeline (DPPP; van Diepen et al., 2018). An observation is made of a known calibrator source for which there is a set of model visibilities. The DPPP calibration algorithm aims to minimise the following equation

$$||\mathbf{V}_{pq} - \mathbf{G}_p \mathbf{M}_{pq} \mathbf{G}_q^{\dagger}|| \tag{3.13}$$

for each baseline pq. Here $\mathbf{V}$ are the measured visibilities, $\mathbf{M}$ are the modelled visibilities and $\mathbf{G}$ are known as the gain matrices for each antenna p, q and the superscript $\dagger$ indicates the Hermitian conjugate. Calibration is done under the assumption of time invariability of the calibrator source. Unfortunately, if the Sun is close enough to the calibrator so that it can be seen in the sidelobes, during bursty periods such as solar radio noise storms this assumption breaks down. Calibration solutions found during these periods are inaccurate at best. The image in Figure 3.14 was made with a bad calibration solution and as such, multiple sources can be seen.

Calibration is arguably the most important step in the data processing of interferometric observations. To date, direction-dependent calibration on LOFAR solar observations is not a common step taken, despite its proven success in astrophysical observations (de Gasperin et al., 2019). A method to correct for radio bursts in calibration solutions and combine this with direction-dependent calibration should be developed and self-calibration techniques developed for solar imaging with the Murchison Widefield Array (MWA; Mondal et al., 2019) should be implemented before the parameter space for imaging algorithms can be fully explored.

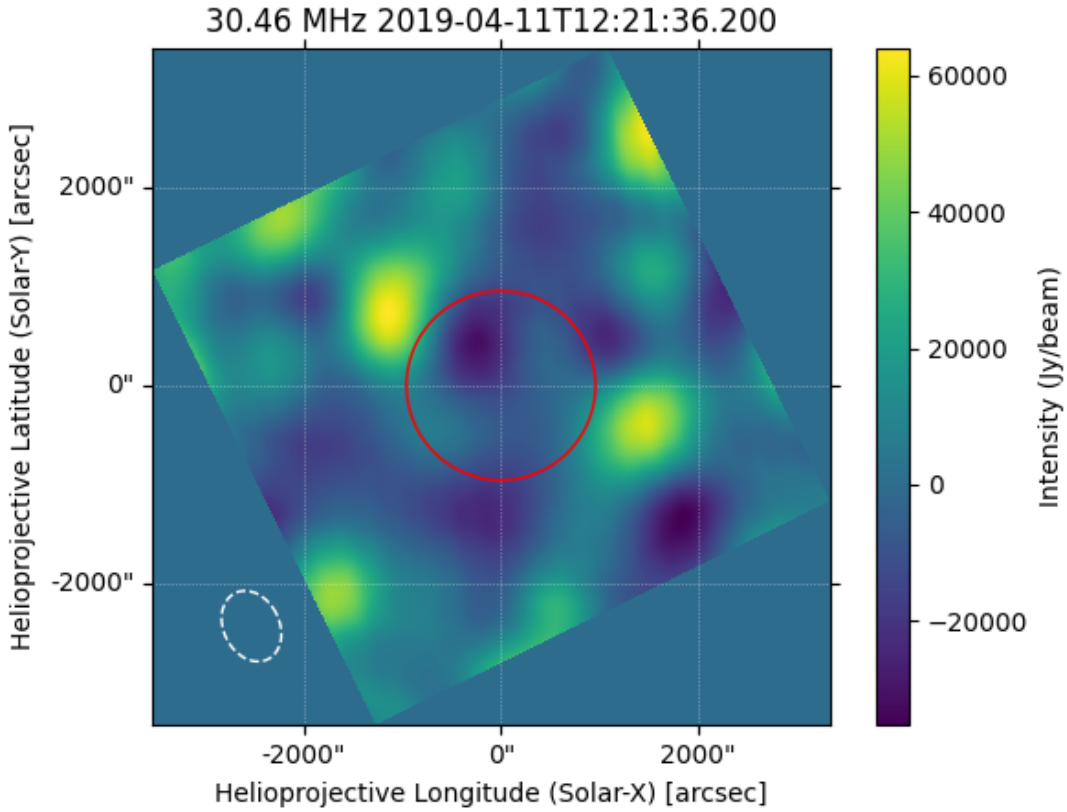

Figure 3.14: A solar radio burst imaged with poor calibration. The colourbar shows intensity in units of Jy/beam. The red circle indicates the solar limb while the dashed white ellipse is the CLEAN beam. Multiple bright peaks and negative bowls are typical artefacts of failed calibration.

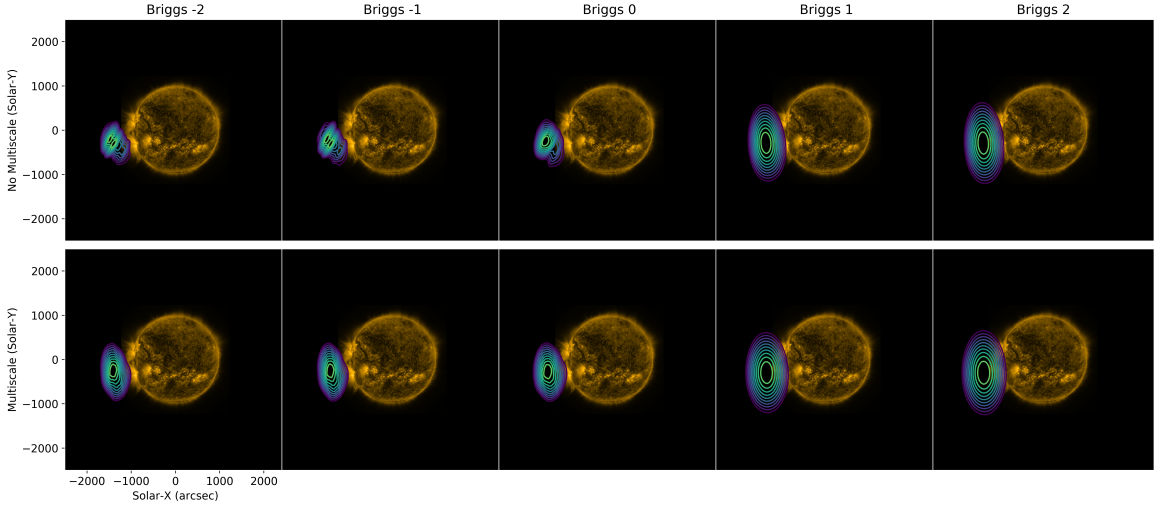

Figure 3.15: A solar radio burst imaged multiple times changing the Briggs robustness parameter with (bottom) and without (top) multiscale cleaning. From left to right the Briggs robustness parameter is chosen as -2, -1, 0, 1 and 2. The effect of this change on the source is most evident when multiscale cleaning is not used. What appears to be a two peak structure with Briggs -2 is completely obfuscated when using Briggs 2. Even when using multiscale cleaning, it is evident that the source size changes considerably with increasing Briggs robustness.

Imaging algorithms such as CLEAN have proven themselves to be widely successful in the field of radio astronomy. However, the ability to produce different results with the same data by only changing the parameters of the algorithm is too subjective when the main focus of one's research is to determine the size of a radio burst. A number of parameters are necessary to run the CLEAN algorithm, with number of iterations and weighting scheme having the most notable effect on the output image. Figure 3.15 shows how changing the Briggs robustness parameter for weighting the visibilites (Briggs, 1995) affects the resulting image. The top panel shows the results for the CLEAN algorithm implemented in WSCLEAN and the bottom panel shows the results when using multiscale cleaning (Offringa & Smirnov, 2017).

In order to consistently image the Sun it is important to determine an appropriate calibration procedure as well as standardise which parameters are to be used in imaging algorithms. Currently, there is little in the way of consensus as to how interferometric solar imaging should be done. Maguire et al. (2021) and Ryan et al. (2021) show interferometric imaging of a radio burst and the quiet radio Sun respectively using LOFAR. Their methodology is broadly similar though was only finalised after multiple trial and error attempts. Unlike wide-field imaging of other astrophysical sources which

can build upon years of research using aperture synthesis techniques, the Sun is a time-dependent source and does not enjoy the legacy software that has been developed for other radio astronomy applications. In order to extract the most scientific value from current observations, the parameter space for the CLEAN algorithm needs to be explored to avoid making images to a subjective standard. A good start to this work would be to compare how well the algorithm can recreate a known model within the parameter space. The use of supercomputing facilities will be crucial for this to take any reasonable amount of time.

Despite its algorithmic origins, radio imaging can be a very subjective endeavour. Not only can things like the number of iterations or gain parameter be changed to give different results, each baseline can be weighted based on their distance from the centre of the *uv* plane, how many are in a given region, and everything in between (Briggs, 1995). As such, when trying to quantify the size of radio bursts with interferometric observations it can be undesirable to rely images that *look* correct. In Chapter 5 I outline a technique, never before used in the context of solar radio imaging, to directly fit the visibilities and thus avoid any undesired effects from the various tweaks that can be made with imaging algorithms.

4

The REALtime Transient Acquisition Backend (REALTA)

Modern radio interferometers such as the LOFAR are capable of producing data at hundreds of gigabits to terabits per second. This high data rate makes the analysis of radio data cumbersome and computationally expensive. While high performance computing facilities exist for large national and international facilities, that may not be the case for instruments operated by a single institution or a small consortium. Data rates for next generation radio telescopes are set to eclipse those currently in operation, hence local processing of data will become all the more important. Here, I introduce the REAL-time Transient Acquisition backend (REALTA), a computing backend at the Irish LOFAR station (I-LOFAR) which facilitates the recording of data in near real-time and post-processing. I also present first searches and scientific results of a number of radio phenomena observed by I-LOFAR and REALTA, including pulsars, fast radio bursts (FRBs), rotating radio transients (RRATs), the search for extraterrestrial intelligence (SETI), Jupiter, and the Sun. This work was published as Murphy et al. (2021) in *Astronomy and Astrophysics*.

4.1 Introduction

Modern radio interferometers produce more data than any astronomical instrument in history. Interferometric observations can receive data at hundreds of gigabits per second, requiring high performance computer (HPC) facilities to preprocess data before it can be analysed and scientifically explored. These data rates far exceed those of modern generation solar optical telescopes such as the Daniel K. Inouye Solar Telescope (DKIST) which has a data rate of only 4 GB/s. With newly built telescopes such as the Murchison Widefield Array (MWA; Lonsdale et al., 2009), MeerKAT (Jonas, 2018) and the Australian Square Kilometre Array Pathfinder (ASKAP; Johnston et al., 2008)

acquiring such vast amounts of data (up to 300 Gbps; Voronkov, 2020; Lonsdale et al., 2009) radio astronomy is working at the cutting edges of big data science. The Square Kilometre Array (McMullin et al., 2020) is commencing construction this year and pushes the computational requirements to ever more difficult regimes (Scaife, 2020).

The detailed differences between the station types are described in van Haarlem et al. (2013), one key difference being that international stations have twice the collecting area of a Dutch core or remote station. LOFAR operates in two modes: international mode, also known as International LOFAR Telescope (ILT) mode, and local, or stand-alone, mode. In ILT mode, data from all the LOFAR stations in the network are sent via fibre optics to the COBALT2.0 correlator (an upgrade to COBALT1.0, Broekema et al., 2018) in Groningen, in the Netherlands. In local mode, each international station is operated by the host institute or consortium. *De novo*, international stations do not have dedicated processing backends. Without such an addition the raw data from an international station could not be recorded or analysed.

The REAL-time Transient Acquisition backend (REALTA; from the Irish word for star, *réalta*) is a seven node computer cluster designed to record and analyse the raw BF data from international LOFAR stations in real-time, implemented at I-LOFAR. It takes inspiration from the ARTEMIS backend at the LOFAR-UK station in Chilbolton (Serylak et al., 2012; Karastergiou et al., 2015), although it significantly improves upon its hardware composition, using modern components with greater computational power. The REALTA hardware is available commercially, and as such REALTA can be implemented at any international LOFAR station and is ideal as a generic computing backend for LOFAR local mode observations.

Telescope backends at other international LOFAR stations have been used to search for fast radio bursts (FRBs) and studying pulsars using LOFAR-UK (for example, Karastergiou et al., 2015), the French LOFAR station at Nançay (for example, Rajwade et al., 2016; Bondonneau et al., 2017), and its extension, NenuFAR (for example, Bondonneau et al., 2021), the German stations (e.g Donner et al., 2019; Porayko et al., 2019; Tiburzi et al., 2019), and the combination of a number of international stations

(for example, Mereghetti et al., 2016; Hermsen et al., 2018; Michilli et al., 2018). Here I showcase similar success in these and various other observations using I-LOFAR and REALTA.

Development of REALTA began shortly after the construction of I-LOFAR was completed. I have been involved in this process from the start, attending meetings detailing the necessary hardware specifications and networking setup. Not only did I physically install REALTA, I have been on site at I-LOFAR for both regular and emergency maintenance trips. I developed prototype software for plotting the raw data captured by REALTA and wrote scripts to specifically plot solar data recorded in mode 357. Throughout this time, I was under the expert guidance of Mr. Joe McCauley and Dr. Brian Coghlan.

The hardware for REALTA is further described in section 4.2 along with the networking configuration for the I-LOFAR control room while section 4.3 describes the data capture and processing software used by REALTA. In section 4.4, some first scientific results from REALTA are highlighted. These include observations of pulsars, solar radio bursts, FRBs, Jovian radio emission, and the search for extraterrestrial intelligence (SETI).

4.2 REALTA

In this section, I describe the local network configuration necessary to capture raw User Datagram Protocol (UDP; Postel, 1980) packets from I-LOFAR and the individual hardware components that make up REALTA. Data is transferred from the station through the UDP protocol using LOFAR CEntral Processing (CEP) packets. Each packet is 7824 bytes long and consits of a 16 bit header followed by 16 time slices for each beamlet. The full specification for CEP packets is described in both Lubberhuizen & Kooistra (2009) and Virtanen (2018). CEP packets are sent via fibre optics to CEP or REALTA over four data 'lanes'. Each lane only holds one quarter of the maximum number of beamlets for an observation. The network to facilitate capturing these

packets is shown as a schematic block diagram in Figure 4.1, while Table 4.1 gives a detailed description of the specifications for each of the REALTA nodes.

4.2.1 Local networking

The control room for I-LOFAR is located at the Rosse Observatory on the grounds of Birr Castle and $\sim$ 100 m from I-LOFAR (Figure 3.9). In order to record data from I-LOFAR while it is in local mode, a high-speed 10 Gbps network was set up between the ILT container that houses the I-LOFAR Remote Station Processing (RSP) boards and the control room.

In a typical ILT observation, data output from each RSP board is sent to a Foundry LS648 10 Gbps network access switch (S2) in the container. From here it is sent to a Foundry LS624 switch (S1) before finally being sent over a 10 Gbps fibre connection to the COBALT cluster in Groningen for correlation and or beamforming with data from other LOFAR stations.

The aim of I-LOFAR's network configuration is to record RSP data to REALTA in the I-LOFAR control room. This is achieved by a fibre link between the I-LOFAR control room and S1. RSP data are sent along a Virtual Local Area Network (VLAN), VLAN 2278, on a 10 Gbps fibre link to the control room. Data reaches a fibre optic termination panel in the I-LOFAR control room and is sent to a 10 Gbps Dell EMC S4128F-ON optical switch. A fibre link between this switch and the REALTA compute nodes allows data to be recorded. All REALTA compute nodes are connected via Infiniband (an alternative to Ethernet and fibre). On REALTA this acts at a maximum of 10 Gbps to allow for transfer of data between nodes and Network File System (NFS) mounting.

As well as this, a future link to a HEAnet (Ireland's national education and research network) cloud service for data transfer to the research institutions of the I-LOFAR consortium has been approved by ASTRON. This will allow access along existing 10 Gbps fibre infrastructure to S1 and then over another fibre to the control room along a VLAN. Another fibre is in place to eventually send RSP and Transient Buffer Board

(TBB) data directly from S2 to the control room using two additional VLANs. Data transfer from REALTA to research institutes is currently facilitated by a direct 1 Gbps link between the Dublin Institute of Advanced Studies (DIAS) and S1 via HEAnet on a VLAN.

4.2.2 Hardware description

REALTA is ultimately designed to perform real-time analysis of radio data generated by the I-LOFAR international station. In its current form, it uses four Dell Poweredge R740XD compute nodes named UCC1, UCC2, UCC3, and UCC4. Each compute node contains two Intel Xeon® Gold 6130 central processing units (CPUs) and an NVIDIA Tesla V100 16GB graphics processing unit (GPU). Each CPU has 16 cores, with two threads per core giving a total of 64 threads per node. A total of 210 TB of storage is distributed across the compute nodes with a further 128 TB available on a dedicated storage server, NUIG1. Storage on REALTA is set up as a Redundant Array of Inexpensive Disks (RAID). Most disks ($\sim$ 263 TB) are in RAID 5 for data archival, while a number of scratch disks ($\sim$ 75 TB) are set up in RAID 0 for recording and processing raw data. In addition to this, a compute node for dedicated SETI research was provided by the Breakthrough Prize Foundation in collaboration with the Breakthrough Listen (BL) team at the Berkeley SETI Research Centre. The BL compute node is a SuperMicro 6049P-E1CR24H node with two, 16 core (8 threads) Intel Xeon® Silver 4110 CPUs, an NVIDIA RTX 2080Ti GPU, and 144 TB of storage. The BL Headnode is a SuperMicro 1029U-TRTP2 node intended to control REALTA during SETI observations. When being operated from the BL Headnode, all of the REALTA compute nodes will receive an identical operating system (OS) image and process in parallel across all five compute nodes. Each of the REALTA nodes connect to the 10 Gbps Dell EMC S4128F-ON optical switch via fibre optic cable as well as a 1 Gbps Ethernet switch for normal networking (using default VLAN 1). There are two redundant keyboard-video-mouse (KVM) servers and a KVM switch for remote access to both switches and all machines, and three uninterruptible power supplies (UPS)

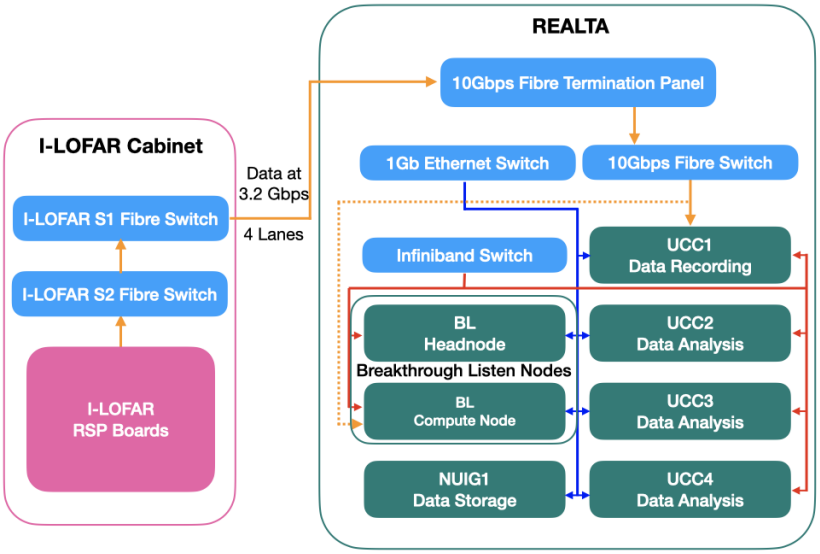

Figure 4.1: Block diagram for REALTA and I-LOFAR. Data recorded at the Remote Station Processing (RSP) boards are sent to the S1 fibre switch in the I-LOFAR container. Here the data are split into four 'lanes' where each lane contains the data from a maximum of one quarter of the beamlets from the observation. The four lanes of data are then sent over a fibre connection to the I-LOFAR control room where it is recorded by REALTA. Orange arrows indicate the data path along fibre connections. Blue arrows are 1 Gbps Ethernet links and red arrows show infiniband connectivity. The dotted orange line is a fibre link to the BL compute node currently under development.

to mitigate the effects of a sudden power outage on both servers and critical access paths. Fail-safe cold-aisle air-conditioning will handle heat created by this unsupervised cluster.

REALTA is located in the control room which is $\sim$ 100 m from the I-LOFAR HBAs and $\sim$ 150 m from the LBAs. As REALTA was being set up and tested, the RFI from the system was monitored using all-sky observations and sub-band statistics observations. It was found that REALTA did not produce any significant RFI.

Table 4.1 lists the technical specifications for each of the nodes in REALTA. In its configuration at the time of writing, REALTA acts as a number of independent nodes (UCC1-4, NUIG1, BL headnode, and BL Compute node). Data is recorded solely to the UCC1 compute node while the remaining nodes perform pre-processing and data analysis after data has finished recording.

	Storage Node (NUIG1)	Compute Nodes (×4 UCC1-4)
Machine Model	Dell Poweredge R730XD	Dell Poweredge R740XD
CPU Model	Intel Xeon® E5-2640 V4 (×2)	Intel Xeon® Gold 6130 (×2)
CPU Clock Speed	2.40GHz	2.10GHz
CPU Cores (Threads)	20 (40)	32 (64)
RAM	256GB	256GB
Storage	128TB	210TB (total)
GPU	N/A	16GB NVIDIA Tesla V100
	BL Headnode	BL Compute Node
Machine Model	SuperMicro 1029U-TRTP2	SuperMicro 6049P-E1CR24H
CPU Model	Intel Xeon® Silver 4110 (×2)	Intel Xeon® Silver 4110 (×2)
CPU Clock Speed	2.10GHz	2.10GHz
CPU Cores (Threads)	16 (32)	16 (32)
RAM	93GB	96GB
Storage	N/A	144TB
GPU	N/A	11GB NVIDIA RTX 2080Ti

Table 4.1: Table of hardware specifications for REALTA. Note that the specifications are given for individual UCC 1-4 compute nodes, except for storage which is the total amount dedicated to archival of data distributed across all four.

4.3 Software and pipelines

In REALTA's current state, UDP packets are recorded directly to disk before being converted into usable science products, such as Stokes parameters with variable levels of time integration, after the observation has completed. Future work will implement the current software pipelines to work directly on incoming data, which will allow for real-time analysis of the low frequency sky. Currently, a combination of local and community developed software is used in the main data recording and reduction pipeline. The primary recording and processing of the pipeline are described below.

4.3.1 Recording data

The station RSPs generate a stream of packets across four data lanes, which is recorded on our compute nodes using software developed by Olaf Wucknitz at the Max Planck Institute for Radio Astronomy. The recording software, `dump_udp_ow`, listens to each port for incoming CEP packets, discards the UDP metadata related to the protocol, and writes the remainder of the packets to disk.

In order to reduce the storage requirements to record the CEP packets, the software can compress the data while it is being captured. This is accomplished by applying the `zstandard` compression algorithm[1] to the output data stream. This procedure requires additional CPU processing but offers a compression fraction in the range of 40-60%, depending on the observing mode and noise of an observation.

4.3.2 Pre-processing data

Once the data has been recorded to disk, observers use `udpPacketManager`[2] (McKenna, 2020), a C library developed to convert the raw CEP packets, either compressed or uncompressed, to usable scientific data products. It implements checks to correct for issues that may have occurred during the recording process, such as padding when

[1] https://github.com/facebook/zstd
[2] https://github.com/David-McKenna/udpPacketManager

packets are missed, performs a polarmetric correction on the voltages using `dreamBeam`[1] in order to correct for the changes of intensity with respect to altitude of the source, and generates scientific data products for further processing and analysis.

The `udpPacketManager` library is extremely versatile and allows for an observer to chose a number of processing strategies. These include individual polarisation analysis, forming Stokes parameters, ordering data by either time or frequency or formatting data to be used with other software for further analysis. The most common processing strategy is to construct Stokes I and V from the voltages, then output the results to disk in a binary file format that follows the `SIGPROC` Filterbank standard (Lorimer, 2011). Future work will include determining best practises for removal of RFI from filterbank formatted files.

4.3.3 Pulsar and single pulse processing

All pulse-like observations undergo an additional processing step, whereby data are both channelised by a factor of eight (reducing the bandwidth of a given observing subband to 24.41 kHz) and coherent dedispersion is applied to the voltages. Coherent dedispersion is the process by which an input signal is convolved with the inverse transfer function of the inter-stellar medium in order to remove the signature of dispersion delay due to free elections along the line of sight (Hankins & Rajkowski, 1987). This process is especially important at frequencies observed by LOFAR as these delays scale with the inverse square of the observing frequency. This process is performed on the GPUs in REALTA using a modified version of `CDMT` (Bassa et al., 2017), which accepts input voltages from `udpPacketManager` rather than h5 files generated from the LOFAR COBALT system. In order to avoid distortions caused by Fast Fourier Transform (FFT) operations on zero-padded data, `CDMT` was further modified to overlap the input voltages between processing iterations.

Pulsar data is further reduced using a combination of `digifil` and `DSPSR` (van Straten & Bailes, 2011) to generate folded profiles which are then analysed using

[1] https://github.com/2baOrNot2ba/dreamBeam/

`PSRCHIVE` (Hotan et al., 2004). The filterbanks are also often folded using `PRESTO` (Ransom, 2001), a suite of pulsar searching software, to determine optimal dispersion measures for folding observations. RFI flagging is performed in two steps: firstly, all data below 106 MHz and above 194 MHz is automatically flagged to remove contributions from local FM radio transmission and to minimise noise contributions due to the loss in sensitivity near the edge of the telescope's polyphase filter. Secondly, the spectral kurtosis method (e.g. Nita & Gary, 2010) is performed to remove transient RFI sources.

Single-pulse sources, such as intermittent rotating radio transients (RRATs; McLaughlin et al., 2006) and fast radio bursts (FRBs; Lorimer et al., 2007; Thornton et al., 2013) are searched for using `Heimdall`[1] to generate pulse candidates across a wide dispersion measure range. A typical search is performed between 5 pc cm^{-3} and 500 pc cm^{-3} across all pulsar and single-source observations. These are then filtered, discarding any below the 7.5 σ level to reduce the number of spurious candidates due to system noise or alignment of RFI between frequency channels. The remaining candidates are then plotted and visually inspected to discard those that are due to RFI, ionospheric scintillation or other phenomena that may cause spurious signals.

4.3.4 SETI data processing

For SETI, the goal is to achieve a very high spectral resolution of the order of a few hertz to look for narrow-band Doppler drifting signals. Such signals are prime candidates for deliberately transmitted beacons by Extra-Terrestrial Intelligence (ETI; Tarter, 2001). Baseband voltages are recorded directly on the BL compute node as described in Section 4.3.1. The `udpPacketManager` library is then used to convert these data to Green Bank Ultimate Pulsar Processing Instrument[2] (GUPPI) formatted baseband data products for further processing. The BL team has developed a suite of software to work with the GUPPI formatted baseband voltages (Lebofsky et al., 2019) and the

[1] https://sourceforge.net/projects/heimdall-astro/
[2] https://safe.nrao.edu/wiki/bin/view/CICADA/GUPPiUsersGuide

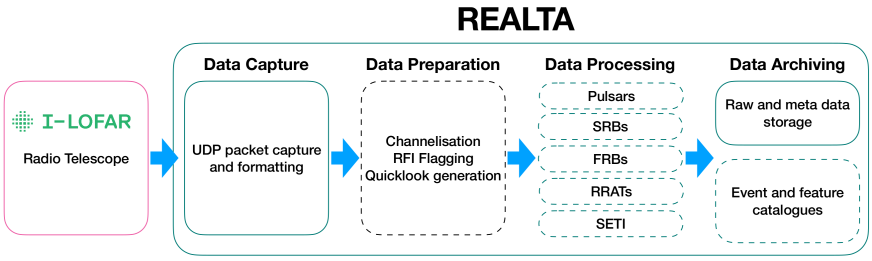

Figure 4.2: System diagram for REALTA, including future data preparation, processing, and archiving capabilities. Solid lines indicate existing features, while dashed lines denote stages under development. REALTA is currently capable of capturing data from the I-LOFAR radio telescope and archiving it in near real-time. The I-LOFAR team are in the process of developing a variety of data processing pipelines that will flag RFI, identify and characterise SRBs, pulsars, RRATs, FRBs, and SETI signals. Machine learning methods are being explored for a number of these tasks.

preliminary result from this software is discussed in section 4.4.

4.3.5 Future development and real-time analysis

The current and planned data path through REALTA, from the time it is recorded at I-LOFAR to when it is written to disk by REALTA is shown as a block diagram in Figure 4.2. UDP packets containing the data are captured and recorded directly to disk in real-time (section 4.3.1). The data are then formatted and metadata updated (§4.3.2) so that they are compatible with existing pulsar and SETI software (section 4.3.3, 4.3.4).

In the future, the capture and formatting of data will occur simultaneously in real-time. Further channelisation of the raw data in the data capture stage will be implemented in order to increase the spectral resolution of observations and help in flagging Radio Frequency Interference (RFI) in the data. This, along with the generation of quick-look plots, will form the data preparation stage. The data processing software described below will also be developed to allow for real-time processing of solar, pulsar, FRB, RRAT, SETI, and other data. Finally, the data archive will be expanded to include a catalogue of transient events observed and a summary of their features.

4.4 First results

Since REALTA's installation in July 2018, more than 130 unique targets have been observed. These science use cases range from the Sun, to planetary bodies, to pulsars. This allows for I-LOFAR to be used in the pursuit of a number of science goals. These include: analysing the wide gamut of low-frequency transient phase space (Keane, 2018), characterising pulsars and the characteristics of binary systems (Manchester, 2017), and observing solar activity and space weather (Maguire et al., 2020). REALTA has also enabled collaborations with other LOFAR station operators, most notably an ongoing very long baseline interferometry (VLBI) campaign performed with stations located in Germany, France, and Sweden (in a continuation of Wucknitz, 2019) in order to study scattering of light from pulsars in the interstellar medium.

The REALTA use cases are complementary to the Key Science Projects of the ILT (KSP; see van Haarlem et al., 2013). For example, a single international station is well suited to the study of bright transient sources such as pulsars, rotating radio transients, fast radio bursts, solar radio bursts, Jovian radio emission, and SETI signals, where flexible scheduling can be an advantage (for example, Maguire et al., 2020; Morosan et al., 2019). The flexible scheduling of international stations in local mode allows for projects that require a large amount of observing time or regular observations of the same object. International station teams can also use the station to develop and test novel observing campaigns and hardware and software systems (for example, Scully et al., 2021). First results from the aforementioned science use cases are described below. In the following subsections I refer to work undertaken as part of the I-LOFAR chief observing team.

4.4.1 Solar radio bursts

Solar radio bursts (SRBs) are some of the brightest phenomena in the radio sky. Five types of SRBs were classified in the 1950s (Wild & McCready, 1950; Boischot, 1957; Wild et al., 1959) and have been studied regularly since (See Pick & Vilmer, 2008, for

a comprehensive review). A number of observations of solar radio bursts have been taken either using the LOFAR array as part of the Solar and Space Weather KSP (for example, Zhang et al., 2020; Murphy et al., 2021) or with an international station during local mode (for example, Morosan et al., 2019; Maguire et al., 2020; Bartosz et al., 2020). Most solar radio bursts occur due to the plasma emission process, first described by Ginzburg & Zhelezniakov (1958), and as such can be used as a diagnostic for the plasma density in the solar corona (Melrose, 1987). Remote sensing of radio emission from the Sun can be used as diagnostics of both large scale energy release from solar flares and CMEs (Carley et al., 2021) and small-scale energy release, potentially related to coronal heating (Mondal et al., 2020).

On 2 November 2020, I-LOFAR observed a solar radio noise storm in mode 357. The dynamic spectrum of this storm from 12:00 - 14:00 UTC is shown in Figure 4.3a at 10 ms temporal resolution and 195.3125 kHz spectral resolution. A large number of short duration SRBs are seen across the full HBA band.

Some SRBs can exhibit fine scale temporal and spectral features. Fine scale temporal and spectral structure are thought to be indicative of the turbulent nature of the solar corona which could further enhance the diagnostic capability of SRBs (Kolotkov et al., 2018; Sharykin et al., 2018; Reid & Kontar, 2021). These include, for example, herringbone bursts which are observed as part of type II bursts (for example, Carley et al., 2015) or individual striations of a type IIIb burst (for example, Zhang et al., 2020). A number of short duration radio bursts, which are not part of the five classified types, have also been reported (for example, Ellis & McCulloch, 1967; Ellis, 1969; Melnik et al., 2010a). The high temporal resolution of REALTA observations with I-LOFAR will allow the study of these bursts at some of the highest temporal resolutions to date. Figure 4.3b shows a zoom-in of the radio noise storm from Figure 4.3a at 10 ms temporal resolution. The inset of Figure 4.3b shows the sub-second variation of a particular burst with a temporal resolution of 1 ms.

Figure 4.4 shows a number of type III and type IIIb bursts observed on 3 June 2020. It is possible that these bursts form type IIIb - III pairs, where the fundamental

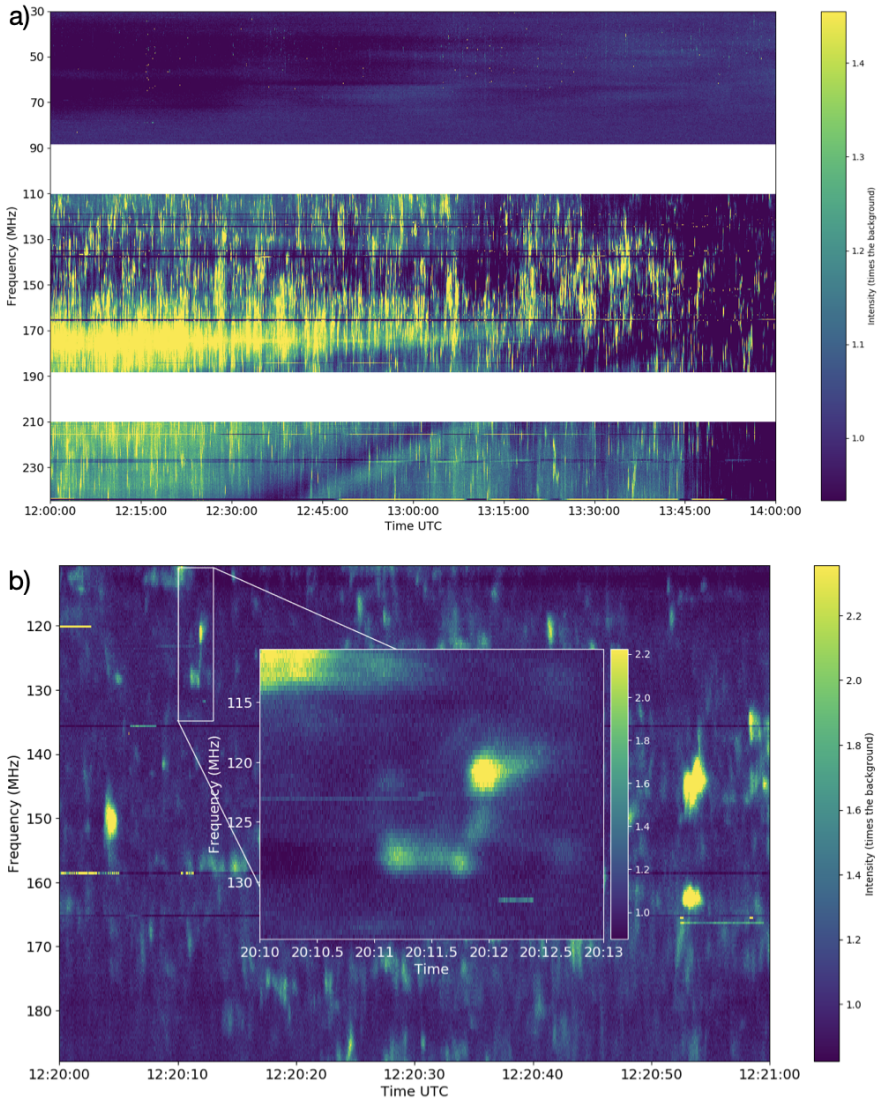

Figure 4.3: A dynamic spectrum of a solar radio noise storm observed on 2 November 2020. The x axis shows the time of day on 2 November 2020 while the y axis shows the frequency in MHz. The colourbars shows the intensity relative to the background. This is a period of radio activity where bursty features that do not match the 5 typical types of bursts described in section 1.4 can be seen. a) In this mode 357 observation, a number of bright bursts can be seen at frequencies greater than 110 MHz (yellow in the dynamic spectrum). The white gaps indicate the frequency range not observed in mode 357.Here the data spans 2 hours from 12:00 UTC and has a temporal resolution of 10 ms. b) Zoom-in of panel a at 1 ms temporal resolution. A number of short duration SRBs are observed. The inset shows the sub-second variation of an individual burst in the noise storm, also at a temporal resolution of 1 ms. Bursts such as this have not been characterised. The spectral resolution of both panels is 195.3125 kHz.

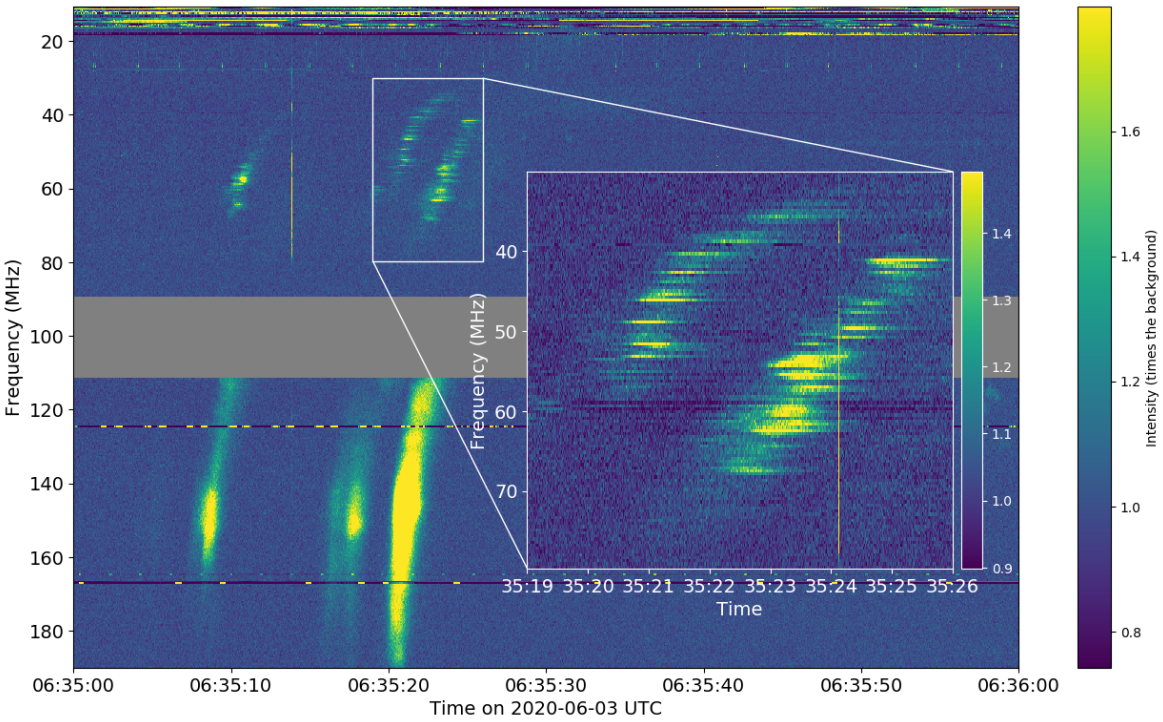

Figure 4.4: Type IIIb burst observed on 3 June 2020. In this mode 357 observation, a number of type III bursts can be seen in the frequency range of 10-190 MHz (yellow in the dynamic spectrum). The intensity relative to the background is shown in the colourbar. Here the data spans 1 minute from 06:35 UTC and has a temporal resolution of 1 ms. The inset shows 2 type IIIb bursts which occur over 7 seconds in the frequency range 30 - 80 MHz. The fine spectral structure known as striae (see Section 1.4.1) are clearly evident. The spectral resolution of the dynamic spectrum is 195.3125 kHz. It is interesting to note that the bright burst that occurred at $\sim$ 06:35:20 in the frequency range 110-190 MHz disappears at lower frequencies. It is possible that this burst is a J burst such as those described in Section 1.4.1, where the turnover of the burst occurs in the frequency range not observed.

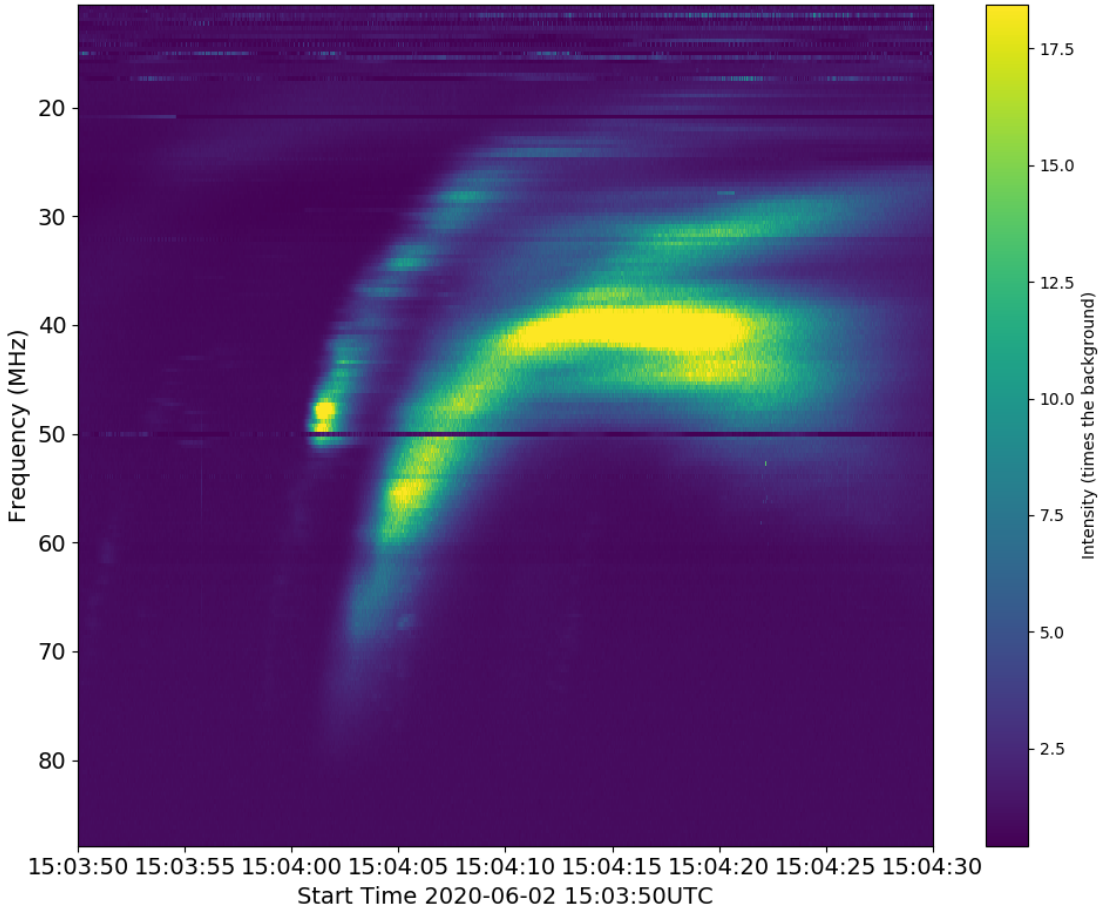

Figure 4.5: Two solar radio bursts observed on 2 June 2020. The earlier burst is likely a type III SRB while the later burst shows the morphology typical of a U burst. The observation has a spectral resolution of $\sim$ 195 kHz and a temporal resolution of 1 ms. The intensity of the bursts relative to the background is given by the colourbar.

emission is seen as a type IIIb while the harmonic emission is seen as a type III. Zhang et al. (2020) performed an analysis on interferometric images of a type III-IIIb pair and found the source motion of the pair components to be significantly different.

Figure 4.5 shows an LBA observation from 2 June 2020 of a type III burst and a U burst, both described in Section 1.4.1 as being generated by electron beams travelling along open and closed magnetic field lines respectively. This observation also has a 1 ms temporal resolution. Although a single international LOFAR station can only make spectroscopic observations of type III bursts and their sub-types, this is still a valuable tool in determining the characteristics of the accelerated electron beam that instigates plasma emission in these bursts (Reid & Kontar, 2018). Furthermore, short duration pulsations in radio bursts can give insight into magnetohydrodynamic oscillations in

the solar corona (Carley et al., 2019).

With future upgrades to ILT hardware coming in the first half of the 2020s (mainly LOFAR2.0; Edler et al., 2021), international LOFAR stations will require a dedicated high-performance backend to record data rates of ∼6.4 Gbps, should they wish to use the full capacity of the instrument in local mode. While some international stations have existing backends, REALTA offers a powerful backend that is well suited to the data rates of LOFAR2.0. Due to the use of commercially available hardware, straightforward network configuration and freely available software, backends like REALTA will make it possible for international LOFAR stations to capture and process raw data and to undertake a wider variety of astronomical observations. As mentioned in section 4.3.5, in the future it will be possible to process and record raw data in real-time. This will be done by recording data to a ring buffer implemented with the Parkes-Swinburne Recorder Distributed Acquisition and Data Analysis software (PSRDADA; Jameson & van Straten, 2008) and then reading from the ring buffer into `udpPacketManager`. This will further improve the capabilities of international LOFAR stations during local mode. Finally, cooperation and coordinated observations between international LOFAR stations becomes easier if using the same software and hardware for data capture and post-processing and will be more beneficial than each international station operating individually.

5

Measuring Source Sizes in Visibility Space

Low frequency radio wave scattering and refraction can have a dramatic effect on the observed size and position of radio sources in the solar corona. The scattering and refraction is thought to be due to fluctuations of electron density caused by turbulence. Hence, determining the true radio source size can provide information on the turbulence scales in coronal plasma. However, the lack of high spatial resolution radio interferometric observations at low frequencies such as with the LOw Frequency ARray (LOFAR) have made it difficult to determine the true radio source size and level of radio wave scattering. Here we directly fit the visibilities of a LOFAR observation of a type IIIb radio burst with an elliptical Gaussian to determine its source size and position. This circumvents the need for imaging of the source followed by deconvolution, which can introduce spurious effects on source size and shape. For a burst at 34.76 MHz, we find a full width at half maximum (FWHM) along the major and minor axes to be 18.8 arcmin $\pm$ 0.1 arcmin and 10.2 arcmin $\pm$ 0.1 arcmin respectively at a plane-of-sky heliocentric distance of 1.75 $R_{\odot}$. Our results suggest that the level of density fluctuations in the solar corona is the major cause of the scattering of radio waves, resulting in large source sizes. However, the magnitude of ε may be smaller than previously derived in comparison to observations of radio wave scattering in the "tied-array imaging mode" (Morosan et al., 2014), whereby a number of beams are tessellated across the Sun and the response in each beam is interpolated to produce an image (e.g. Reid & Kontar, 2017; Kontar et al., 2017; Zucca et al., 2018; Morosan et al., 2019). This work was published as Murphy et al. (2021) in *Astronomy and Astrophysics*.

5.1 Introduction

Low frequency radio wave propagation in the solar corona is not fully understood. It is widely accepted that scattering of radio waves by density inhomogeneities plays a key

role in the observed source sizes of radio bursts (Fokker, 1965; Steinberg et al., 1971; Stewart, 1972; Riddle, 1974; Thejappa et al., 2007; Thejappa & MacDowall, 2008; Kontar et al., 2019). However, the exact extent to which observed source sizes are broadened is difficult to measure as it requires an angular resolution to spatially resolve the source as well as an *a priori* knowledge of its original size. Current generation radio interferometers such as the LOw Frequency ARray (LOFAR; van Haarlem et al., 2013) have the resolving power to observe this angular size. This angular resolution can be exploited to accurately determine burst size and position, both of which are indicators of the level of radio scattering in the corona, which in turn is related to the level of turbulent density fluctuations. Hence a better understanding of scattering may lead to new insights into the nature of coronal turbulence.

The study of radio wave scattering in the solar corona has its origins in the 60s and 70s. Fokker (1965), Steinberg et al. (1971), Stewart (1972) and Riddle (1974) did seminal work on ray tracing of radio waves in various coronal models. All concluded that sources emitted near the plasma frequency in the solar corona are enlarged due to scattering of radio waves from coronal density fluctuations. While the explanation of coronal scattering for observed source characteristics fell out of favour by the mid-1980s (McLean & Labrum, 1985), it has seen renewed interest in low frequency radio observations in recent years (Thejappa et al., 2007; Thejappa & MacDowall, 2008; Kontar et al., 2017; Sharykin et al., 2018; Gordovskyy et al., 2019; Kontar et al., 2019).

In low frequency imaging, the extent of scattering in the corona can be determined through the analysis of type III radio bursts, particularly their position and size in images or decay times in dynamic spectra (e.g. Kontar et al., 2019; Gordovskyy et al., 2019; Krupar et al., 2018). Given that these bursts are due to plasma emission from electron beams propagating through coronal plasma (see Reid & Ratcliffe, 2014, for a review), they provide a density diagnostic of such plasma. In particular, a subset of these bursts known as "type IIIb" (see Section 1.4.1) provide a diagnostic of scattering in coronal plasma due to density fluctuations from turbulence. For example, type

IIIb bursts often show fine structures or "striae" along the burst envelope (Ellis & McCulloch, 1967; Ellis, 1969; de La Noe & Boischot, 1972; de La Noe, 1975; Melnik et al., 2010b), which are believed to be caused by density inhomogeneities in the corona (Takakura & Yousef, 1975). Using a density model, the frequency bandwidth of these striae can be used to infer the vertical extent of the density inhomogeneity in space. A comparison of this spatial extent to observed source size in images can provide the extent to which the radio emission has been scattered (e.g. Kontar et al., 2017).

Theoretically, the extent of scattering in the corona is related to the root mean squared (rms) fluctuations of electron density $\varepsilon = \sqrt{\langle \delta n^2 \rangle}/n$. Many recent works have assumed a value for ε to use in simulations in order to recreate the time profile and source size of solar radio bursts (e.g. Krupar et al., 2018; Kontar et al., 2019). However, few use the observed source size and time profile to determine ε. Those that have are limited to determining the value of ε in the solar wind at distances $> 10\,R_\odot$. Techniques such as interplanetary scintillations (e.g. Bisoi et al., 2014) and Crab nebula occultation (Sasikumar Raja et al., 2016) have also been used to determine ε at these distances. The general conclusion of these studies is that ε varies slowly with heliocentric distance and has typical values of $0.001 \lesssim \varepsilon \lesssim 0.02$ in the range of 10 to 45 $R_\odot$. Despite this, larger values of ε have been used in models. For example, Reid & Kontar (2010) use a radially varying value of ε to model electron beam transport and found a value of $\varepsilon \approx 0.1$ at 1 AU. Kontar et al. (2019) recently used Monte Carlo simulations of scattering to determine that a value of $\varepsilon = 0.8$ is necessary in order to account for source sizes of the order of 20 arcmin at $\sim$ 32 MHz, as observed by Kontar et al. (2017). This value in particular seems excessively large given the large fluctuations in density this would need. Perhaps during eruptive periods above active regions such as CMEs it may be possible but otherwise seems highly unlikely. Measured values of ε, particularly at heights of $\sim 2\,R_\odot$, are not common in the literature, with the exception of a recent study by Krupar et al. (2020). By using observations from Parker Solar Probe (PSP, Fox et al., 2016), Krupar et al. (2020) calculate a value for $\varepsilon = 0.07$ at a plasma frequency $f_p = 137$ kHz. They also find that the value of ε decreases from 0.22

to 0.09 over a height range of 2.4 to 14 $R_\odot$. Woo et al. (1995) measured the value of ε *in-situ* in the solar wind at distances less than 0.2 AU. They found ε in the range of 0.003 - 0.005 in the fast solar wind and ~ 0.1 in the slow solar wind.

The spectrum of density fluctuations in the solar corona, $S(\mathbf{q})$, can be normalised relative to the rms density fluctuations such that (e.g. Kontar et al., 2019)

$$\varepsilon^2 = \int S(\mathbf{q}) \frac{d^3q}{(2\pi)^3}. \tag{5.1}$$

Thus, understanding the spectrum of density fluctuations is key to understanding their rms value. The shape of $S(\mathbf{q})$ was inferred by Coles & Harmon (1989) from measurements of the solar wind electron density between 2 and 22 $R_\odot$ and is shown in Figure 5.1 (where those authors used $\Phi_{\rm ne}$ for the spectrum of density fluctuations).

Historically $S(\mathbf{q})$ was assumed to be isotropic however, recently it has been shown that this is not the case (Kontar et al., 2019). For an anisotropic spectrum of density fluctuations $S(\mathbf{q})$ can be written as

$$S(\mathbf{q}) = S\left(\left[q_\perp^2 + \alpha^{-1} q_\parallel^2\right]^{1/2}\right), \tag{5.2}$$

where $\alpha = h_\perp / h_\parallel$ is the ratio of perpendicular and parallel correlation lengths. Armstrong et al. (1990) find that the density inhomogeneities are elongated in the radial direction in a ratio of $\sim 3:1$ at 10 $R_\odot$, this would have the effect of a point source being observed as elongated in the perpendicular direction.

It is clear that a correct interpretation of radio observations provide a means to investigate the level of scattering and density fluctuation in the corona. Advances in radio astronomy over the past 40 years have lead to increased sensitivity, temporal resolution, frequency resolution and resolving power. Modern radio telescopes such as LOFAR, the Murchison Widefield Array (MWA; Lonsdale et al., 2009) and the upcoming Square Kilometre Array (SKA; Dewdney et al., 2009) are capable of observing the predicted spatial and time profiles of type IIIb bursts. That said, previous studies with LOFAR have tended to use tied-array imaging in this regard (Kontar et al., 2017),

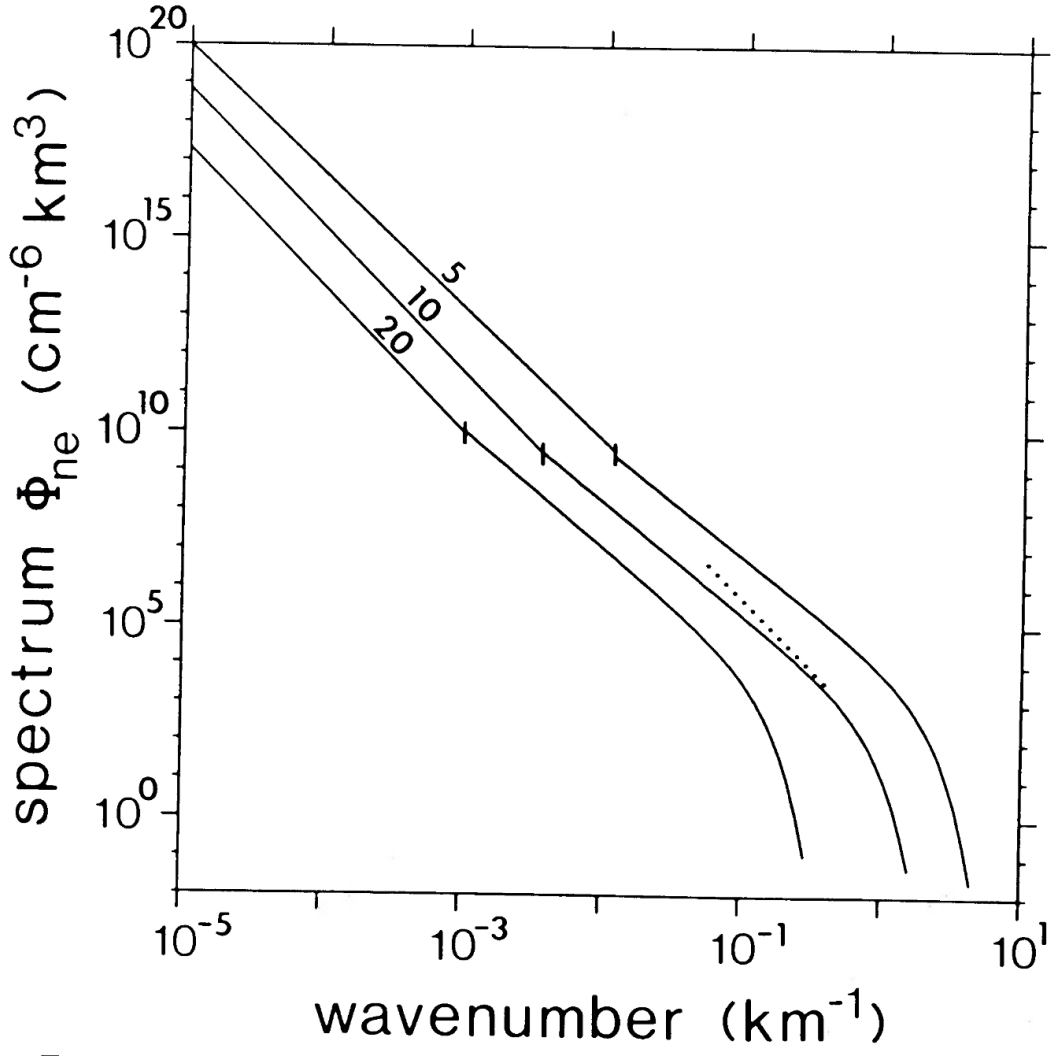

Figure 5.1: Inferred spectrum of density fluctuations from Coles & Harmon (1989). Black curves show the density fluctuation spectra at 5, 10 and 20 $R_\odot$. The vertical ticks indicate the wave number at which there is a break in the power law. The shape of these spectra is best described by a Kolmogorov like power law to some outer scale where a spectral flattening occurs, this shallower power law then continues until an inner scale where a rapid steepening is observed. The dotted line indicates a transient steeping seen in radar data from 1979.

which has limited spatial resolution with respect to interferometric imaging.

Here I use LOFAR interferometric observations to determine the observed radio source size and position and how this differs from the expected source properties, which can be estimated from spectroscopy. Directly fitting interferometric visibilities provides an opportunity to observe low frequency radio sources at a spatial resolution in excess of what has usually been achieved. I compare these results with those of the tied-array observation from Kontar et al. (2017) and discuss the implication this may have on determining the relative level of density fluctuations in the corona. The remainder of this chapter is outlined as follows; an observation of a type IIIb burst is described in Section 5.2, in Section 5.3 I detail a method of directly fitting interferometric visibilities in order to recreate a sky brightness distribution and give results of observed source size. Section 5.3 also includes analysis of a type IIIb striation. I conclude with a discussion about the caution necessary in determining ε from observations in Section 5.4.

5.2 Observation

An interferometric observation of the Sun, utilising 36 LOFAR stations (24 core and 12 remote), was performed on 17 October 2015 from 08:00 UTC to 14:00 UTC. During this time, a type III solar radio burst was recorded at 13:21 UTC. A calibrator source, Virgo A, was observed co-temporally in all subbands over the course of the observation.

Figure 5.2a shows the X-ray flux measured by GOES for the duration of the LOFAR observation. A number of C-class flares can be seen in Figure 5.2a but no significant activity is noticeable at the time of the radio burst, indicated by red vertical lines.

A dynamic spectrum of the burst was recorded in the LBA band by remote station RS509 and is shown in Figure 5.2b. The inset shows a number of striations from 34 - 35 MHz and the white cross indicates the time and frequency at which the images described in Section 5.3 are made.

The maximum baseline of the LOFAR observation is 84 km giving sub-arcminute

resolution across almost all of the observed frequency range and offering an unprecedented level of spatial resolution.

5.3 Data analysis and results

The source sizes and positions of solar radio bursts in LOFAR data have typically been obtained by the tied-array imaging mode. Tied-array imaging has the distinct advantage over interferometric observations in that it retains the ∼12 kHz frequency resolution and ∼0.01 s temporal resolution from LOFAR beamformed observations but it also contains a significant limitation. Tied-array observations can only be made using the LOFAR core stations as they share a single clock (de Gasperin et al., 2019), which makes it possible to add beamformed data coherently. This means that the maximum baseline from tied-array observations is approximately 2 km corresponding to an angular resolution of ∼17 arcmin at ∼30 MHz. Not only this, but the effect of interpolation between each tied-array beam on the observed source size has not yet been compared to observations done interferometrically. It is therefore unclear whether previously observed source sizes are in fact due to the underlying source, or an effect of the imaging technique. Solar campaigns with LOFAR are now performed with a new mode which allow for simultaneous interferometric and tied-array observations. A detailed comparison of these modes is currently under study, which should resolve the ambiguity in source sizes determined with tied-array observations (Morosan, D. E. 2020, private communication).

In order to avoid such limitations of the tied-array mode, here we use interferometric observations from the LOFAR core and remote stations, offering a longer baseline of 84 km and hence much better spatial resolution. The LOFAR data from this observation were calibrated using the Default Preprocessing Pipeline (DPPP; van Diepen et al., 2018) and a co-temporal observation of Virgo A. This corrects for effects such as antenna band-pass, clock drift and propagation effects through the ionosphere (de Gasperin et al., 2019). Correcting for antenna band-pass means accounting for the

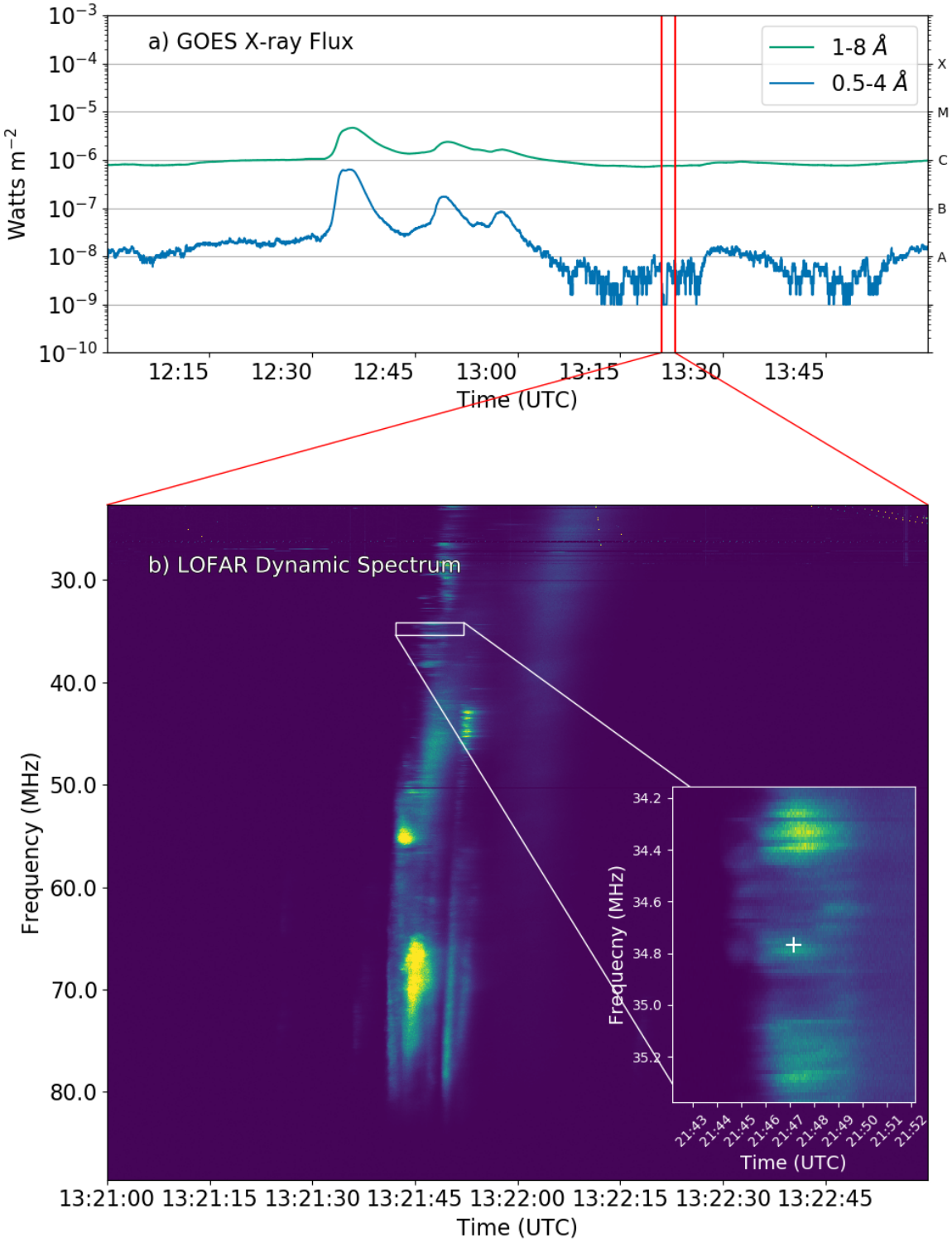

Figure 5.2: The X-ray light curve and radio dynamic spectrum for 17 October 2015. **a)** GOES X-ray lightcurves for the duration of the LOFAR solar observation. Minimal activity other than a number of C class flares prior to 13:00 UTC is observed. Red vertical lines indicate the time range of radio analysis. **b)** Dynamic spectrum of a type IIIb solar radio burst observed with LOFAR station RS509. The inset is a zoom of the region in the white box showing striation in the burst. The white cross indicates the time and frequency at which the images described in Section 5.3 are made. The intensity was not calibrated for this observation.

sensitivity of the LOFAR antennas at different frequencies (e.g. Figure 3.3). Clock drift occurs when the clocks on two different remote stations read slightly different times, this can introduce errors when the signals are correlated if the effect is not corrected. The ionosphere is an ionised medium and as such, radio waves propagating through it can be refracted and scattered, if these effects are not taken into account, the absolute position of an imaged source may be incorrect. I next describe the technique of directly fitting the LOFAR visibilities to estimate radio source size and position.

To produce an image from interferometric observations, an inverse Fourier transform is performed on the observed visibilities, usually followed by a deconvolution of the array point spread function (PSF) from the resulting "dirty-map" of the sky-brightness distribution. For such a deconvolution, LOFAR uses an implementation of the multi-scale CLEAN algorithm known as WSClean (Offringa et al., 2014). In this procedure a weighting may be applied to the visibilities to improve sensitivity to various spatial scales, the most common of which is the Briggs robustness weighting scheme (Briggs, 1995). Recreating a radio image in this way can introduce artefacts depending on the Briggs robustness used, the number of iterations of the algorithm and a number of other parameters described in more detail in Högbom (1974); Cornwell (2008); Offringa et al. (2014); Offringa & Smirnov (2017) for example. These artefacts include changes to the source shape and size (see Figure 3.15 for an example). Therefore, to avoid ambiguity in the source size, shape and position due to such imaging algorithms, I directly fit the measured visibilities similar to a method used for X-ray observations using the Reuven Ramaty High Energy Solar Spectroscopic Imager (RHESSI Hurford et al., 2002; Kontar et al., 2010). I describe this method in the following subsections.

5.3.1 Fitting the visibilities

The *uv* plane is a Fourier space representation of antenna pair positions. Each point in the *uv* plane is sensitive to emission of a particular angular scale. Due to the timescales over which type III bursts occur, solar observations are limited to a sparse sample of the *uv* plane and techniques to increase samples in this plane, such as aperture synthesis,

cannot be used. However, the large brightness temperatures of type III and type IIIb radio bursts (Reid & Ratcliffe, 2014) give rise to a high signal to noise ratio which allows a direct fit of a model to the visibilities. In the following it is assumed that the emitting source is a single elliptical Gaussian. This is based on the dynamic spectrum in Figure 5.2b, showing the type IIIb burst does not overlap any other bursts and as such is probably the only source in an interferometric image. The assumption leads to the convenient fact that an elliptical Gaussian in real space is observed as another elliptical Gaussian in the uv plane. The form of this Gaussian is

$$V(u,v) = e^{-2\pi i(ux_0+vy_0)}\left(\frac{I_0}{2\pi}e^{-\left(\frac{\sigma_x^2(2\pi u')^2}{2}-\frac{\sigma_y^2(2\pi v')^2}{2}\right)}+C\right) \tag{5.3}$$

where x_0, y_0 are the x and y coordinates of the source centre in real space, σ_x, σ_y are the standard deviation in the x and y direction and C is a constant background. Here the visibilities have been rotated to a new coordinate frame with axes u' and v' which are parallel and perpendicular to the major and minor axes of the Gaussian source such that $u' = u\cos\theta - v\sin\theta$, $v' = u\sin\theta + v\cos\theta$, where θ is the angle of the major axis to the x axis, i.e. the position angle of the Gaussian on the uv plane.

A nonlinear least squares fit is applied to the sample of visibilities in two stages. First, the source size, maximum intensity and angle relative to the x axis are found by fitting the absolute value of the complex visibilities also known as the amplitude. In order to determine source location, the phase angle of the data is fitted. Source location in real space determines fringe separation and orientation in Fourier space. The direct fitting of parameters to $V(u,v)$ is then used to recreate the sky brightness distribution or image $I(x,y)$, which is the inverse Fourier Transform of Equation 5.3. The nonlinear least squares fit is implemented in the `lmfit` python library (Newville et al., 2014) which uses the Levenberg–Marquardt algorithm to minimise the sum of least squares between the model, Equation 5.3, and the measured visibilities.

Although the computational time to perform a model fit to the visibilities is much less than creating a CLEAN image (10s of seconds compared to minutes), ensuring

that the calibration was successful at a particular time and frequency is still a labour intensive process. Particularly bright radio emission from the Sun can corrupt the observation of the calibrator source giving spurious values in the calibration solution. Considerable time was invested in identifying successful calibration using expert knowledge, gathered from many hours of interferometric imaging. Extending the analysis to other frequencies and times was thus deemed to be too much effort for the return.

Figure 5.3 shows the fit of the modelled Gaussian to the complex visibilities. Due to the fact that this fit is done in Fourier space, the amplitude and phase of the data and fit are shown in the *uv* plane in Figure 5.3a and 5.3b respectively. Here, the points are the observed visibilities and the background colour map is the fit. In Figure 5.3a a red ellipse indicates the full width at half maximum height (FWHM) of the fitted Gaussian. The fringes in Figure 5.3b show the fit of the source position to the distribution of visibility phases across *uv* space. Figure 5.3c shows the increase in the amplitude of recorded visibilities with the angular scale on the sky that causes this increase. The red curves are where data points would lie for a Gaussian in visibility space with the FWHM in the major and minor direction obtained from the fit in Figure 5.3a.

The visibility fit reveals a source with a FWHM in real space of 18.8 arcmin ±0.1 arcmin and 10.2 arcmin ±0.1 arcmin, in the direction of the major and minor axis, respectively. The source is found at a position of $-1312''$, $-1064''$ from the solar centre giving a plane of sky distance of $1.75\,R_{\odot}$. The parameters from the fit can then be used to recreate a sky-brightness distribution $I(x, y)$ in real space which is shown as contours over-plotted on a 171 Å image taken by the Atmospheric Imaging Assembly (AIA; Lemen et al., 2012) in Figure 5.4. Note that, despite the theoretical high angular resolution of the long baselines afforded by LOFAR remote stations (84 km), the source size is still large and there is little evidence of angular scales smaller than ∼10 arcmin in Figure 5.3c. I will discuss this further in Section 5.4.

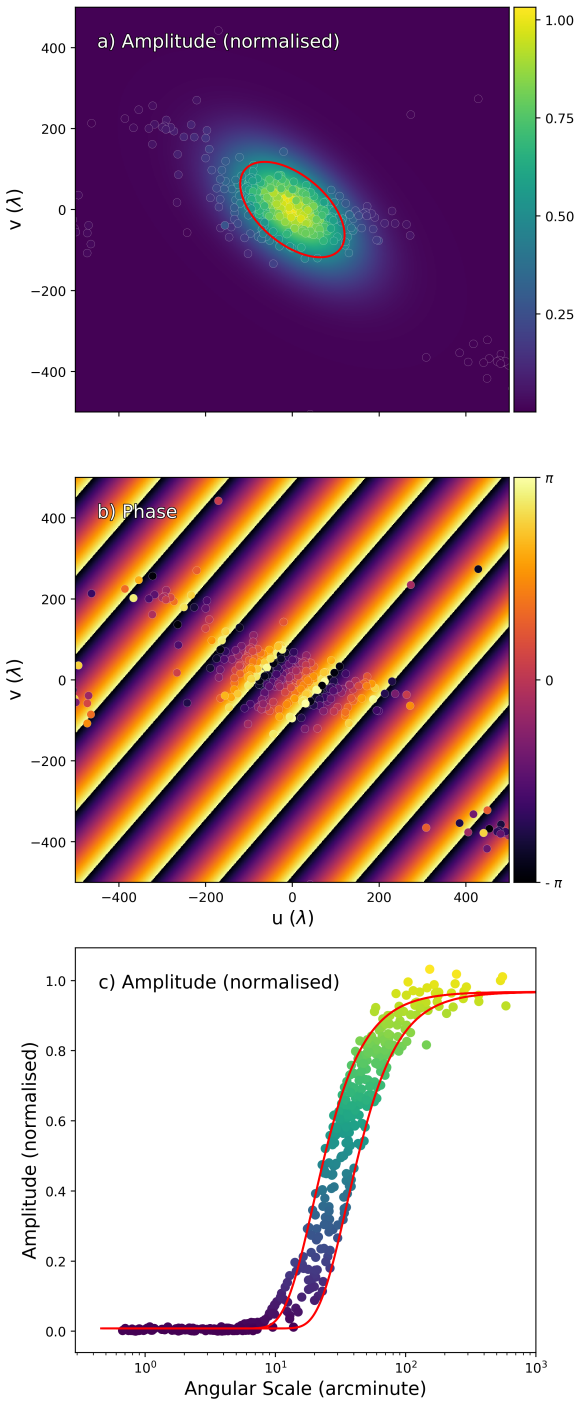

Figure 5.3: Modelled visibilities determined from a direct fit to observed interferometric visibilities. **a)** Amplitudes of visibilities in the *uv* plane for LOFAR observation. Background colour map shows a Gaussian fit. Red ellipse shows the FWHM of the normalised amplitude. **b)** Visibility phase in the *uv* plane. Background colour map shows fitted phase angle. The fringe spacing is indicative of the distance of the source from the centre of the image while their orientation gives information on the source position. **c)** Visibility amplitudes received from different angular scales. Red curves indicate the FWHM of the semi-major and semi-minor axes of the fitted Gaussian.

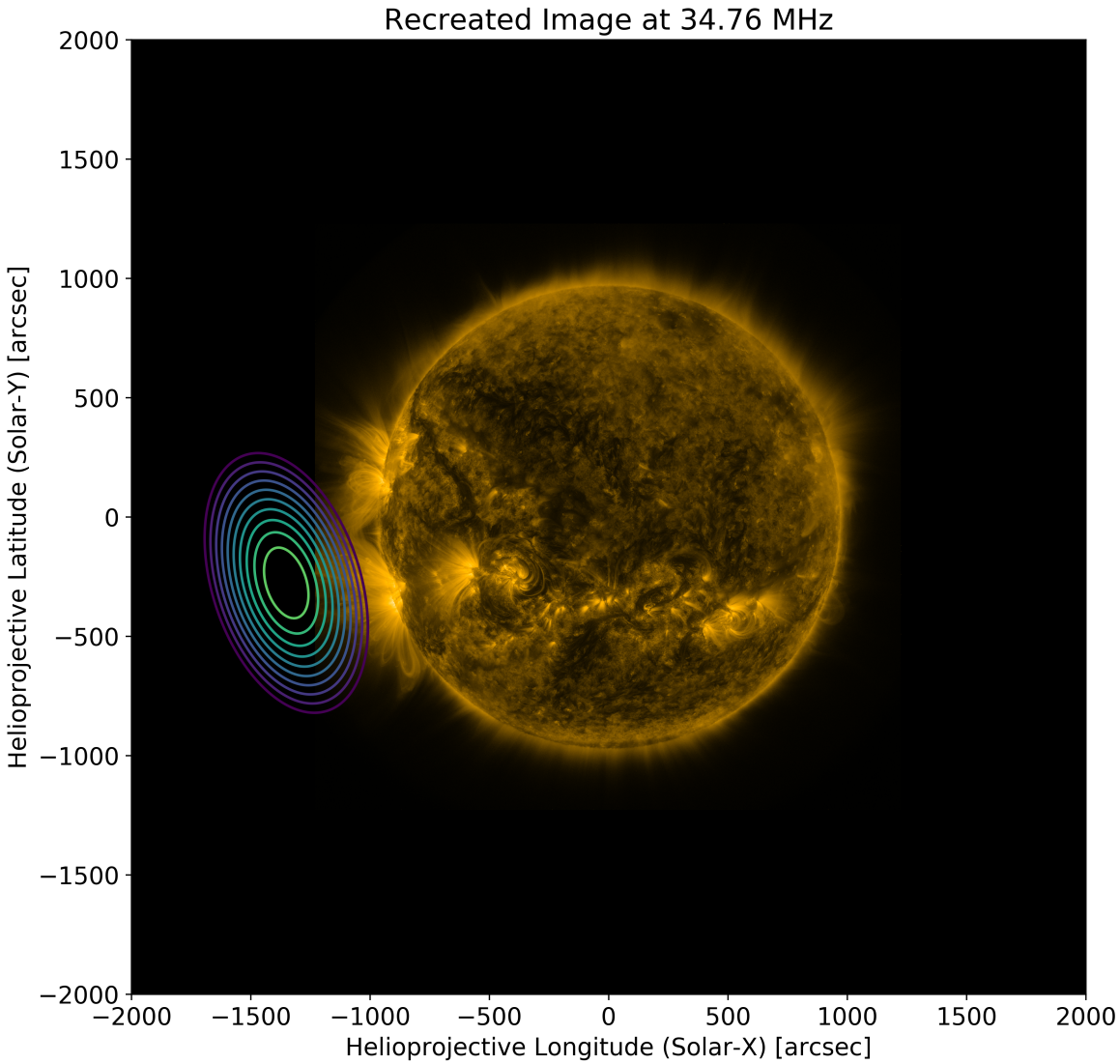

Figure 5.4: Recreated sky intensity profile of a type IIIb radio burst occurring at 13:21:46 on 17 October 2015. The contours show a Gaussian source whose size and position are determined from the model fit to Equation 5.3. The contour levels start at 50% of the maximum value and increase in steps of 5%. The background solar image is an AIA 171Å image at 17 October 2015 13:21:46 UTC.

5.3.2 Type IIIb striae

In the above I determined the source size and position using a direct modelling of LOFAR visibility observations. This provides us with an opportunity to compare the observed source size to its actual size, which can be estimated from spectroscopic observations, similar to the method of Kontar et al. (2017).

To estimate the source size from spectroscopic measurements, I relate the FWHM of the frequency of the striation to its vertical extent in the solar corona $\Delta r \sim 2L\,(\Delta f/f)$ where L is the characteristic density scale height (Kontar et al., 2017) determined using a Newkirk (1961) density model. Assuming emission occurs at the distance where the plasma frequency is ~ 35 MHz, this gives $L \approx 6200$ km. A single striation was manually identified at 34.76 MHz from the dynamic spectrum. The time of maximum intensity for the burst was found and a vertical frequency slice was obtained from which $\Delta f/f$ was calculated. The individual striation, the centre of which is indicated by a white cross in the inset panel of Figure 5.2b, was fitted with a Gaussian. The value for Δf of the striation was found to be $\Delta f \sim 0.2$ MHz. The ratio of frequency to bandwidth for the striation was found to be $\Delta f/f = 0.006$, leading to an estimated source size of 3.18 arcsec. Similar to Kontar et al. (2017), this is far smaller than the source size observed from the visibility fit.

In the following section I will discuss why the most probable cause for the discrepancy in source size is radio scattering, as well as a discussion on the comparison of this observation to recent developments in the theory and the effect scattering has had on actual source size and position.

5.4 Discussion

Adopting the theory described by Takakura & Yousef (1975) and used in Kontar et al. (2017), the predicted source sizes of a type IIIb striation are much smaller than what is observed. The most probable cause for this discrepancy is a combination of radio light scattering in the solar corona, propagation effects in the Earth's ionosphere and

limitations due to angular resolution. With this observation we accounted for and corrected ionospheric effects in the calibration step (Section 5.3 and de Gasperin et al., 2019) thereby removing the largest uncertainty in source size and position. By fitting the source size directly in visibility space we can directly see the power at which different angular scales were observed. The *uv* coverage of this observation allows angular scales of ∼42 arcsec to be observed (Figure 5.3c) and although the predicted source size of ∼3 arcsec is smaller than this, the amplitude of the observed visibilities does not increase until ∼10 arcmin indicating that this is, in fact, the smallest source size observed in the visibilities.

It should be noted that there is better *uv* coverage along one axis compared to its orthogonal which may have an effect on the eccentricity of the elliptical Gaussian fit. However, owing to the qualitatively similar shape as predicted by Kontar et al. (2019) for a burst originating near the solar limb, I am confident that the eccentricity is representative of the real source. The orientation and elongation of the source are also consistent with observations of anisotropic scattering in the solar wind (Anantharamaiah et al., 1994; Ingale et al., 2015) where scattered sources are elongated perpendicular to the large scale (radial) magnetic field of the Sun.

Having accounted for all systematic effects that can affect the source size, I conclude that the large source sizes observed in this observation are due to the effect of scattering in the solar corona only. Previous tied-array observations have similar conclusions, however the tied-array technique interpolates data from a tessellation of beams across the Sun, and this introduces an ambiguity to the origin and size of sources. I assume the origin of the radio source to be somewhere above the active regions close to the East limb. An exploratory potential free source surface (PFSS) extrapolation suggests open field lines at an angle of θ_s∼20° from the plane of sky towards the observer. Similar to Chrysaphi et al. (2018) (Equations 5 and 6), an out-of-plane heliocentric distance for the source can be determined. Using the observed in-plane heliocentric distance and an angle of θ_s∼20° from the plane of sky, I obtain an out-of-plane heliocentric distance of 1.82 $R_\odot$. Comparing this to Figure 8 in Kontar et al. (2019), which shows

the effect of the angle from the plane-of-sky θ_s on source position and FWHM size in the major and minor axis, one would expect a ratio of the FWHM on the minor axis to the FWHM of the major axis to be of the order of 0.6. These observations show a ratio of 0.54 suggesting $\theta_s \sim 20^\circ$ is an appropriate approximation for the angle from the plane-of-sky.

The FWHM of the source at 34.76 MHz along the major and minor axis for this observation are 18.8 arcmin $\pm$0.1 arcmin and 10.2 arcmin $\pm$0.1 arcmin respectively. This gives the FWHM area of the source to be $A_s = 150.6$ arcmin^2, which I note is smaller than that of Kontar et al. (2017) who measure $A_s = 400$ arcmin^2 at a similar frequency of 32.5 MHz. While this could be simply due to these being two separate observations, this may be more indicative of a discrepancy between source sizes measured in interferometric observations and tied-array observations. As mentioned in Section 5.3, the spatial resolution of LOFAR interferometric observations is superior to that of tied-array observations. This is mostly due to the additional stations that can be used for interferometric imaging and thus greater baseline lengths, but also due to the way tied-array images are made. Tied-array observations are carried out by pointing a number of beams in a honeycomb like pattern centred on the Sun and interpolating data from each of the tessellated beams. The effect of this on observed source sizes and position is, as of yet, uncharacterised. Kontar et al. (2017) attribute the large source size observed in their tied-array observation of a type IIIb radio burst to the scattering of radio waves by density inhomogeneities in the solar corona. It was later determined that a relative rms fluctuation of electron density of $\varepsilon = 0.8$ was necessary to explain the large source size observed Kontar et al. (2019). While it is evident that radio wave scattering causes radio bursts to appear larger in observations than predicted, the reduced spatial resolution of tied-array imaging may result in an overestimate of ε.

The last decade has seen a renewed interest in low frequency observations of the radio sun with state of the art radio interferometers such as LOFAR and the MWA. Radio bursts emitted via the plasma emission process give a diagnostic of the local

plasma density which may give insight into the turbulent nature of coronal plasma. It is theorised that the size of low frequency radio emission is limited by scattering caused by turbulence (Bastian, 1994), however it is only recently that the angular resolution necessary to challenge this theory has become available. In particular, a robust comparison of sources observed with tied-array and interferometric imaging is needed. Analytical approximations of radio scattering (e.g. Chrysaphi et al., 2018; Gordovskyy et al., 2019; Sharma & Oberoi, 2020) have seen some success in accounting for apparent source shift and brightness temperature due to scattering, however they cannot account for the anisotropic nature of scattering and may not be appropriate to describe large angle scattering near the source location. As such, a full numerical treatment of scattering (e.g. Thejappa & MacDowall, 2008; Bian et al., 2019; Kontar et al., 2019), in combination with interferometric imaging, is necessary to fully understand radio wave propagation in the turbulent coronal plasma. In order to definitively determine ε, more information on the power spectrum of density fluctuations and the scales on which radio scattering most effectively occurs is needed.

5.5 Conclusion

In summary, a type IIIb radio burst was observed with LOFAR on 17 October 2015 at approximately 13:21:00 UTC. The bandwidth of an individual striation at 34.76 MHz suggests a FWHM source size of 3.18 arcsec. Directly fitting visibilities to avoid effects of deconvolution algorithms reveals a FWHM source size in the major and minor axes of 18.8 arcmin $\pm$0.1 arcmin and 10.2 arcmin $\pm$0.1 arcmin respectively. The source is located at $-1312''$, $-1064''$ from the solar centre. Having corrected for radio wave propagation in the ionosphere, I conclude that scattering from electron density fluctuations in the solar corona is the main cause of source broadening. I discuss how values for the rms relative electron density fluctuations determined from numerical models and compared to tied-array observations may be an overestimate. In the future, a combination of remote observations from LOFAR and *in situ* measurements of plasma properties

from PSP and Solar Orbiter (Müller et al., 2013, 2020) at a variety of heliocentric distances in the corona and solar wind will be needed to form a more complete picture of coronal turbulence.

6

The intrinsic sizes of type III radio bursts and comparison to recent simulations.

Recent developments in the modelling of radio waves in a turbulent corona have made predictions about source sizes that have not yet been qualitatively compared to interferometric observations. Scattering of radio waves by density inhomogeneities in the solar corona is considered to be the dominant cause of the size and shape of radio bursts. By understanding scattering, the turbulent nature of processes that generate density inhomogeneities can be studied. Turbulence in the corona can give insight into how energy is transferred from large scale phenomena down to the microscales, potentially resulting in the million degree Kelvin temperatures that have puzzled solar physicists for decades. New models of radio wave scattering, therefore, are one of the first steps to solving fundamental physical problems in the solar corona. However, unless the models agree with observations, their use is limited and, as such, comparisons between models and observations are crucial. In this chapter I utilise the direct visibility fitting method described in Chapter 5 and apply it to 29 type III radio bursts observed with LOFAR from 10-90 MHz. Using a Markov Chain Monte Carlo (MCMC) fitting method, it is determined that these bursts have a mean size along the major and minor axis of $\mathrm{FWHM_x} = 16.27$ arcmin and $\mathrm{FWHM_y} = 11.96$ arcmin respectively. No trend of source size with respect to helioprojective angle is found, which is in contrast to predictions from state-of-the-art radio wave scattering models. I discuss reasons for this discrepancy and how improved imaging and additions to scattering models can be used to resolve them.

6.1 Introduction

The computational modelling of radio wave scattering has seen considerable development over the 50-odd years since some of the first simulations by e.g. Fokker (1965)

and Steinberg et al. (1971). The theory for these early works followed from a generalisation of Chandrasekhar (1952), as was discussed in Chapter 2, and was developed to explain the observations of radio burst source size, position, directivity (power received from source in some solid angle compared to power from an isotropic source in the same solid angle) and time profile. These models considered scattering of radio photons by density inhomogeneities in the solar corona. Notably, each of these scattering events occurred at a small angle. Simulations of this kind fell out of favour by the mid 1980s and remained mostly dormant until Thejappa et al. (2007) investigated the source directivity and time profiles of bursts using a different power spectrum of isotropic density inhomogeneities. In the studies by e.g. Fokker (1965) and Steinberg et al. (1971), the inhomogeneities were assumed to have a Gaussian power spectrum. However, in the intervening 30 years knowledge of turbulence in the solar corona proved this assumption to be incorrect. As mentioned in Chapter 5, Coles & Harmon (1989) collated the results of numerous observations to give the following description of the density inhomogeneity power spectrum, shown in Figure 5.1. At large scales, greater than a few hundred kilometres, the spectrum is well described with a power law index of -5/3, which agrees with the Kolmogorov description of turbulence (Kolmogorov, 1941). For scales smaller than these but greater than a few kilometres, the spectrum becomes shallower and is better described with a power law index of ~ -1. Finally, on the smallest scales less than a few kilometres the spectrum steepens again. This steepening has been interpreted as the scale at which energy is dissipated by turbulence. Coles & Harmon (1989) also found that this inner scale increases with heliocentric distance. Bastian (1994) expanded on this description of the density inhomogeneity power spectrum and investigated the angular broadening of radio waves sources at centimetre wavelengths.

Comparisons between the models mentioned above and observations of radio bursts have also developed over time. Stewart (1972) compared the observed positions of fundamental and harmonic emission and related it to the then contemporary scattering models (e.g. Fokker, 1965; Steinberg et al., 1971). As our knowledge of solar turbulence

and the power spectrum of density inhomogeneities improved so too did the instrumentation, allowing for more accurate observations of radio bursts and thus more accurate comparisons. In particular, radio interferometers such as LOFAR and the MWA have the angular resolution to investigate radio emission from both bursts (e.g. Zhang et al., 2020) and the quiet sun (e.g. Sharma & Oberoi, 2020).

The latest development in the modelling of radio wave scattering is by Kontar et al. (2019). Rather than using the small scattering angle approximation of previous work, Kontar et al. (2019) build on the work of Arzner & Magun (1999) and Bian et al. (2019). In this approach, the effect of anisotropic density inhomogeneities is treated as photon diffusion in momentum space and the Hamiltonian equations for photon position and momentum can be solved iteratively to trace a photon's path. This allows for a continuous transition from weak to strong scattering, whereas previous work was limited to regime of small angle scattering. Kontar et al. (2019) assume a spherically symmetric corona with an anisotropic distribution of electron density fluctuations, with wavenumber $\mathbf{q}$, such that $q_{\parallel}$ is parallel to the local radial direction. They perform Monte Carlo simulations of photons emitted from a point source at $\omega = 1.1\omega_p(R_s)$ via fundamental plasma emission at a distance R_s and an electron density from the Parker (1960) density model of a spherically symmetric corona with constant temperature. In the Kontar et al. (2019) model, the kinematic properties and arrival time of each photon was recorded at a predetermined distance from the burst source where scattering is considered negligible. An image was then created by projecting photons directed towards the observer back to the plane of the source. For a radio burst that would be observed at ~ 35 MHz ($f_p = \omega_p/2\pi \sim 32$ MHz), Kontar et al. (2019) find that value for the root mean square (r.m.s) of density fluctuations $\varepsilon = 0.8$ and an anisotropy factor of $\alpha = 0.3$ are necessary to explain previous observations (Kontar et al., 2017). The effect of source location on the modelled image are also investigated and it is found that sources appear more elongated in solar latitude close to the disk limb than they do at disk centre. Kontar et al. (2019) determine that this effect is less evident when an anisotropy factor of $\alpha = 0.5$ is used.

The conclusions of Kontar et al. (2019) have not yet been qualitatively compared to observations of radio bursts. In particular, whether a relationship between the source size and its location on the solar disk exists is an easy test of the validity of recent modelling efforts. In order to verify this relationship, one can measure the source eccentricity at various heliographic longitudes. However, due to the effects of imaging algorithms on observed source size, extreme care must be taken in this regard. The approach taken here directly fits a 2D elliptical Gaussian to the interferomteric visibilities, thereby eliminating the need to produce images. Here I improve upon Murphy et al. (2021) by implementing a Markov Chain Monte Carlo fitting method to get a robust description of fitting uncertainties. The position and size of the burst in the minor and major axes ($FWHM_x$ and $FWHM_y$ respectively) can be determined from this fitting and used to calculate the eccentricity or "aspect ratio" of the burst i.e. $FWHM_x/FWHM_y$.

Observations of radio bursts contain information on the scattering effects of radio waves as they travel through the corona to the observer. The process that determines this scattering needs to be fully understood before information about the solar corona can be determined from observations of radio bursts. By measuring the aspect ratio of type III bursts as a function of heliographic longitude, a direct comparison can be made to the predictions of state-of-the-art scattering simulations. If they are in agreement, we may be able to use information about the scattering effects on a source to remotely determine the physics of coronal plasma.

6.2 Observations

During the period 04 April 2019 to 14 April 2019 a type III storm occurred on the Sun. This storm was observed in the frequency range of 20 - 80 MHz using LOFAR in both tied-array and interferometric mode. Interferometric visibilities at a frequency of 30.47 MHz from 12:00 UTC - 13:00 UTC on April 4-8 and 11-14 are used for this study. During this time a large active region (AR) rotated across the solar disk. Figure

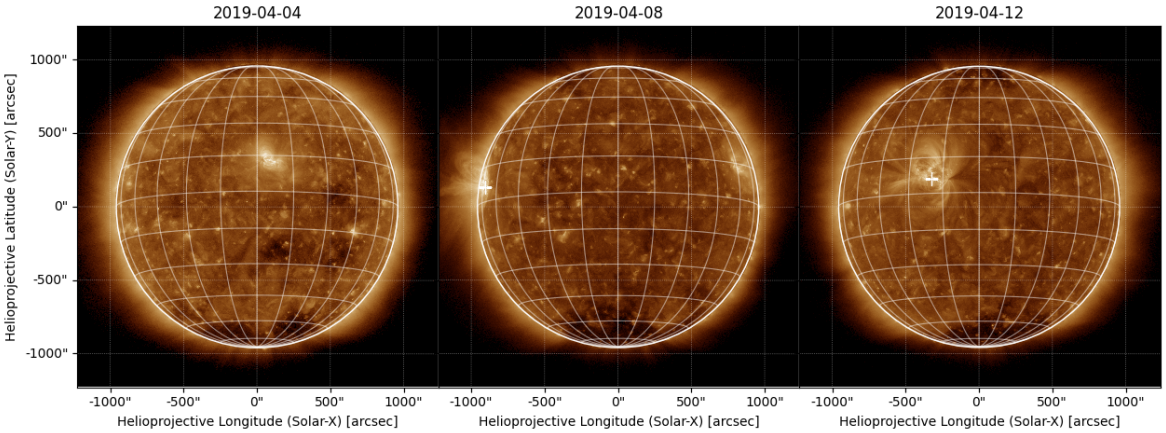

Figure 6.1: Evolution of active region 12738 as it revolves around the disk. Images are in the 193 Å passband of AIA showing hot material in the solar corona. It is expected that type III bursts should be centred above the active region. The left panel shows the Sun on the first day of the observation where active region 12738 has not yet rotated onto disk. The middle panel shows the active region on the solar limb and is the first day where the active region is classified. The right panel shows the active region closer to the centre of the disk. In both the middle and right panel active region 12738 is marked with a white cross.

6.1 shows the active region with NOAA identification number 12738 revolves onto the disk. The active region is first classified on 08 April 2019 as a unipolar sunspot under the Hale classification and evolves to a bipolar structure by 14 April 2019. Assuming type III radio bursts occur above this active region, it offers a perfect opportunity to study the variation of source size and shape with respect to position. The heliographic longitude of AR 12738 changes by $\sim 80^{\circ}$ from close to the limb on 08 April 2019 to close to disk centre on 14 April 2019. This is an ideal range to measure variability of source size with respect to longitude.

6.3 Method

The size and position of 29 type III radio bursts over the period of 04 April 2019 to 14 April 2019 were determined by directly fitting their interferometric visibilities. Only bursts which occurred between 12 UT and 13 UT were analysed. The time of day was chosen so that the Sun was at its highest point in the sky and thus any radio light would propagate through a minimum amount of ionosphere. This was done in an effort to have consistency across multiple days of observation. The bursts were identified in LOFAR beamformed observations and their peak time determined using an

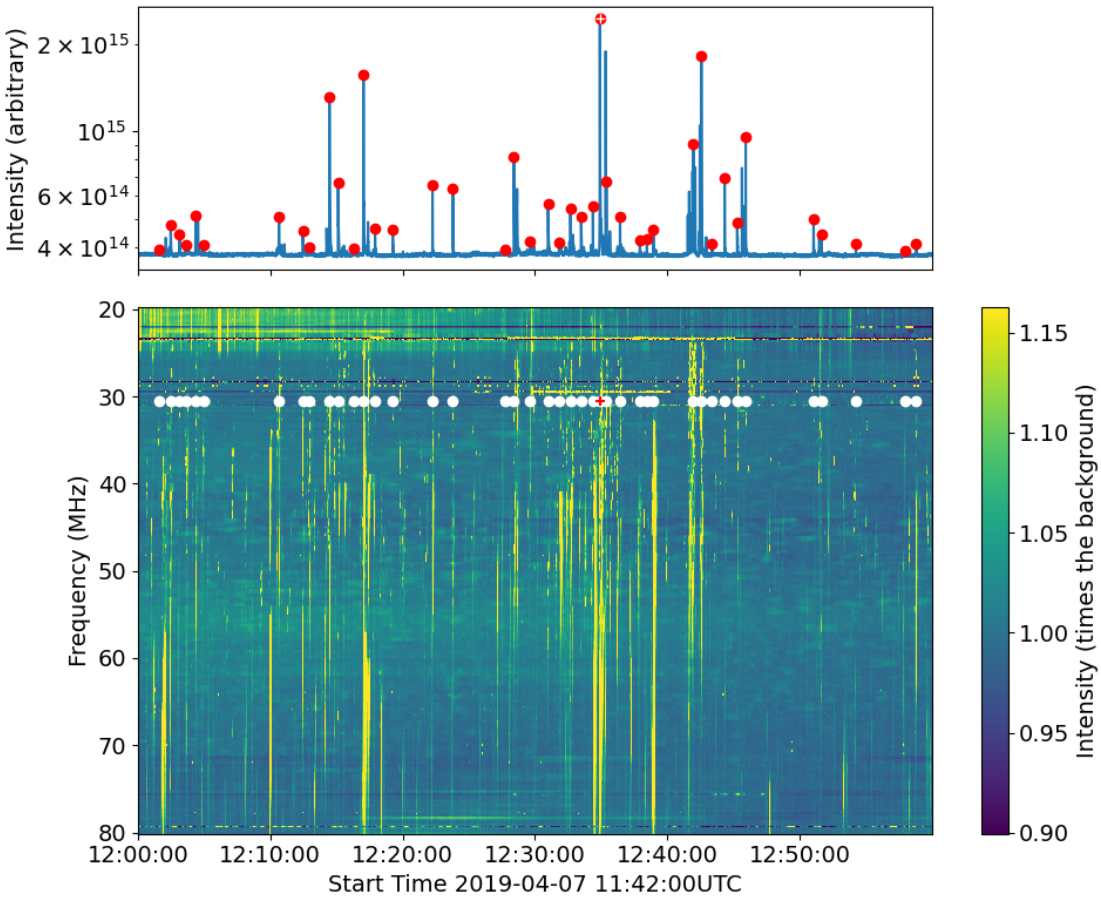

Figure 6.2: Type III storm observed on 07 April 2019. The top panel is the light curve at 30 MHz and the red dots indicate the detected peaks. The maximum peak is marked with a white cross. The bottom panel shows the dynamic spectrum of the storm with the colourbar showing intensity above the background. The white dots indicate the bursts identified by an automatic peak finding algorithm, the red cross indicates the brightest burst.

automatic peak finding algorithm. Peaks are found from the spectrum by first averaging over 16 subbands around 30 MHz, in order to match the spectral resolution of the interferometric observation, and smoothing the resulting time series. Then the `scipy` Python library (Virtanen et al., 2020) is used to determine the peaks by comparing to neighbouring values. This list of peaks is filtered so that only peaks greater than the background plus five times the standard deviation are returned. Figure 6.2 shows the automatically identified bursts at 30 MHz. In total, 320 bursts were identified in this way.

Unfortunately, due to the intensity of many radio bursts exceeding $\sim 500kJy$, the calibration of interferometric data did not converge for $\sim 90\%$ of them. This occurs

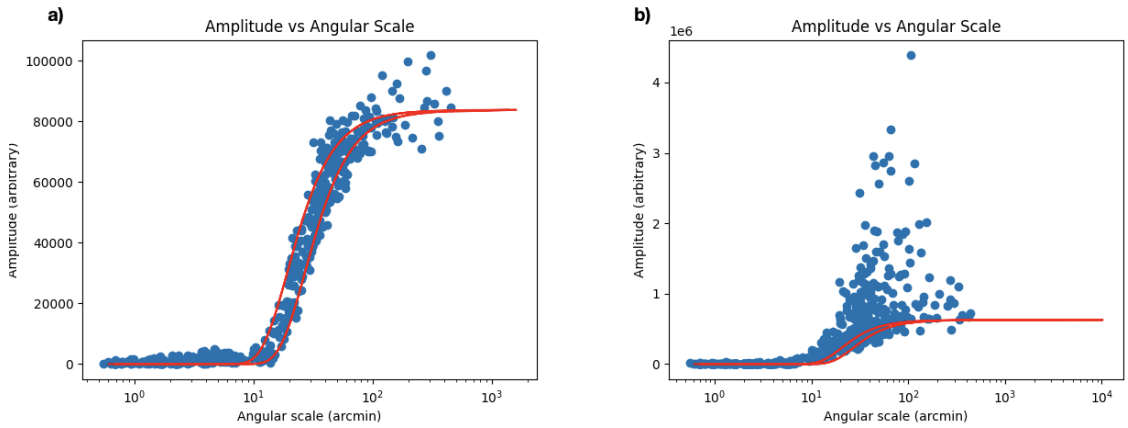

Figure 6.3: Comparison of type III burst visibilities with good and bad calibration. Plotted are the amplitude of the burst visibilities with respect to angular scale in arcmin for a burst where calibtration did (a) and did not (b) converge. The red lines are the 2D Gaussian fitted to the visibilities.

when flux from the source is detected in the side lobes of the beam observing the calibrator. An example of burst visbilities with good and bad calibration solutions is shown in Figure 6.3a and Figure 6.3b respectively.

In order to determine the position and size of the identified bursts, their visibilities were fitted with a 2D elliptical Gaussian at the time of the peak maximum. This makes the assumption that the burst is the only emitting source in the visibilities. To estimate the error in each fit the probability distribution for the parameters determined. This can be done by employing a Markov Chain Monte Carlo (MCMC) technique. MCMC methods generate samples from a probability distribution, in this case the posterior probability density function of the fitting parameters, x, given the data, D,

$$p(x|D) \propto p(x)p(D|x). \tag{6.1}$$

The most common form of MCMC algorithm is the Metropolis-Hastings (M-H) method which I will outline below. Starting at a particular state $x^{(t)}$ a proposed new state x' is drawn from some proposal density $Q(x'; x^{(t)})$ which depends on the current state. $Q(x'; x^{(t)})$ is a probability distribution from which it is easy to generate samples, such as a multivariate Gaussian. In order to determine whether or not to accept the new

state the probability

$$a = \frac{p(x'|D)}{p(x^t|D)} \frac{Q(x'; x^{(t)})}{Q(x^{(t)}; x')}, \tag{6.2}$$

is computed. If $a > 1$ the new state is accepted and the next iteration occurs. Otherwise the state is accepted with probability a. Note that if a state is not accepted, the position $x^{(t)}$ is repeated on the chain. Successive samples in a Markov chain are dependent meaning that it is only as $t \to \infty$, that the probability density function of $x^{(t)}$ tends towards $p(x|D)$. An improvement to the M-H algorithm which speeds up convergence is proposed by Goodman & Weare (2010) and implemented in the `emcee` Python library (Foreman-Mackey et al., 2013). This method uses an ensemble of *walkers* to determine the proposal distribution. For each walker k in an ensemble of K walkers, the proposed state is determined by the positions of the remaining $K-1$ walkers in the ensemble. To determine a move for the walker at $x_k^{(t)}$, a walker $x_j, j \neq k$ is chosen from the ensemble and the proposed move has the form

$$x_k^{(t)} \to x' = x_j + Z(x_k^{(t)} - x_j). \tag{6.3}$$

Here, Z is a random variable drawn from the distribution

$$g(z) \propto \begin{cases} \frac{1}{\sqrt{z}} & \text{if} z \in \left[\frac{1}{a}, a\right] \\ 0 & \text{otherwise} \end{cases} \tag{6.4}$$

where a is an adjustable parameter set to 2 by Goodman & Weare (2010). The probability of accepting a proposed step is given by

$$q = \min\left(1, Z^{N-1} \frac{p(x')}{p(x_k^{(t)})}\right), \tag{6.5}$$

where N is the dimension of the parameter space. This process is then repeated in series for the remaining walkers in the ensemble. The ensemble of walkers for each parameter in the 2D Gaussian which is being fit are show in Figure 6.4. Each black line represents a walker's individual Markov Chain and the cyan line is the mean of

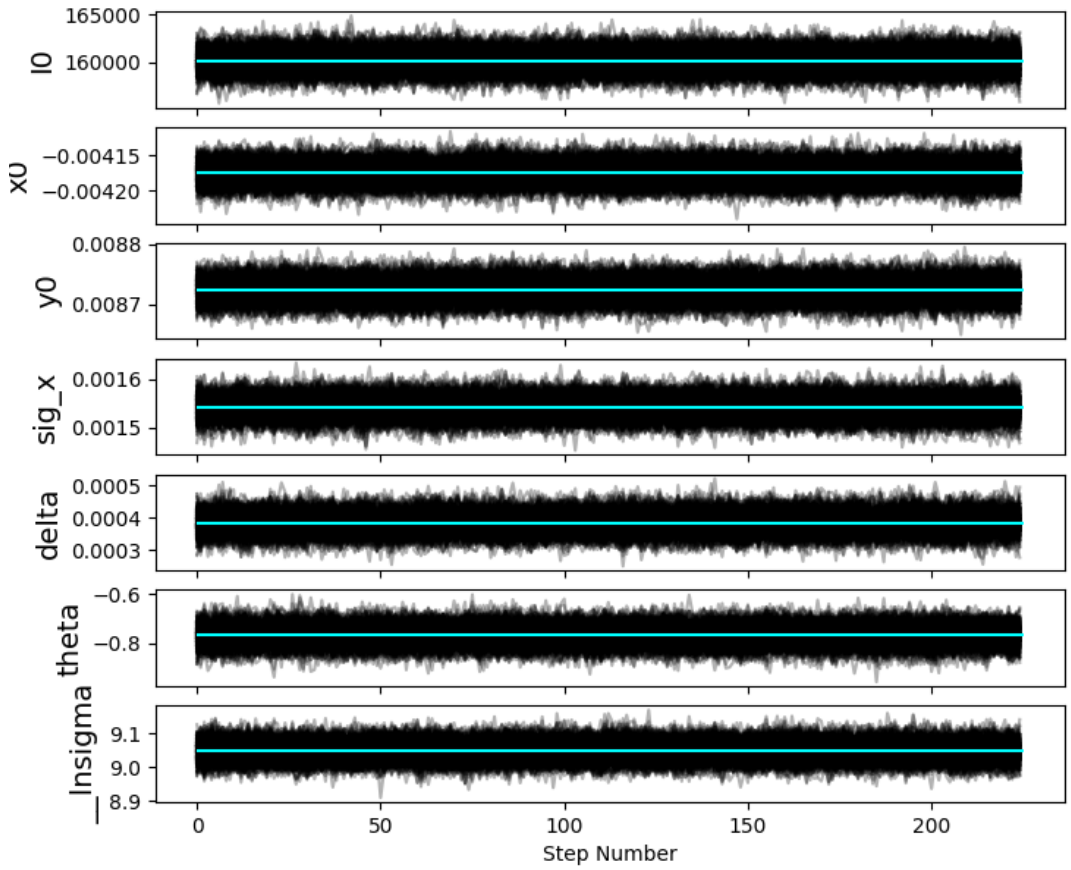

Figure 6.4: The Markov chain generated by 300 walkers for each parameter in visibility fitting. The parameters fit are as follows. `I0` is the amplitude of the Gaussian, `x0` and `y0` are the coordinates of its centre, `sig_x` is the standard deviation of the Guassian in the x direction, `delta` is an additive factor to find the standard deviation of the Guassian in the y direction such that $\sigma_y = \sigma_x + \delta, \delta > 0$, `theta` is the position angle of the Gaussian and `__lnsigma` is the log uncertainty of the visibilities. Horizontal cyan lines indicate the mean of the Markov Chain.

the ensemble. Here a "burn-in" time of 500 steps was used to allow the walkers to explore the parameter space and "forget" their initial position. This is a typical way to fine-tune an MCMC.

Once the MCMC has run for enough time to generate independent samples of the posterior probability density function, histograms of the samples can be projected into parameter space. The corner plot in Figure 6.5 shows the individual histograms as well as the 2D correlations between various parameters. This gives an excellent and robust measure of the error in each parameter.

The corner plots of all 320 identified bursts were manually inspected to identify

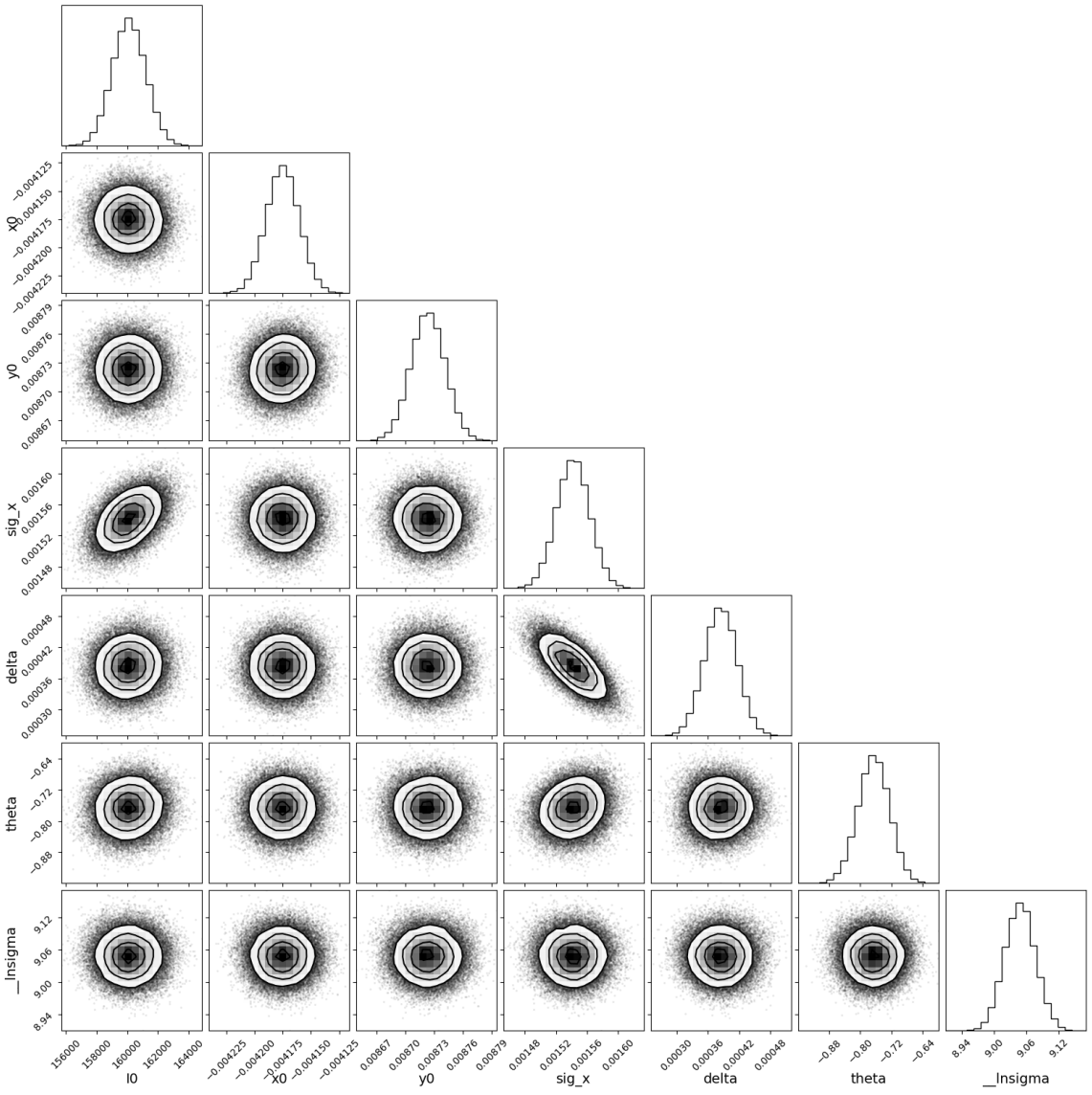

Figure 6.5: The corner plot of parameter histograms determined by MCMC algorithm. This shows the one (along the diagonal) and two dimensional projections of the sampled probability function. This can be used to determine the covariances between different parameters. The parameter labels are as described in the caption to Figure 6.4.

cases where calibration succeeded. Any that did not show gaussian-like distributions such as in Figure 6.5 were deemed to have failed. Calibration was successful for 29 bursts.

The magnetic field structure around AR 12738 was determined by using a Potential Field Source Surface (PFSS) model using the Python library `pfsspy` (Stansby et al., 2020). This library solves the equations for magnetic field assuming there is no electrical field. Boundary conditions for the magnetic field are imposed from a spherical shell starting at the solar surface and ending at some configurable outer radius, 2.5 $R_\odot$ in this case.

6.4 Results

The parameters for all 29 fitted bursts are given in Table 6.1 where I_0 is the maximum intensity of the burst, x_0 and y_0 are the x and y helioprojective-cartesian coordinates of the burst, $FWHM_x$ and $FWHM_y$ are the burst sizes along the minor and major axes of the Gaussian respectively and θ is the position angle of the fitted Gaussian.

The size of each burst, is plotted against the distance from the disk centre in the helioprojective-cartesian x and y direction in Figure 6.6. There is no trend in the aspect ratio of the bursts, which is expected to be a linear decrease from 1 near disk centre to < 1 near the limb.

Figure 6.7a shows a histogram of $FWHM_x$ and $FWHM_y$ in the range of 6 to 20 arcmin. The mean size of the bursts is indicated by a vertical grey dashed line and is 11.96 arcmin for $FWHM_x$ and 16.27 arcmin for $FWHM_y$. The histogram of burst aspect ratios is shown in 6.7b with the mean aspect ratio of the bursts ~ 0.74 plotted as a vertical dashed line. The relative angle of each burst i.e. the angle between the minor axis of the burst and a line from its centre to (0,0) in helioprojective-cartesian coordinates, is plotted as a histogram in Figure 6.7c. These peak are around $\sim -10°$ and have a mean indicated by a dashed green line at $-18.33°$.

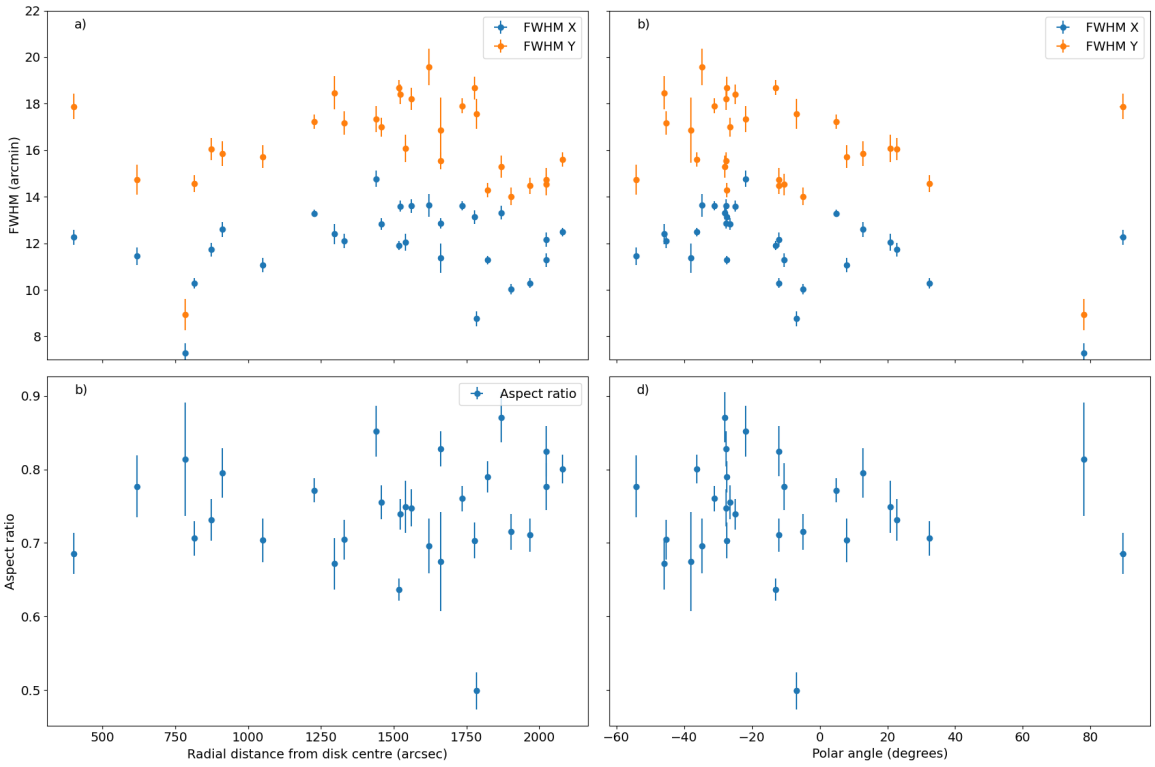

Figure 6.6: A comparison of the directly fitted type III burst sizes with respect to their radial distance from the disk centre and polar angle. Top row, $FWHM_x$ (blue) and $FWHM_y$ (orange) as a function of their radial distance from the disk centre (left) and polar angle (right). Bottom row, same as above except showing the "aspect ratio" of each burst. There is no obvious correlation with burst size or aspect ratio with respect to distance from disk centre or polar angle.

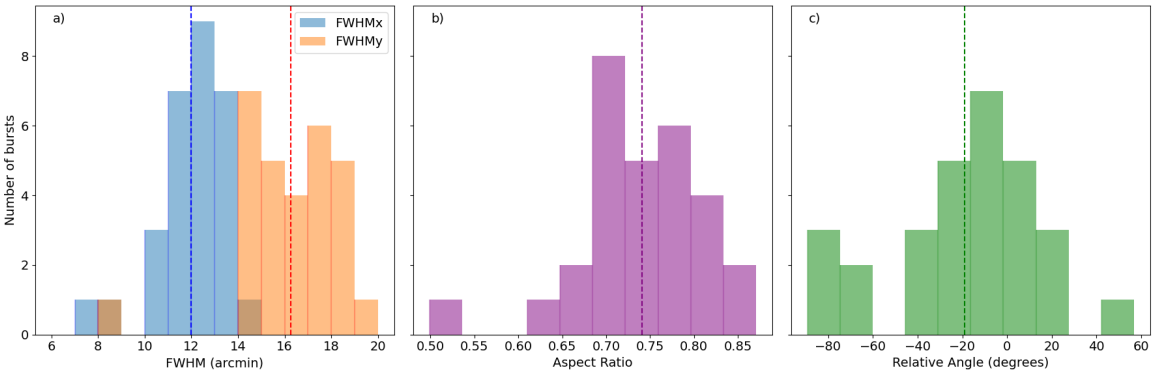

Figure 6.7: a) Histogram of type III burst sizes. Bins are 1 arcmin wide and the vertical dashed lines indicate the mean value for $FWHM_x$ (blue) and $FWHM_y$ (orange). A peak in the $FWHM_x$ of the bursts could suggest an intrinsic size while the possible double peak in $FWHM_y$ shows that scattering effects cannot simply be determined from burst size alone. b) Histogram of type III burst aspect ratios. The vertical purple dashed line indicates the mean value for the aspect ratio $FWHM_x/FWHM_y$. A peak here possibly indicates that the observed aspect ratio depends more on the intrinsic size of a burst than the scattering effects. c) Histogram of type III burst relative angles. The vertical green dashed line indicates the mean value for the angle between the minor axis of the burst and a line joining its centre to (0,0). A peak near 0° indicates a preference for bursts to be oriented perpendicular to the radial direction from disk centre. Observations of bursts in the solar wind support this suggestion (Anantharamaiah et al., 1994; Sasikumar Raja et al., 2016). Large errors in the burst position angle for three bursts (Table 6.1) can account for the outliers $< -80°$.

Table 6.1: Table of fitted burst parameters for each of the 29 bursts described in Section 6.3 fitted with a 2D Gaussian in visibility space. The units in each column are given in brackets. Here I_0 is the maximum intensity of the burst, x_0 and y_0 are the x and y helioprojective coordinates of the burst, $\mathrm{FWHM_x}$ and $\mathrm{FWHM_y}$ are the burst sizes along the minor and major axes and θ is the position angle of the fitted Gaussian. Here I note that the position angle of the source is almost never 0. No predictions about the position angle of the source have been made from scattering models.

Burst Time 2019-04	I_0 (Jy)	x_0 (arcsec)	y_0 (arcsec)	$\mathrm{FWHM_x}$ (arcmin)	$\mathrm{FWHM_y}$ (arcmin)	θ (deg)
05T12:08:08	$90\,300 \pm 1310$	-1773 ± 6	214 ± 8	8.8 ± 0.3	17.6 ± 0.6	-27 ± 2
07T12:02:29	$83\,800 \pm 678$	-1924 ± 3	412 ± 4	10.3 ± 0.2	14.5 ± 0.4	-55 ± 2
07T12:04:22	$108\,000 \pm 1110$	-1990 ± 5	372 ± 5	11.3 ± 0.3	14.5 ± 0.5	-67 ± 3
07T12:15:08	$160\,000 \pm 1100$	-1677 ± 3	1229 ± 4	12.5 ± 0.2	15.6 ± 0.3	-44 ± 2
07T12:31:00	$120\,000 \pm 1010$	-1897 ± 4	165 ± 4	10.0 ± 0.2	14.0 ± 0.4	-56 ± 2
07T12:51:39	$47\,900 \pm 505$	-1979 ± 5	420 ± 5	12.2 ± 0.3	14.7 ± 0.5	-67 ± 4
08T12:00:16	$117\,000 \pm 1770$	-1310 ± 7	1021 ± 7	11.2 ± 0.6	16.9 ± 1.4	-64 ± 78
08T12:06:41	$316\,000 \pm 3380$	-1580 ± 6	819 ± 6	13.1 ± 0.3	18.7 ± 0.5	-66 ± 2
08T12:08:37	$60\,700 \pm 442$	-1617 ± 3	841 ± 4	11.3 ± 0.2	14.3 ± 0.3	-50 ± 3
08T12:22:34	$171\,000 \pm 1530$	-1381 ± 5	643 ± 5	13.6 ± 0.2	18.4 ± 0.4	-61 ± 2
08T12:26:54	$111\,000 \pm 800$	-1479 ± 4	339 ± 4	11.9 ± 0.2	18.7 ± 0.3	-58 ± 1
08T12:29:00	$77\,400 \pm 862$	-1341 ± 6	534 ± 6	13.3 ± 0.3	18.7 ± 0.6	-59 ± 1
08T12:34:57	$177\,000 \pm 1900$	-935 ± 5	947 ± 5	12.1 ± 0.3	17.2 ± 0.5	-72 ± 2
08T12:35:35	$278\,000 \pm 4130$	-903 ± 8	931 ± 8	12.4 ± 0.4	18.5 ± 0.7	-62 ± 3
08T12:43:00	$120\,000 \pm 1180$	-1653 ± 5	878 ± 5	12.4 ± 0.3	16.2 ± 0.5	-60 ± 1
08T12:47:07	$160\,000 \pm 1500$	-1382 ± 5	723 ± 5	13.6 ± 0.3	18.2 ± 0.5	-62 ± 2
08T12:48:49	$300\,000 \pm 2630$	-1305 ± 4	648 ± 5	12.8 ± 0.2	17.0 ± 0.4	-62 ± 2
08T12:50:27	$130\,000 \pm 2080$	-1332 ± 9	924 ± 9	13.6 ± 0.5	19.6 ± 0.8	-90 ± 88
08T12:54:35	$207\,000 \pm 1370$	-1485 ± 4	898 ± 4	13.6 ± 0.2	17.9 ± 0.3	-72 ± 2
08T12:59:25	$177\,000 \pm 1380$	-1473 ± 4	769 ± 4	12.9 ± 0.2	15.5 ± 0.4	-66 ± 3
11T12:56:27	$216\,000 \pm 1510$	-1222 ± 3	-106 ± 4	13.3 ± 0.2	17.2 ± 0.3	0 ± 2
12T12:00:18	$180\,000 \pm 2350$	-363 ± 6	501 ± 6	11.4 ± 0.4	14.8 ± 0.6	-87 ± 2
12T12:04:55	$131\,000 \pm 1550$	3 ± 6	400 ± 6	12.3 ± 0.3	17.9 ± 0.6	-102 ± 2
12T12:14:51	$43\,300 \pm 549$	-1439 ± 6	-549 ± 6	12.0 ± 0.4	16.1 ± 0.6	-83 ± 3
12T12:39:32	$86\,000 \pm 918$	-1040 ± 5	-147 ± 5	11.0 ± 0.3	15.7 ± 0.5	-91 ± 1
12T12:49:34	$74\,800 \pm 855$	-889 ± 5	-202 ± 6	12.6 ± 0.3	15.8 ± 0.5	-80 ± 4
12T12:51:54	$133\,000 \pm 1340$	-805 ± 5	-338 ± 5	11.7 ± 0.3	16.1 ± 0.5	-82 ± 3
12T12:53:51	$128\,000 \pm 1000$	-688 ± 4	-436 ± 4	10.3 ± 0.2	14.6 ± 0.4	-83 ± 2
13T12:30:31	$101\,000 \pm 1210$	-162 ± 4	-766 ± 5	7.2 ± 0.4	9.0 ± 0.7	-76 ± 84

6.5 Discussion

The observed source sizes of type III bursts are largely consistent with previous observations at similar frequencies in both interferometric and tied-array observations (Kontar et al., 2017; Zhang et al., 2020). In particular, the mean of the size in the major and minor axes is in agreement a previous measurement using the visibility fitting method (Murphy et al., 2021). As well as this, all 29 of the fitted bursts have an aspect ratio (defined above) of less than 1, which is indicative of elongation due to scattering in a particular direction (Anantharamaiah et al., 1994; Bastian, 1994). The peaked distribution of relative angles in Figure 6.7c is further evidence for alignment along a preferred direction. If this direction were radial, one would expect a peak around 0° however here a mean value of $-18.33°$ is observed. An examination of the magnetic field structure of the active region shows that some bursts are oriented such that their major axis is quasi-perpendicular to an open magnetic field line. These field lines are not necessarily radial with respect to the disk centre. Figure 6.8a shows a good example of the previous statement. The burst, shown in blue contours, intersects with open magnetic field line, shown in yellow at a quasi-perpendicular angle. This is in agreement to observations of bursts in the solar wind (Anantharamaiah et al., 1994; Sasikumar Raja et al., 2016). The assumption that the radio bursts are generated in open field lines above AR 12738 is only true for some of the bursts observed. There are a number of bursts that do not appear to be associated with the active region e.g. the burst in Figure 6.8b. It is possible that such bursts originated behind the limb however given the limitations of PFSS extrapolations it is uncertain whether this is the case.

There is one major deviation between the model of scattering through anisotropic density fluctuations in a spherically symmetric corona and these results. Kontar et al. (2019) predict that, for a point source, the aspect ratio of a radio burst should decrease with increasing heliographic longitude, i.e. distance away from the disk centre along the solar equator. However, as shown in Figure 6.6, no such trend is evident. There are a number of reasons why this may not be the case. Firstly, it is possible that calibration

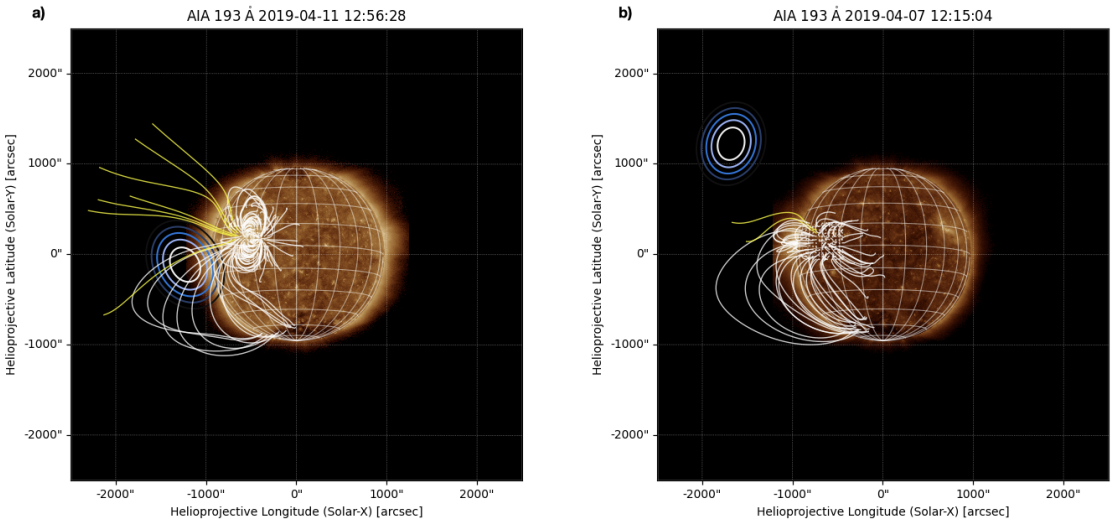

Figure 6.8: Overlay of burst location with PFSS from active region 12738. The background image is an AIA 193 Å image of the Sun at the time indicated in the title. Blue contours are the intensity of the radio burst from 50% of the max value to 100% in steps of 10%. Open field lines are shown in yellow, white lines are closed field lines. Panel a shows the type III burst is oriented quasi-perpendicular to an open field line from AR 12738. Panel b shows a type III burst that is not associated with any open field lines from the PFSS and may have originated behind the limb.

of the data did not fully converge or that the observation itself was corrupted. I believe this to be unlikely firstly because the Gaussian fit to each of the 29 bursts was manually inspected and any such flaw would be apparent. Secondly, the position and orientation of the bursts with respect to the magnetic field lines of AR 12738 agrees with the theory that type III bursts are generated along open magnetic field lines (Wild, 1950b,a) and are oriented with their major axis perpendicular to the field line (Anantharamaiah et al., 1994). Assuming the observation and data analysis are free from error, the simplest answer to why this is the case is mentioned in the discussion of Kontar et al. (2019). They argue that the total observed size can be considered as the intrinsic size of a burst and the size due to scattering of a point source added in quadrature $\mathrm{FWHM}_{\mathrm{total}} = (\mathrm{FWHM}^2{}_{\mathrm{intrinsic}} + \mathrm{FWHM}^2{}_{\mathrm{scattering}})^{1/2}$. Therefore, no trend in source sizes could suggest that type III bursts have an intrinsic size that is greater than the size due to scattering.

An alternative explanation could be that the level of r.m.s fluctuations and anisotropy are different to what Kontar et al. (2019) suggest. The parameter space for the scat-

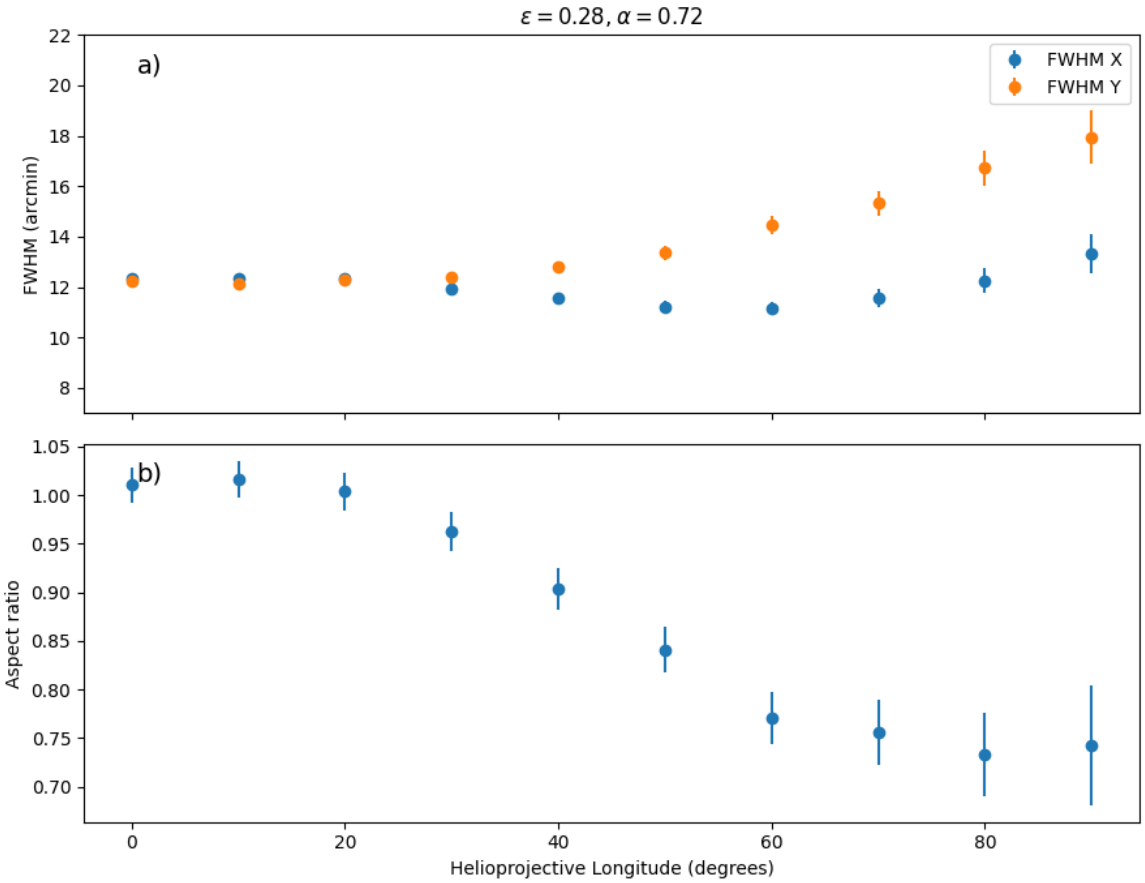

Figure 6.9: Results from the anisotropic scattering model from Kontar et al. (2019) using the Python implementation by Zhang et al. (2021). 50,000 photons were emitted from a radio point source with a frequency of ~ 30.6 MHz. The size of the radio burst at a number of helioprojective longitudes was determined by tracing the photons to a point where scattering is negligible and then back-projected to form an apparent source intensity map $I(x, y)$ the centroid and FWHM of this map are found using Equations 6.6, 6.7, 6.8. Panels a and b correspond to panels a and c in Figure 6.6 respectively, although here the x axis is heliographic longitude. The model was run with $\varepsilon = 0.28$ and $\alpha = 0.72$.

tering model was explored by Zhang et al. (2021) who found that in order to match the observed decay time and size of a radio burst at 35 MHz, a value for r.m.s fluctuations of $\varepsilon = 0.28$ and an anisotropy factor of $\alpha = 0.72$ were necessary. The anisotropic scattering model from Kontar et al. (2019) was run using the Python implementation by Zhang et al. (2021). 50,000 photons were emitted from a radio point source with a frequency of ~ 30.6 MHz. As was discussed in Section 6.1, the photons are tracked until they cross a point where scattering becomes negligible or 1 AU, whichever is less. From here they are back-projected to form an apparent source intensity map $I(x, y)$. The source location and size is found from the normalised moments of the intensity map, i.e.

$$\bar{x} = \frac{\int_{-\infty}^{\infty} xI(x,y)dxdy}{\int_{-\infty}^{\infty} I(x,y)dxdy}, \quad \bar{y} = \frac{\int_{-\infty}^{\infty} yI(x,y)dxdy}{\int_{-\infty}^{\infty} I(x,y)dxdy} \tag{6.6}$$

$$\begin{aligned} \sigma_x^2 &= \frac{\int_{-\infty}^{\infty} (x-\bar{x})^2 I(x,y)dxdy}{\int_{-\infty}^{\infty} I(x,y)dxdy}, \\ \sigma_y^2 &= \frac{\int_{-\infty}^{\infty} (y-\bar{y})^2 I(x,y)dxdy}{\int_{-\infty}^{\infty} I(x,y)dxdy} \end{aligned} \tag{6.7}$$

$$\mathrm{FWHM}_{x,y} = 2\sqrt{2\ln 2}\sigma_{x,y}. \tag{6.8}$$

Figure 6.9 shows the result of modelling a radio burst at different heliographic longitudes with the parameters suggested by Zhang et al. (2021). It is immediately obvious that the modelling result does not match what is observed in the left column of Figure 6.6. It also shows the opposite of Figure 8 in Kontar et al. (2019) whereby $\mathrm{FWHM_x}$ remains roughly constant while $\mathrm{FWHM_y}$ is seen to increase with increasing heliographic longitude. The expected trend towards smaller aspect ratios with increased heliographic longitude remains.

Can the absence of a relation between source aspect ratio and position be explained if type III bursts have an intrinsic size? Following the extension of the total source size being the size of the intrinsic source and size due to scattering added in quadrature can give an estimate as to how big a source must be before it isn't affected by scattering. Assuming a size of due to scattering of $\mathrm{FWHM_{scattering}} = 12$ arcmin, which is consistent

with modelling results shown in Figure 6.9, for the total source size to mostly consist of the intrinsic size, i.e. $\mathrm{FWHM_{total}} = 1.5\mathrm{FWHM_{intrinsic}}$, a type III burst would need an intrinsic size of ~ 10.73 arcmin. This results in a total observed size of $\mathrm{FWHM_{total}} = 16.1$ arcmin, similar to the mean value obtained for $\mathrm{FWHM_y}$ in this work.

The latitudinal variation of source size and aspect ratio has not yet been investigated with scattering models. The main effect of change in latitude is tentatively shown in panel c of Figure 6.7 which suggests that the the source will always be oriented such that the major axis is almost perpendicular to the radial direction from the solar centre.

The modelling in this analysis was performed under the assumption that ε and α do not change with time or position in the solar corona. Neither of these assumptions is necessarily true. Considering that burst orientation is strongly related to the local magnetic field line direction, it is possible that there is spatial variability in these measures of coronal turbulence. To investigate any possible temporal variance of ε and α, the FHWM size in the helioprojective-cartesian x and y direction are plotted with respect to time in Figure 6.10. Over the course of an hour the FWHM size of the burst varies by ~ 5 arcmin while the biggest difference in source size over the entire observation is ~ 8 arcmin and ~ 11 arcmin for $\mathrm{FWHM_x}$ and $\mathrm{FWHM_y}$ respectively. If the observed source size were *only* due to scattering then any change may be indicative of temporal variability in either ε, α or both.

6.6 Conclusion

Observations of the position and size of 29 type III radio bursts do not fully agree with results from models of radio wave scattering in the solar corona. After thorough inspection of interferometric calibration and fits to interferometric visibilites, I attribute this discrepancy to an intrinsic source size of type III bursts. Work needs to be undertaken to improve the calibration procedure for solar radio bursts so that the initial sample of ~ 300 bursts can be analysed. The scattering model used in this analysis assumes a spherically symmetric, unmagnetised, corona (Kontar et al., 2019; Zhang et al., 2021).

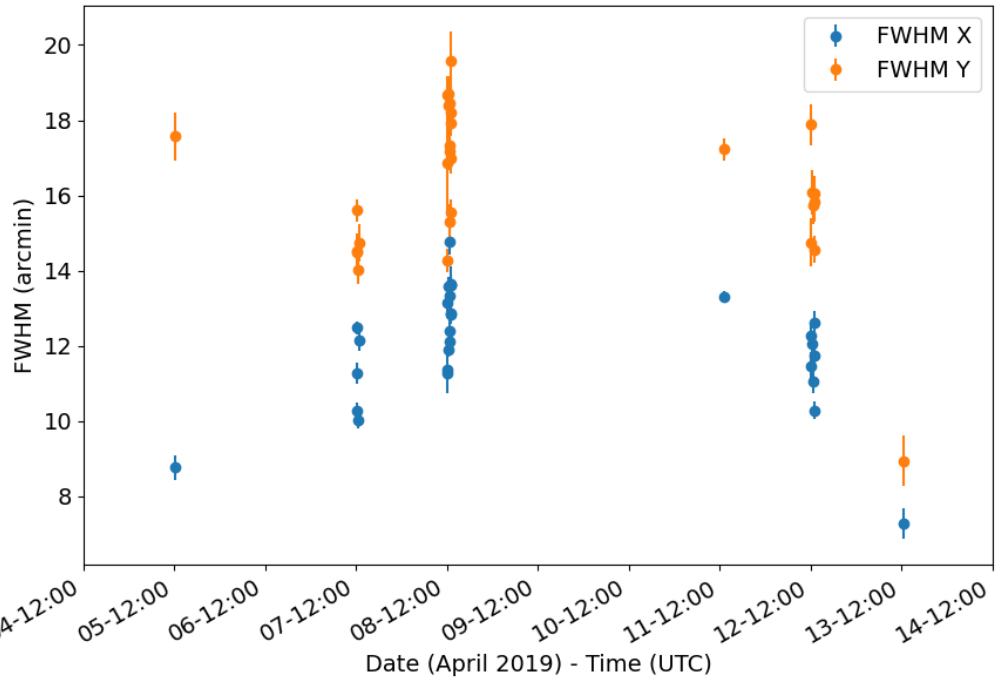

Figure 6.10: Plot of FWHM size of radio bursts with respect to time. The x axis shows the date and time while the y axis denotes the FWHM in the major (orange) and minor (blue) direction in arcmins. There is a spread of sizes in both $\mathrm{FWHM_x}$ (blue) and $\mathrm{FWHM_y}$ (orange) of the order of ~ 5 arcmin over the course of an hour which could be interpreted as temporal variance of ε or α on timescales of minutes.

Most of the bursts in this analysis are seen to be located above the active region AR 12738 which has a much greater electron density and magnetic field strength than the quiet corona. Thus, changes to the electron density model and including the effects of magnetic fields may be necessary to explain the difference between observations and the results from scattering models.

Before one can use observations of radio bursts to determine the physical parameters of coronal plasma and the radio wave scattering process, the discrepancies between the results presented here and previous modelling work must be addressed. Improvements to interferometric calibration techniques and including the effects of magnetic fields and active regions in scattering models are the two most prominent issues in this regard.

In this chapter I outlined the development of scattering models for radio waves in the solar corona from seminal works to modern day advancements. I also stated the importance of comparisons between these models and contemporary observations. I then detailed the observation of hundreds of type III radio bursts during a radio noise storm over the period 04 April 2019 to 14 April 2019. Using LOFAR interferometric visibilities at ~ 30 MHz and a method similar to Murphy et al. (2021), I fitted 29 of the calibrated bursts to determine their size and shape. I found that type III radio bursts have a mean size in the minor and major axis of 11.96 arcmin for and 16.27 arcmin respectively and a mean aspect ratio of 0.74. No trend in aspect ratio with respect to burst location was evident in the observations and as such, I attributed this to the intrinsic size of type III radio bursts being greater than the size due to scattering. The relative angle between the minor axis of each burst and a radial line from the centre of the Sun to its centre has a mean value of $-18.33°$ and indicates preferential orientation. The magnetic field was modelled using a PFSS model and the source orientation was found to be perpendicular to open magnetic field lines for some of the bursts. Using the mean values achieved as a typical intrinsic size agrees well with previous observations with LOFAR in both interferometric and tied-array images at similar frequencies. This work is *in prep* for submission to *Astronomy and Astrophysics*.

7

Future Work and Conclusions

The principal goals of this thesis were to observe solar radio emission at the highest temporal, spectral and spatial resolutions to date. Firstly, the REAL-time Transient Acquisition backend (REALTA) was developed and installed at I-LOFAR to record the raw voltages from the station at 5.12μs temporal resolution. This work was published in *Astronomy and Astrophysics* as Murphy et al. (2021) Secondly, a new technique was implemented for the first time to directly measure the size of radio bursts from their interferometric visibilities. This work was presented in Chapter 5 and was published in *Astronomy and Astrophysics* as Murphy et al. (2021). This technique was utilised to determine the size and shape of 29 type III bursts that were compared with predictions from state-of-the-art scattering simulations. In this chapter I highlight some future work that could be built upon the research presented in this thesis to further advance the knowledge of radio wave generation and propagation in the solar corona. I discuss the possibility of observing radio bursts with 5 ns temporal resolution using the Transient Buffer Boards (TBBs) from I-LOFAR. Next I consider the use of machine learning algorithms to automatically detect and classify solar radio bursts recorded with I-LOFAR and REALTA. I then discuss the necessity for the development of a calibration and imaging pipeline for solar interferometry. I also outline further work that is necessary to bridge the gap between modern observations and computer simulations. This is underscored by the need for a statistical analysis of type III and type IIIb radio bursts, particular in the context of the most recent theories of spectral fine structure generation due to Langmuir wave modulation. Finally, I draw this thesis to a close with some concluding remarks.

7.1 Primary Scientific Objectives

The research that has been presented in this thesis has contributed to our knowledge of solar radio emission at low frequencies. The extent to which radio wave propagation

effects distort the original shape of a radio burst has been explored. Work undertaken during this thesis has also resulted in a new facility to record and analyse radio emission using I-LOFAR. REALTA can be used to record radio observations at 5.12 μs temporal resolution. A new technique for measuring burst sizes from complex visibility data was also developed over the course of this work. Below I summarise the results from this thesis.

7.1.1 Observing Radio Bursts at the Highest Temporal Resolutions.

The first objective of this thesis was to record the high time resolution, raw voltages from I-LOFAR to observe solar radio bursts. In order to do this, a dedicated backend to record, store and analyse the data was necessary. Chapter 4 outlines the development of the REALtime Transient Acquisition backend (REALTA) to serve this purpose. The seven node computer cluster receives data from I-LOFAR along a 10 Gbps fibre optic cable in four data "lanes". After data has been recorded to disk, one of a number of processing pipelines can be run including those for solar radio observations, pulsars, FRBs, RRATs, Jovian emission and SETI. Some of the first solar radio bursts observed with I-LOFAR and REALTA are shown in Chapter 4. REALTA allows for high temporal resolution observations of short duration solar radio bursts such as S-bursts and can be used to analyse short duration pulsations in radio bursts. Information gained from such observations can be used to remotely determine the physics of the solar corona (Morosan et al., 2015; Clarke et al., 2019) and can give insight into magnetohydrodynamic oscillations in the corona (Carley et al., 2019). This work was published in *Astronomy and Astrophysics* as Murphy et al. (2021). Some other first results from REALTA are given below.

7.1.1.1 Pulsars

International LOFAR stations are ideal instruments to observe radio pulsars, particularly at frequencies between 100 MHz and 200 MHz (Stappers et al., 2011; Bilous et al., 2014; Noutsos et al., 2015). Furthermore, the large fractional bandwidth of an international LOFAR station can offer new insight to the spectral variability of giant pulses from the Crab Nebula. Many international stations regularly participate in pulsar studies (for example, Mereghetti et al., 2016; Bondonneau et al., 2017; Hermsen et al., 2018; Donner et al., 2019), while pulsar observations with LOFAR core stations (for example, Bilous et al., 2014, 2020) are also common. Recent observations with the Polish international stations include those by Blaszkiewicz et al. (2020).

To date, over 50 different pulsars have been observed with I-LOFAR using REALTA. Figure 7.1 shows a sample of 19 pulsars which were observed, each for 6 minutes, on the 4th and 5th of March 2020, processed using the methods discussed in section 4.3.3. In addition, as a result of regular timing campaigns of these sources, a number of targets have been studied in more depth, the Crab Nebula being the prime example. While the recording and timing of folded profiles of the Crab pulsar are of interest for studying the interior structure of the neutron star via its glitches (Lyne et al., 2015) and variability due to scattering and echo events, it also frequently emits so-called 'giant pulses' (Meyers et al., 2017). These giant pulses have fluences that vary from hundreds of Jy ms to tens of thousands of Jy ms. These pulses can be studied to analyse their scintillation, scattering, and brightness distributions.

One such example of these giant pulses can be seen in an observation taken of the Crab pulsar with I-LOFAR on 30 June 2020. The observation was processed using the previously described methodology (section 4.3.2, section 4.3.3) on REALTA and a short segment of the observation is shown in Figure 7.2. The figure is made from Stokes I data, where each channel has a bandwidth of 24 kHz and an underlying time resolution of 40.96 μs (though it has been averaged using a median filter for this plot). There were $\sim$ 1300 giant pulse candidates detected in the 30 minute observation. Using a rate of

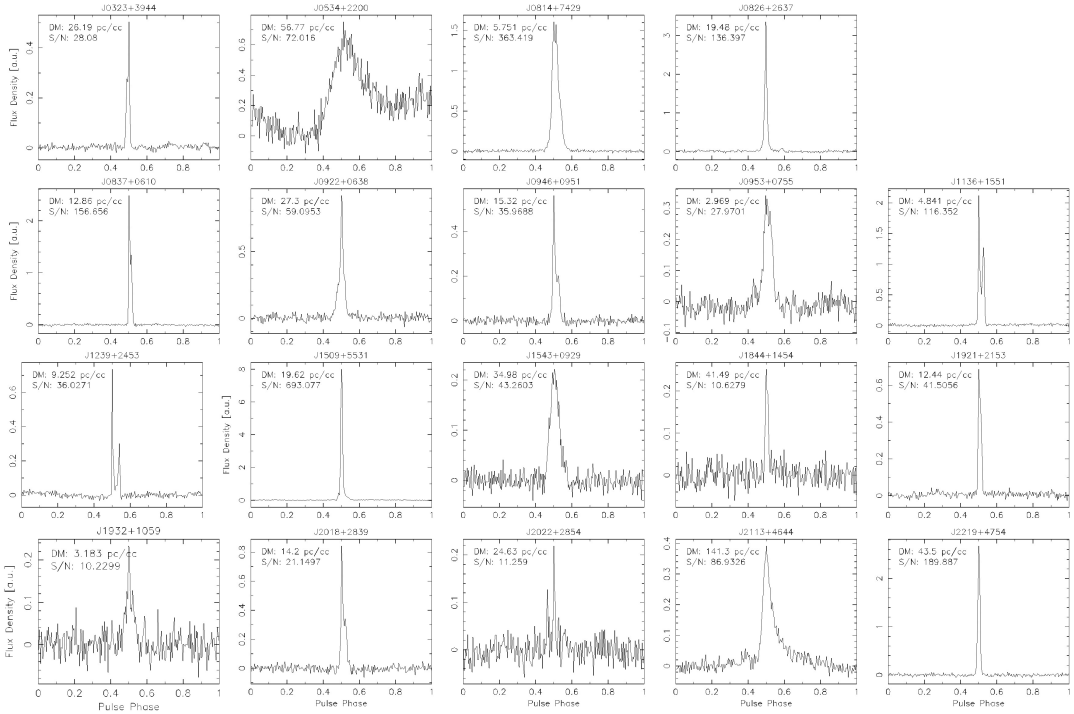

Figure 7.1: Sample of 19 pulsars observed with I-LOFAR and REALTA. Each of these observations is 6 minutes in duration and were taken on 4–5 March 2020 using the HBA antennas (110 MHz to 190 MHz). The data were processed using the method described in section 4.3.3 and plotted using `PSRCHIVE`. The x-axis in each plot is the pulse phase in radians, while the y-axis is flux density in arbitrary units.

~ 0.7 giant pulses per second, we determine there are ~ 20 giant pulses visible in the dynamic spectrum in the left panel of Figure 7.2. Other structure in the left panel of Figure 7.2 includes some ionospheric scintillation and RFI. This time segment is mostly of interest due to one rare, extremely bright, giant pulse, which is re-plotted in the right panel of Figure 7.2 where it has been corrected for dispersion effects. Initial analysis using the radiometer equation indicates a specific fluence of ~ 200 kJy ms across the observed bandwidth which may be the brightest pulse ever observed for this pulsar at these frequencies (Karuppusamy et al., 2012; Meyers et al., 2017; Van Leeuwen et al., 2020).

As of May 2021, over 80 hours of observations of the Crab pulsar have been captured by REALTA. Initial analysis of this data set, focusing on a four hour observation from March of 2020, has been performed and gives results that are similar to that of other low-frequency instruments. The giant pulses were found to form a fluence distribution with a power-law fit of $\alpha = -2.86 \pm 0.07$, similar to that of other low fre-

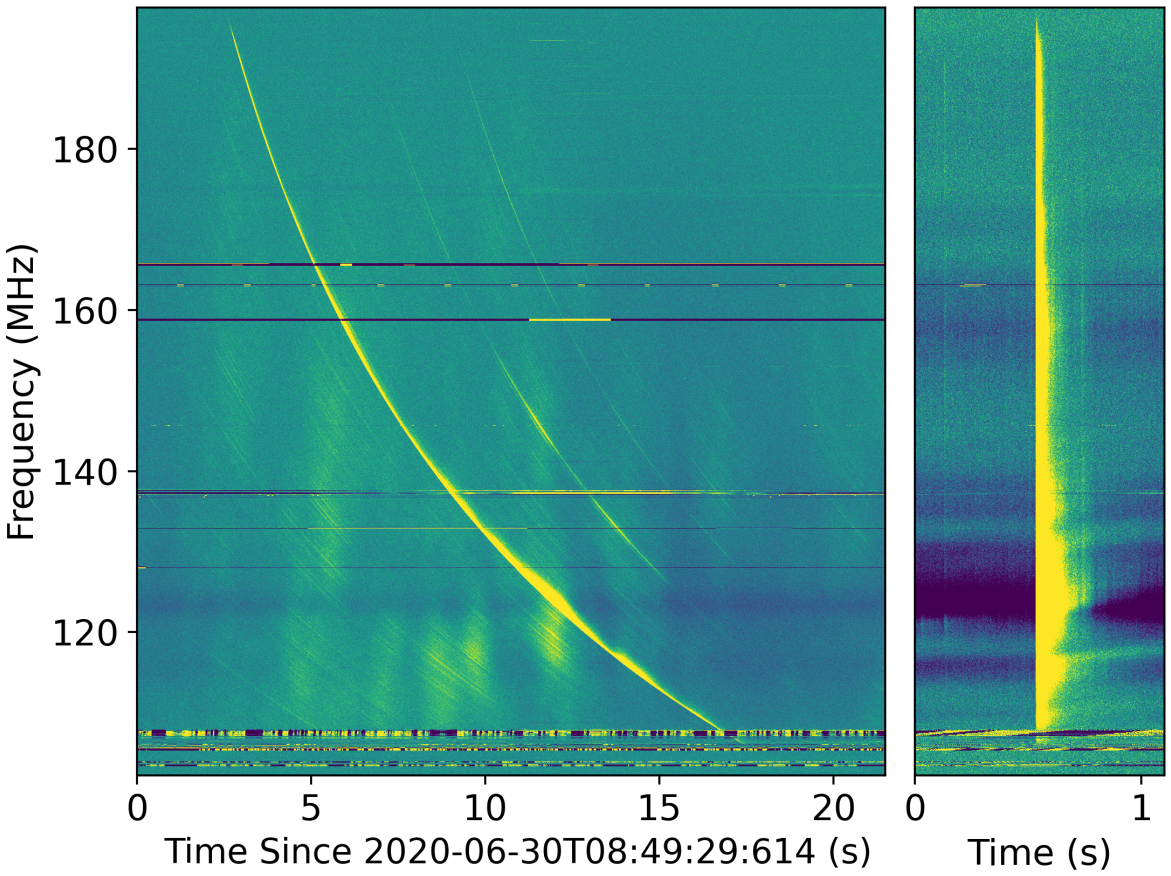

Figure 7.2: Observation of the Crab Pulsar performed on 30 June 2020, (left) without incoherent dedispersion and (right) with incoherent dedispersion. The plot on the left contains several giant pulses and both temporally- and spectrally-variable ionospheric scintillation. The plot on the right focuses on the brightest pulse in the group, which is the brightest pulse observed from the Crab Pulsar with I–LOFAR to date. Here data were processed to channel bandwidths of 24 kHz, resulting in a sampling rate of 40.96μs. The data were time integrated to a temporal resolution of 1.31 ms prior to plotting.

quency instruments (Meyers et al., 2017), but steeper than the results at Jodrell Bank (Mickaliger et al., 2017). Similarly, an initial investigation of the spectral behaviour of the scattering timescale of the brightest pulses appeared to follow a power law of $\alpha = -3.7 \pm 0.5$, in agreement with other instruments (Driessen et al., 2019). Future work includes planning to integrate a CLEAN-based de-convolution (see Bhat et al., 2003) of the pulse shapes to better describe the scattering and dispersion measure variations of single pulses over time, the effects of which are entangled (McKee et al., 2018), especially at lower frequencies.

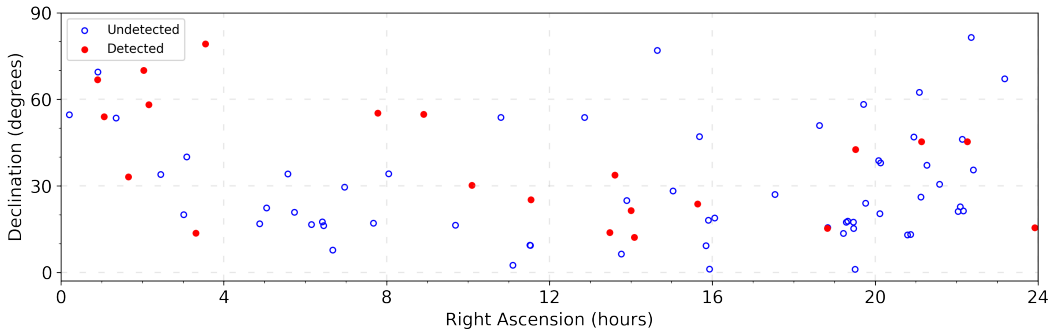

Figure 7.3: Overview of the sky positions of the RRATs observed during the census discussed in section 7.1.1.2 as of May 2021. Filled red dots indicate sources that have been observed and detected with either single pulses or periodic emission while blue circles indicate sources that were observed but not detected in I-LOFAR data.

7.1.1.2 Rotating radio transients

Rotating radio transients (RRATs) are a class of neutron star that were discovered through detecting single, bright pulses rather than via periodicity searches. If a sufficient number of pulses is detected within a short observing window, it is possible to determine the underlying period of the neutron star through brute force methods, after which the times of arrival of these pulses can be used to time the sources like any other pulsar (Keane et al., 2011). While the LOFAR core has blindly detected several RRATs during the LOFAR Tied Array All Sky survey (LOTAAS Sanidas et al., 2019; Michilli et al., 2020; Tan et al., 2020), and through targeted follow-up observations of sources detected with the Green Bank Telescope (Karako-Argaman et al., 2015), there has not been a major undertaking to time these sources with the LOFAR instruments, using the core or international stations. However, the full-sky sensitivity and fractional bandwidth of a single international LOFAR station makes it the perfect candidate to perform follow-up observations of some of the brighter RRAT candidates identified by all-sky monitoring instruments such as the Big Scanning Array of Lebedev Physical Institute (BSA LPI) and the Canadian Hydrogen Intensity Mapping Experiment (CHIME; Amiri et al., 2018). Follow-up observations of these candidates are useful to (a) determine the rotational characteristics of the stars through phase-coherent follow-up timing; and to (b) perform source characterisation from examining stars with broad spectral coverage.

Between July 2020 and May 2021, a 500 hour observing campaign has been undertaken to observe a diverse set of RRATs from the RRatalog[1], the CHIME-FRB Galactic sources database[2], and the BSA LPI Transients Catalogue[3], with a focus on sources that as yet do not have well defined periods. An overview of the sources observed and detected by this census can be seen in Figure 7.3. This campaign has so far resulted in the discovery of rotation periods for two sources which were previously unknown, periodic detection of a further two sources that have not been previously detected at LOFAR frequencies and the determination of coherent timing solutions for thirteen other sources. These results will be discussed in detail in a future paper (McKenna et al. in prep).

7.1.1.3 Fast radio bursts

Since their discovery in 2007 by Lorimer et al., fast radio bursts (FRBs) have been of keen interest to radio astronomers across the globe. While blind searches with multiple telescopes have helped push the lower bounds of their emission frequencies down year on year, the detection of numerous repeating FRBs by the CHIME-FRB collaboration (Andersen et al., 2019) has accelerated this process in recent months. Searches for FRBs with LOFAR include those by Karastergiou et al. (2015) and ter Veen et al. (2019), for example.

One particular repeating FRB, FRB 20180916B ('R3') has been found to have a period of 16.35 ± 0.15 days, with an activity window of 5 days (Amiri et al., 2020), and has been detected with the LOFAR core (Pastor-Marazuela et al., 2021; Pleunis et al., 2021). Prior to this, I-LOFAR and REALTA were used as a part of a 70 hour campaign to observe R3 during its activity phase and attempt to see emission at previously unseen frequencies. However, no significant pulse candidates were detected during this campaign. For further results and observations of other FRB sources see McKenna et al. (in prep).

[1] http://astro.phys.wvu.edu/rratalog/
[2] https://www.chime-frb.ca/galactic
[3] https://bsa-analytics.prao.ru/en/transients/rrat/

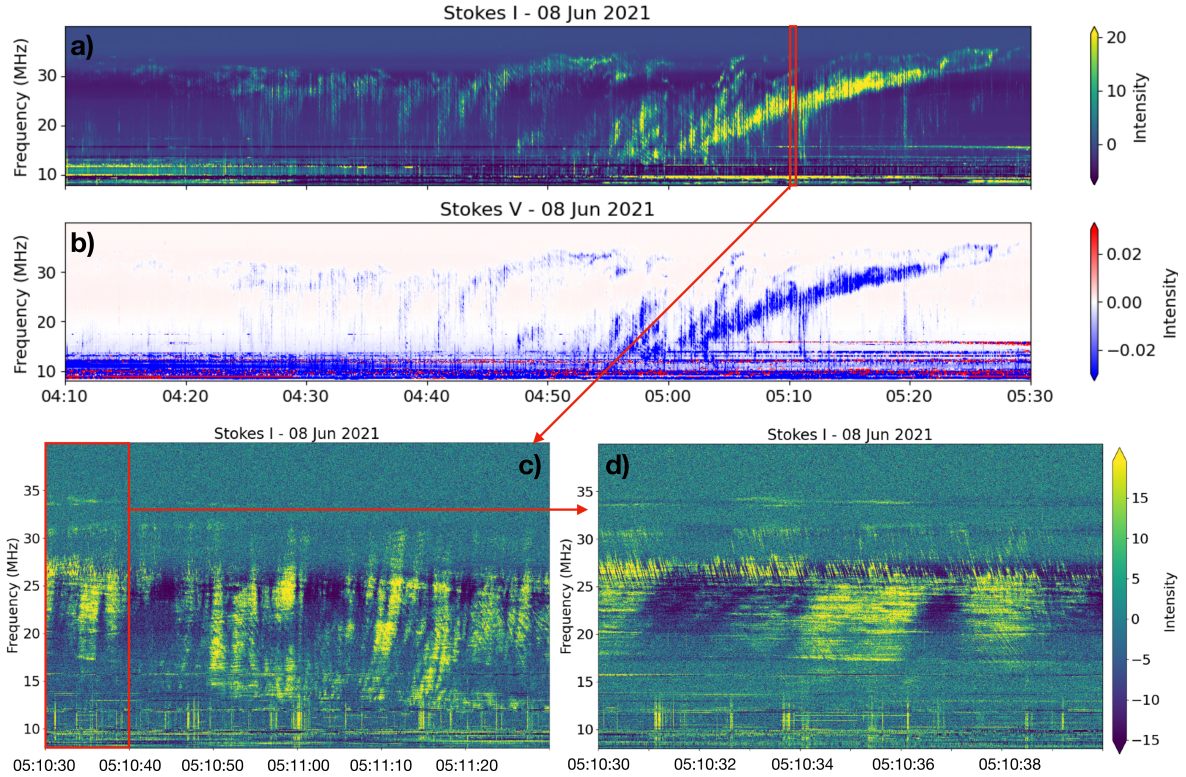

Figure 7.4: Observation of a Jovian Decametric emission produced by the Io-Jupiter interaction. Panel (a) shows Stokes I (in dB above background). Panel (b) displays Stokes V (in arbitrary units). The resolution is 84 ms per 12.2 kHz. The emission displays a strong negative value in Stokes V, which means a strong right-hand circular polarization. Panels (c) and (d) show respectively a 60 s and 10 s zoom-in of panel (a) (Stokes I), processed with the highest resolution available for this observation (81.92 μs per 12.2 kHz). Millisecond drifting bursts are visible panel (d).

7.1.1.4 Jovian auroral radio emission

Decametric radio emission (DAM), the strongest component of Jovian auroral radiation, was discovered in 1955 by Burke & Franklin (1955), with part of this emission controlled by the Io-Jupiter interaction (Bigg, 1964). The source of this radio emission is known to be due to the electron cyclotron maser instability (ECMI) in the Jovian magnetosphere, which occurs when a circularly polarised wave resonates with the gyration of electrons with relativistic energies (Wu & Lee, 1979; Wu, 1985; Zarka, 1998; Treumann, 2006; Louarn et al., 2017). The ECMI amplifies the wave on the extraordinary R-X mode which can escape the source and propagate in free space as a radio wave, at a frequency very close to the local electron cyclotron frequency, which is proportional to the local magnetic field amplitude. Jovian DAM emissions are the only

planetary radio emissions visible from the ground, since part of the DAM is emitted at a frequency above the ionospheric cutoff frequency ($\gtrsim$ 10 MHz). BF observations of Jovian DAM using the LOFAR core stations have been used to test the sensitivity of LOFAR to exoplanetary radio emissions (Turner et al., 2019, 2021).

On 8 June 2021, I-LOFAR observed Jovian DAM emission produced by the Io-Jupiter interaction, from 04:10 to 05:30 UTC. The Stokes I and V data from this observation are shown in Figure 7.4a-b. An arc shape emission with a high intensity is observed between $\sim$ 04:55 and 05:30 (corresponding to the main Io-DAM emission), preceded by emissions with lower intensity starting at $\sim$ 04:10 (corresponding to secondary Io-emissions). Looking at both the shape of the emission and its polarization (strong negative Stokes V value, corresponding to a right-handed circular polarization), we can determine that this emission is an Io-B emission (coming from the north-dawn side of Jupiter, see Marques et al., 2017, for example).

Moreover, we have with I-LOFAR access to very high temporal and frequency resolution, of which an example is shown Figure 7.4c,d (81.92 μs per 12.2 kHz). This will allow us to study the microphysics of the Jovian decametric emissions, for example the millisecond bursts visible Figure 7.4d with a drifting feature in frequency with time ($\sim$ 25-30 MHz). These millisecond drifts are thought to be electron bunches propagating along the magnetic field lines and can reveal both the energy of the resonant electrons as well as the potential drops (if present) along these fields lines (Hess et al., 2007, 2009). The high-resolution capability will also enable constraints to be placed on the position and movement of the sources, by interferometric measurements with several LOFAR stations, as well as the characteristics of the emission (for example, thickness and opening of the emission beam). Finally, I-LOFAR, combined with REALTA, is equipped to join the other LOFAR stations in the ground radio observation campaigns in support of the Jupiter space missions, both current (Juno[1]) and future (JUICE, Europa-clipper).

[1]Such as the Juno Ground Radio Observation Support https://maser.lesia.obspm.fr/task-1-data-collections/juno-ground-radio/

7.1.1.5 SETI

International LOFAR stations such as I-LOFAR have very broad fields of view, particularly at frequencies less than 150 MHz (van Haarlem et al., 2013). This, coupled with the ability to channelise data to bandwidths $\lesssim 1$ Hz, are favourable characteristics in SETI research. BL is conducting one of the most sensitive, comprehensive, and intensive searches for technosignatures on other worlds across a large fraction of the electromagnetic spectrum (Worden et al., 2017). Targets of the BL program include one million nearby stars, one hundred nearby galaxies, the entire Galactic plane, and exotic astrophysical objects (see Isaacson et al., 2017, for detail). Gajjar et al. (2019) provides the current status of these observing campaigns, as well as listing a number of collaborative observing facilities that are working alongside BL for carrying out these sensitive studies. The BL program is collaborating with two of the international LOFAR stations: I-LOFAR and LOFAR-SE, which is located at Onsala (Sweden), to complement searches towards the above-mentioned BL targets at lower radio frequencies. Details of the dedicated hardware deployed at I-LOFAR is discussed in section 4.3.4. First-light observations were conducted with these BL nodes on 19 November 2020 towards PSR B1919+21 to validate the BL recording and conversion pipelines. Recently, we also conducted observations of PSR B2217+47 on 21 April 2021 using the BL nodes for further pipeline development. Baseband data in the GUPPI format were converted to two different temporal and spectral resolution total intensity `SIGPROC` formatted filterbank data products. PSR B2217+47 was clearly detected, by folding high-temporal products. To search for narrowband Doppler drifting signals, `SIGPROC` formatted filterbank files with 3 Hz spectral resolution were used. This made use of the BL narrowband signal search tool, `turboSETI` (Enriquez et al., 2017). Figure 7.5 shows an example of one of the narrowband signals of terrestrial origin detected using `turboSETI` towards PSR B2217+47. In the future, it is planned to conduct detailed on-target and off-target observations to discriminate such anthropogenic signals from true sky-bound ETI signals.

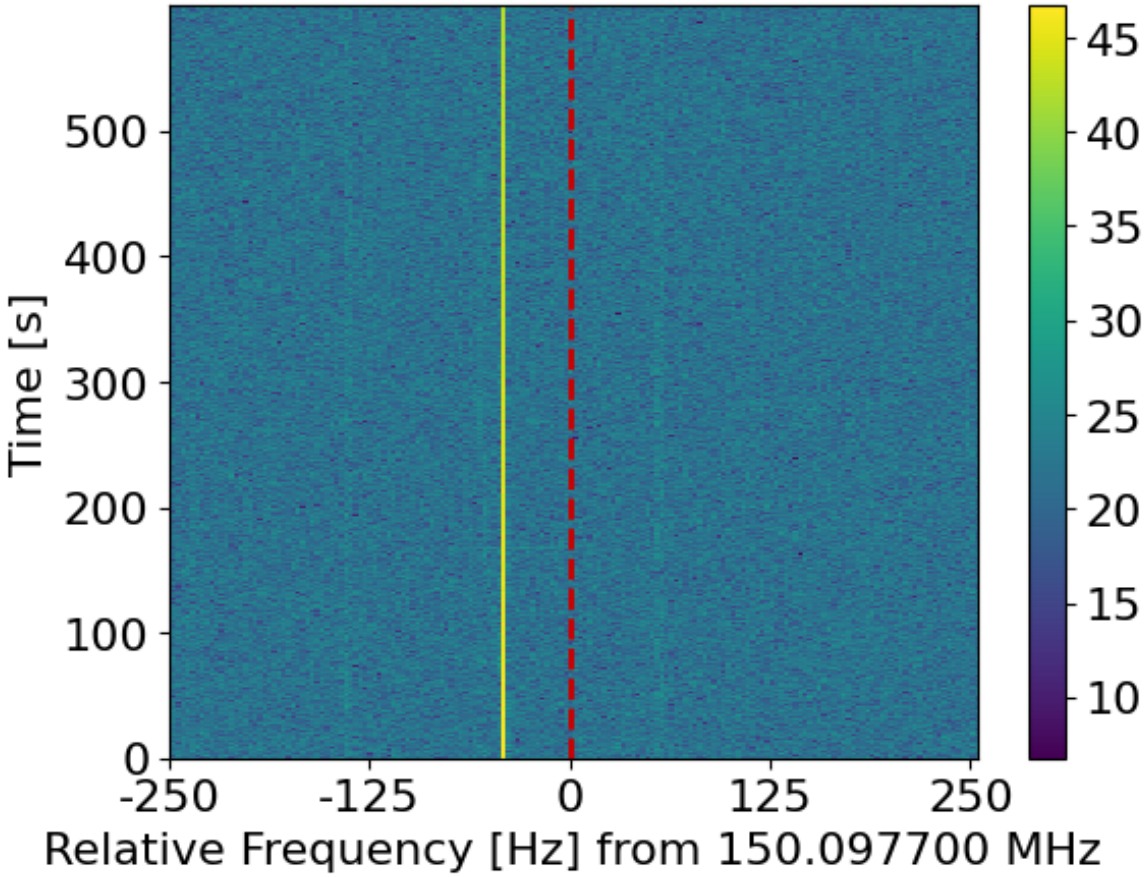

Figure 7.5: Narrowband signal detected using REALTA and the `turboSETI` algorithm. Dynamic spectra of an example narrowband signal detected in an observation pointing toward PSR B2217+47 using `turboSETI` with the BL nodes in REALTA. The colour bar shows intensity in arbitrary units while the red dotted line shows a relative frequency of 0 Hz from 150.0977 MHz. The signal does not show any drifting and thus likely has a terrestrial origin.

7.1.2 Observing Radio Bursts at the Highest Spatial Resolutions.

The second objective of this thesis was to determine if the size of previously observed type IIIb radio bursts was due to an effect of tied array imaging or radio wave scattering in the corona. This is important in determining whether or not the large source sizes of radio bursts have a physical origin or are simply due to a lack of spatial resolution. In Chapter 5 I described a new method for determining the size of a type IIIb burst directly from interferometric visibilities recorded with LOFAR. This method removes reduces the uncertainty of measured source sizes and removes any ambiguity from imaging deconvolution algorithms. This was utilised for the first time in the context of solar observations with LOFAR to determined the size of a type IIIb burst. For a burst at 34.76 MHz, the full width at half maximum height (FWHM) along the major and minor axes was found to be 18.8 arcmin $\pm$ 0.1 arcmin and 10.2 arcmin $\pm$ 0.1 arcmin respectively at a plane of sky heliocentric distance of 1.75 $R_{\odot}$. The expected size of a burst at this frequency, based on the relationship between the spectral width of the striation and spatial extent of emission, was calculated to be 3.18 arcsec. It is important to note that this source size is only an estimate of the vertical extent of the emitting region and as such the actual observed source may be larger due to projection effects. The discrepancy between these two values was investigated and the results suggest that the large size observed is due to radio wave scattering. One further implication of this work is that values of the relative root mean squared density fluctuations ε which are determined *only* from tied array observations of radio bursts run the risk of over estimating the true value as the effect of imaging on source size has not been fully investigated. This work was published in *Astronomy and Astrophysics* as Murphy et al. (2021).

7.1.3 Comparing Observations of Radio Bursts to Computational Simulations.

The final objective of this thesis was to determine if observations of scattered sources matched the predictions of computational simulations. This was achieved by comparing a number of observations of type III bursts to simulations of radio scattering in the solar corona. Using the new method for determining radio burst size from interferometric visibilities, the spatial properties of 29 type III radio bursts were found. The results of this analysis, comparing the similarities and discrepancies between the observations and computation scatting, are presented in Chapter 6.It was found that bursts did not show the change in aspect ratio with respect to heliocentric angle as would be expected following from Kontar et al. (2019). There are two possible explanations for this, the first being the level of anisotropy is lower than initially suggested by Kontar et al. (2019). This is supported by an investigation of the parameter space of the scattering simulations by Zhang et al. (2021). The other is that type III bursts have an intrinsic source size greater than the size of a point source due to scattering. This work favours the latter explanation although it is possible that both can be true. This work suggests that state-of-the-art scattering simulations still do not accurately describe all observed properties of type III radio bursts. In order to use observations of solar bursts at low radio frequencies to determine the turbulent nature of coronal plasma, these discrepancies must be rectified. This work is *in prep* for a scientific publication.

7.2 Future Work

The research outlined in this thesis has furthered our knowledge of the nature of electron density fluctuations in the solar corona. Direct visibility measurements of the source size of a type IIIb burst has confirmed that density fluctuations are the main cause of large source sizes in observations and not the imaging method used. The work in this thesis has also highlighted discrepancies between observations of type III bursts

and scattering simulations. Results from scattering simulations that use values of the relative root mean squared density fluctuations and degree of anisotropy in the power spectrum of fluctuations to match typical observations (e.g. Kontar et al., 2017) are not observed in a sample of 29 type III bursts. This work has produced a computationally and conceptually simple method to determine the size and position of a radio burst from its interferometric visibilities. Not only this but, the development of REALTA throughout this PhD allows for the recording of the raw complex voltages from I-LOFAR to study solar radio bursts. I address some open questions that remain and the possibility of future work which builds upon the research presented in this thesis below.

7.2.1 On the Future Development of REALTA

Here I have described the hardware for REALTA and given an overview of the software used to record and analyse data recorded from I-LOFAR. First observations of solar radio bursts were showcased, while the broad range of objects that I-LOFAR and REALTA can observe can be seen in Murphy et al. (2021).

LOFAR 2.0 is a series of hardware and software upgrades to the ILT, which will be implemented in a number of stages over the coming years. An upgrade to an international LOFAR station, such as I-LOFAR, will require new receiver units (RCU2), new station beamformers (Station Digital Processors) based on the Uniboard^2 architecture (Schoonderbeek et al., 2019) and new power, clock and control board for improved station control. The upgrade will greatly improve the instantaneous bandwidth, sensitivity and RFI rejection of an international station.

LOFAR for Space Weather (LOFAR4SW) [1] is a proposed upgrade to LOFAR, currently being designed to enable regular space weather monitoring. If completed, LOFAR4SW would allow near-real-time monitoring of space weather phenomena such as solar flares and coronal mass ejections, interplanetary scintillation and ionospheric disturbances (Carley et al., 2020). This is useful not only to space weather researchers

[1] http://www.lofar4sw.eu

but to the radio astronomy community as a whole as it will broaden our understanding of how space weather can effect the propagation of radio waves in the inner heliosphere and disturbances in the ionosphere and the effect this has on observing astronomical sources. In order to record the data streams from a LOFAR4SW-enabled international station in local mode, a backend such as REALTA will be required to capture the data-stream and to process the raw data so that it can be used by space weather researchers and forecasters. The effectiveness of machine learning algorithms to detect solar radio bursts with REALTA is currently being investigated.

In the future, REALTA will be upgraded to fully include the BL headnode into the system. In order to achieve this, additional VLAN fibre connections will be set up between the UCC compute nodes and the BL headnode and compute nodes. Activating these VLAN fibre connections will allow each machine to record one lane of data and perform real-time channelisation and dedispersion making use of their GPUs. The BL headnode will distribute an identical OS to the UCC and BL compute nodes and control them in parallel. This will allow REALTA to monitor for radio transients such as those important to SETI research. Upgrades to the data preparation and processing stages of the REALTA data flow (Figure 4.2) will see REALTA operating fully in real-time (see section 4.3.5).

7.2.2 On Observing Radio Bursts with TBBs.

One of the greatest unexplored potentials of solar radio astronomy is extremely high temporal variability of radio bursts. The LOFAR TBBs are capable of recording 5 seconds of raw sampled data from the antennas at 5 ns temporal resolution. The TBBs are an extremely powerful tool that allow one to recreate the LOFAR data processing pipeline entirely in software. Typically, the TBB buffer is frozen before all the data is read out to an external disk. This process is much slower than the 3.2 Gbps recording of RSP data and can take upwards of 40 minutes to read out 5 s of data from every TBB. Over the period September 2017 to March 2018 a method of continually reading from the TBBs in almost real-time was investigated. I assisted in the development of

this system and managed to record TBB data on a number of occasions. The data recorded during this time coincided with the solar minimum of solar cycle 24. Radio bursts occurred only once every few months and as such any data taken was essentially noise. Figure 7.6 shows 10 ms of noise recorded by the TBBs from LBA number 3 at I-LOFAR. Throughout my PhD the development of REALTA to record RSP data was a priority and as such, the possibility of a real-time readout of TBBs was not fully explored.

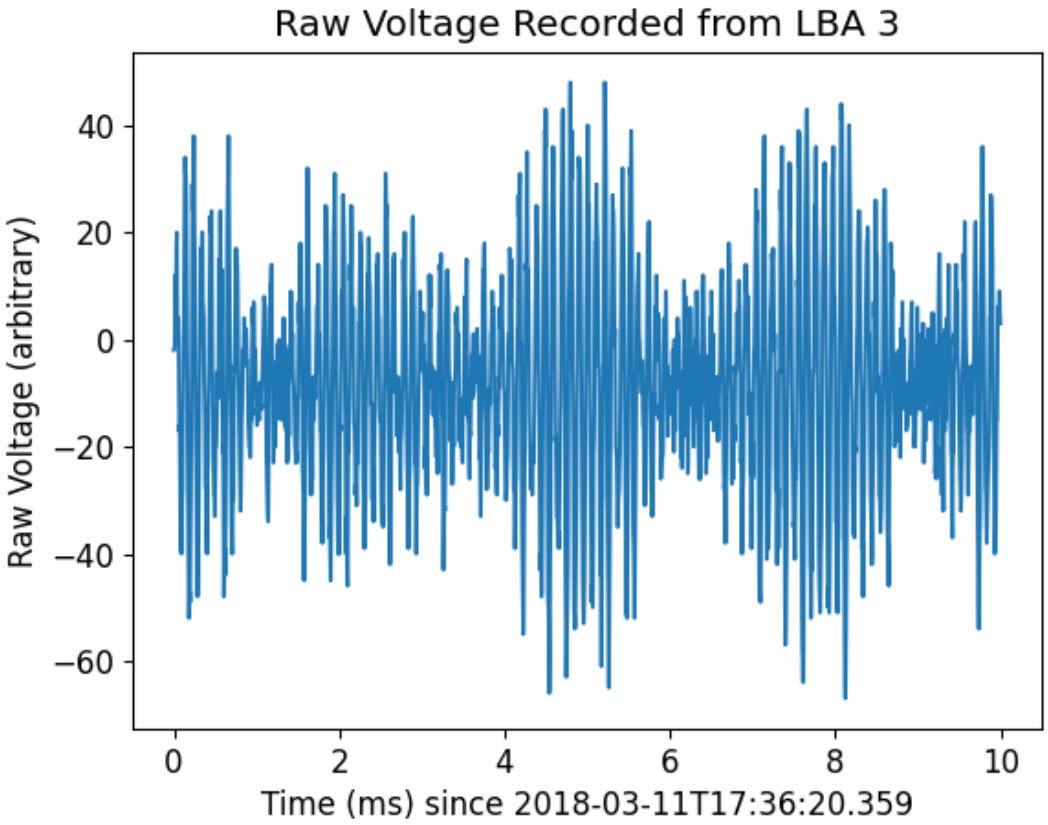

Figure 7.6: 10 ms of data recorded with TBBs from I-LOFAR, the data presented here is from LBA 3. The beating pattern is likely due to RFI.

TBB data gives one the freedom to recreate a radio telescope entirely in software. It also allows for some unique and ingenuitive signal processing steps. For example, the polyphase filter bank in an RSP takes 1024 time samples before performing a Fourier transform to obtain 512 subbands. This results in a dynamic spectrum with a temporal resolution of 5.12 μs and 195.3 kHz spectral resolution. Using TBB data it is possible to, instead, perform an FFT on the entire time series, window the resulting spectrum

with any desired frequency resolution and inverse FFT each to get a dynamic spectrum with 5 ns temporal resolution and the chosen spectral resolution.

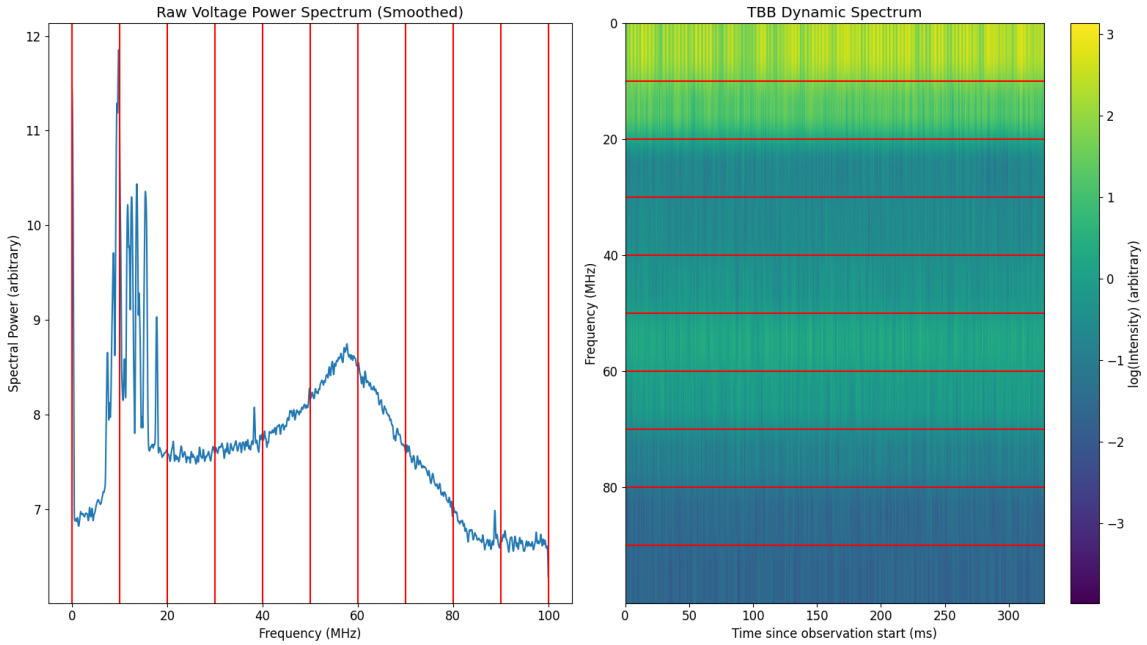

Figure 7.7: An example of creating a dynamic spectrum from TBB data. The left panel shows the (smoothed) power spectrum of an LBA. The vertical red lines mark the chosen subband edges. The right panel is a dynamic spectrum with a time resolution of 5ns and frequency resolution of $\sim$ 10 MHz as determined by the chosen number of subbands, whose edges are shown by the red horizontal lines.

This is implemented on the same TBB data as shown in Figure 7.6 to create the dynamic spectrum shown in Figure 7.7. The left panel shows the (smoothed) power spectrum of the time series with a number of vertical red lines which indicate the edges of chosen subbands. By performing an inverse Fourier transform on each subband, a dynamic spectrum with a temporal resolution of 5 ns can be created, shown in the right panel. Here, again, the red lines indicate the subband edges. Care must be taken to avoid spectral leakage between subbands. A common approach in avoiding this problem is to apply a window function to each subband. Because the subbands in Figure 7.7 are wide and the data is mostly noise, rectangular windows are appropriate in this case.

The ability to record dynamic spectra and retain the 5 ns temporal resolution of the raw LOFAR sampling means that, should they exist, extremely short duration pulsations in solar radio bursts could be studied. These timescales have been completely

unexplored to date and offer an exciting chance to push the forefront of solar radio astronomy. Observations at these timescales would allow for the search for fine temporal structure in radio bursts. Because the decay time of radio bursts is attributed to scattering (Krupar et al., 2020), it is likely that any inherent fine temporal structure will get "blurred out" before being observed. However, there has been no report in scientific literature of solar radio emission at this time scale and thus any such study opens the door into the domain of nanosecond observations of the Sun.

7.2.3 On the Automatic Classification of Radio Bursts.

One of the big challenges facing radio astronomy is the vast amounts of data produced during observations. I-LOFAR produces 3.2 gigabits of data per second meaning that a 5 hour observation can reach sizes of $\sim$ 7 TB. As such, observing the Sun for long durations and saving the entire raw dataset regardless of whether a radio burst occurred or not is impractical. An ideal solution would be to automatically determine if a burst has occurred before choosing to save data to disk. This is an ideal task for a machine learning (ML) algorithm, which are most commonly used for automatic classification. ML algorithms take thousands to billions of inputs which have been labelled in order to "learn" how to classify them. The classic example of ML automatic recognition is recognising handwritten numbers from the Modified National Institute of Standards and Technology database (MNIST; Lecun et al., 1998). Scully et al. (2021) recently showed promising results of using a particular ML algorithm, a convolutional neural network (CNN), to automatically detect and characterise type III radio bursts. They implement the YOLOv2 (You Only Look Once; Redmon & Farhadi, 2016) algorithm to detect type III bursts and place a bounding box that covers their time and frequency span. Figure 7.8 shows a dynamic spectrum with (left panel) and without (right panel) the intensity inverted and the bounding boxes detected by the CNN. Using a training dataset of simulated type III bursts, the algorithm was able to achieve an accuracy of 82.63% and can run on data in real-time.

Implementing this algorithm on REALTA and I-LOFAR would be an ideal test case

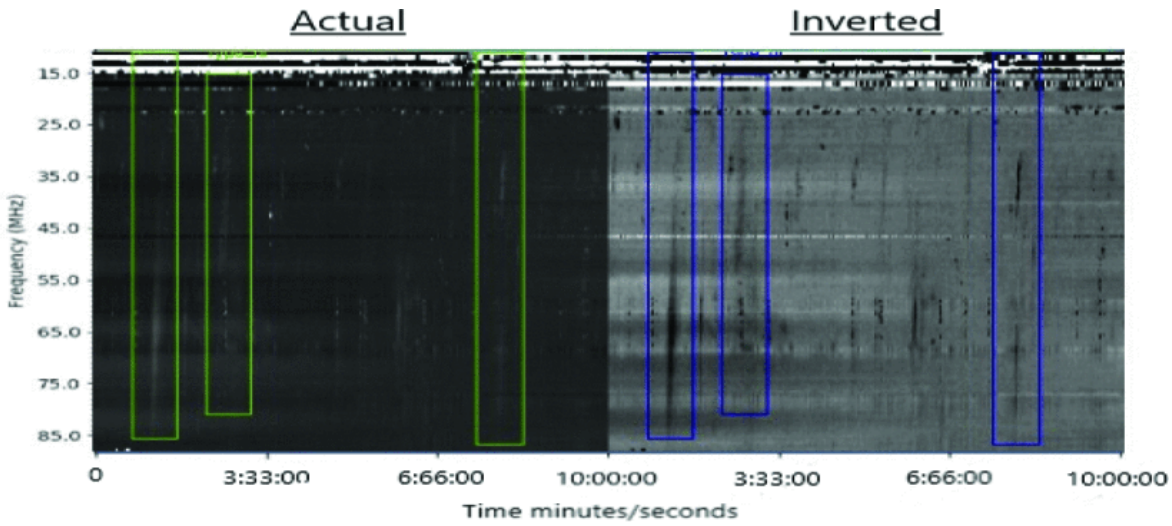

Figure 7.8: Automatically detected type III bursts using YOLO from Scully et al. (2021). Coloured boxes mark the regions detected by the algorithm to contain a type III burst. The colour bar has been inverted in the right panel in order to better display the type III bursts.

on real data in real-time, especially as we enter into the next solar cycle. Not only this, but, a detection from the algorithm could be used to trigger a readout of the TBBs. In their conclusions, Scully et al. (2021) outline some future developments that could improve their results. In particular, a more physical model of type III emission is necessary, rather than the simple morphological model presently used. There is approximately 20 TB of archival data recorded with REALTA many of which contain solar radio bursts. This data, along with simulated dynamic spectra, would provide an ideal training and test set which could improve the performance of the algorithm for I-LOFAR data. The use of ML algorithms in radio data analysis will become all the more important with the next generation of radio telescopes such as the SKA which are expected to drastically increase data rates.

7.2.4 On the Comparisons of Type IIIb Burst Observations and Simulations.

Type IIIb radio bursts are a subset of type III bursts that exhibit fine spectral features called striae or striations, see Section 1.4.1. The origin of these striations has not been conclusively determined. An early theory by Takakura & Yousef (1975) suggests that they are due to an electron beam passing through overdense regions in the solar corona.

Recently, Reid & Kontar (2021) presented simulations and observations of type IIIb radio bursts where they have determined how the striae fine structure is developed. Beam driven Langmuir wave modulation by turbulence in the solar corona and the spatial motion of these Langmuir waves due to a non-zero group velocity are both necessary in order to match simulations to observed dynamic spectra and account for individual striation frequency width and duration.

Following the results from this thesis, the effect radio wave scattering has on the size of type III bursts does not fully agree with scattering simulations (Chapter 6). As such, more work is necessary to determine the probable causes of this discrepancy. One possible avenue of investigation would be to perform a similar analysis to Chapter 6 for type IIIb bursts. By using Equation 1 in Reid & Kontar (2021), it would be possible to obtain a value of ε directly from the dynamic spectrum of a type IIIb burst. Coupling this together with the burst size would give a more qualitative comparison to scattering simulations than has been done previously. Figure 7.9 shows the peak flux of an observed type IIIb burst on 16 September 2015. The green curve shows the smoothed flux which is used to determine $\Delta I/I$ which can be used to infer a value for ε from Equation 1 of Reid & Kontar (2021) repeated here

$$\varepsilon = \frac{\langle \Delta n^2 \rangle}{n^2} = \left(\frac{v_{Th}^2}{v_b^2} \right)^2 \frac{\langle \Delta I^2 \rangle}{I^2} \tag{7.1}$$

A previous case study of a type IIIb - III pair (a fundamental-harmonic pair of type III bursts where the fundamental is a type IIIb and the harmonic a type III) was carried out by Zhang et al. (2020). They found that the fundamental and harmonic emission show different motion as can be seen in Figure 7.10 and attribute this to radio wave propagation effects.

To date there has been no comparison between a large number of type III and type IIIb bursts where both are emitting at the fundamental plasma frequency using interferometric observations. Applying a technique similar to the visibility fitting described elsewhere in this thesis to determine a characteristic size could be extremely useful in

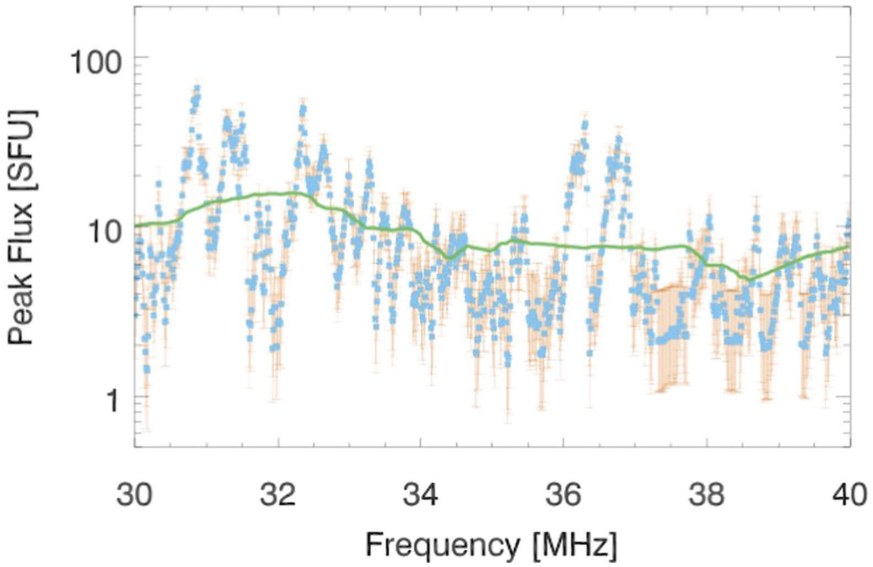

Figure 7.9: Peak flux of a type IIIb burst observed by Reid & Kontar (2021) on 16 September 2015. The blue points are the actual flux values while the green curve shows a smoothed flux determined using a Savitsky-Golay filter with a characteristic size of 3 MHz. The difference between the peak flux and the smoothed flux is used to calculate $\Delta I/I$ in Equation 7.1.

quantifying the level of turbulence necessary to generate type IIIb bursts. This is also an excellent opportunity to use *in-situ* data from Parker Solar Probe (PSP; Fox et al., 2016) and Solar Orbiter (Müller et al., 2020) to confirm the predictions made with remote measurements from LOFAR and other radio telescopes.

7.3 Concluding Remarks.

The research presented in this thesis is a study of the low radio frequency Sun at some of the highest temporal, spectral and spatial resolutions to date. Our knowledge of radio wave propagation in the solar corona has been expanded as a result and the potential for further study is great. Using a new method in the context of LOFAR solar observations that I developed, I determined that the large size observed for a type IIIb radio burst is due to radio wave scattering in the corona and that this effect may be over estimated by previous tied array imaging observations of the same. Following from this, I investigated the source size and position of 29 type III bursts using the same method. My conclusion from this is that the level of anisotropy of radio wave scattering is lower than first expected by simulations and that type III bursts have

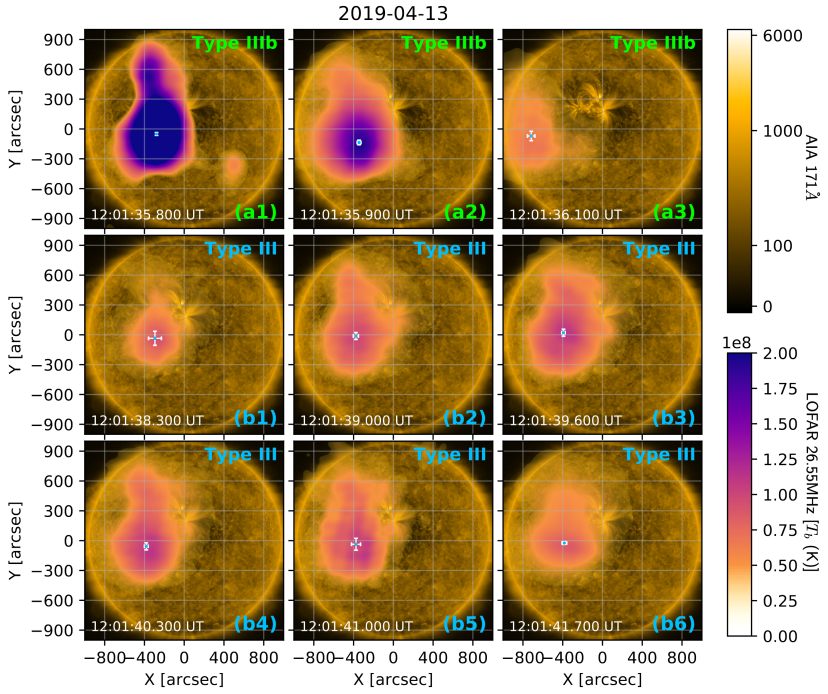

Figure 7.10: A type IIIb - III pair observed by Zhang et al. (2020). Panels a1-3 show the fundamental type IIIb burst observed with LOFAR and imaged using WSCLEAN. Panels b1-6 show the harmonic type III burst at a frequency of 26.56 MHz.

an intrinsic source size of the order of 10 arcmins. Parallel to this, I helped develop and install REALTA at I-LOFAR which has recorded numerous radio noise storms at 5.12 μs temporal resolution and 195.3 kHz spectral resolution.

With the upgrade to LOFAR2.0 and other next generation radio telescopes such as the Square Kilometre Array (SKA; McMullin et al., 2020) imminent, automatic detection of solar radio bursts will become all the more important. Machine learning algorithms have an important part to play in the automatic detection and classification of solar radio bursts in the near future. Until then, development of solar-specific calibration and imaging techniques can help maximise the quality of observations from modern day interferometers such as LOFAR.

There are many questions that remain unanswered about radio wave scattering in the corona, the most relevant to this thesis being why do scattering models not fully agree with observations? Recent advancements in the theory of fine structure generation in type IIIb bursts may bridge the gap between observations and simulations.

The work and research undertaken as part of this thesis has improved our under-

standing of and ability to observe and analyse solar radio emission. By combining the imaging technique developed during this thesis with *in-situ* measurements of coronal plasma, some of the long standing questions in radio wave propagation are bound to be answered.

References

Amiri, M., Andersen, B. C., Bandura, K. M., et al. 2020, Nature, 582, 351 (Cited on page 133.)

Amiri, M., Bandura, K., Berger, P., et al. 2018, The Astrophysical Journal, 863, 48 (Cited on page 132.)

Anantharamaiah, K. R., Gothoskar, P., & Cornwell, T. J. 1994, Journal of Astrophysics and Astronomy, 15, 387 (Cited on pages 103, 118, 120 and 121.)

Andersen, B. C., Bandura, K., Bhardwaj, M., et al. 2019, The Astrophysical Journal, 885, L24 (Cited on page 133.)

Appleton, E. & Hey, J. 1946, The London, Edinburgh, and Dublin Philosophical Magazine and Journal of Science, 37, 73 (Cited on page 10.)

Armstrong, J. W., Coles, W. A., Rickett, B. J., & Kojima, M. 1990, The Astrophysical Journal, 358, 685 (Cited on page 92.)

Arzner, K. & Magun, A. 1999, *Astronomy & Astrophysics*, 351, 1165 (Cited on pages 21, 42 and 109.)

Aschwanden, M. J. 2004, Physics of the Solar Corona. An Introduction (Cited on pages 3 and 5.)

Bartosz, P. D., Flisek, P., Blaszkiewicz, L., & Shevchuk, M. 2020, in Proceedings of the Polish Astronomical Society, Vol. 10, 49–51 (Cited on page 83.)

Bassa, C., Pleunis, Z., & Hessels, J. 2017, Astronomy and Computing, 18, 40 (Cited on page 79.)

Bastian, T. S. 1994, The Astrophysical Journal, 426, 774 (Cited on pages 20, 21, 105, 108 and 120.)

Benz, A. O., Monstein, C., & Meyer, H. 2005, Solar Physics, 226, 143 (Cited on page 16.)

Bhat, N. D. R., Cordes, J. M., & Chatterjee, S. 2003, The Astrophysical Journal, 584, 782 (Cited on page 131.)

Bian, N. H., Emslie, A. G., & Kontar, E. P. 2019, The Astrophysical Journal, 873, 33 (Cited on pages 21, 42, 105 and 109.)

Bigg, E. K. 1964, Nature, 203, 1008 (Cited on page 134.)

Bilous, A. V., Bondonneau, L., Kondratiev, V. I., et al. 2020, Astronomy & Astrophysics, 635, A75 (Cited on page 129.)

Bilous, A. V., Hessels, J. W. T., Kondratiev, V. I., et al. 2014, Astronomy & Astrophysics, 572, A52 (Cited on page 129.)

Bisoi, S. K., Janardhan, P., Ingale, M., et al. 2014, The Astrophysical Journal, 795, 69 (Cited on page 91.)

Blaszkiewicz, L., Lewandowski, W., Smierciak, B., et al. 2020, in Proceedings of the Polish Astronomical Society, Vol. 10, 46–48 (Cited on page 129.)

Boischot, A. 1957, Comptes Rendus de l'Académie des Sciences, Paris, 244, 1326 (Cited on pages 12 and 82.)

Bondonneau, L., Grießmeier, J.-M., Theureau, G., et al. 2021, Astronomy & Astrophysics, 652, A34 (Cited on page 72.)

Bondonneau, L., Grießmeier, J.-M., Theureau, G., & Serylak, M. 2017, Proceedings of the International Astronomical Union, 13, 313 (Cited on pages 72 and 129.)

Briggs, D. S. 1995, in American Astronomical Society, 187th AAS Meeting, id.112.02; Bulletin of the American Astronomical Society, Vol. 27, p.1444, Vol. 187, 112.02 (Cited on pages 69, 70 and 97.)

Broekema, P. C., Mol, J. J. D., Nijboer, R., et al. 2018, Astronomy and Computing, 23, 180 (Cited on page 72.)

Brueckner, G. E., Howard, R. A., Koomen, M. J., et al. 1995, Solar Physics, 162, 357 (Cited on page 5.)

Burke, B. F. & Franklin, K. L. 1955, Journal of Geophysical Research, 60, 213 (Cited on page 134.)

Carley, E., Cecconi, B., Reid, H., et al. 2021, in EGU General Assembly, EGU21–13113 (Cited on page 83.)

Carley, E. P., Baldovin, C., Benthem, P., et al. 2020, Journal of Space Weather and Space Climate, 10, 7 (Cited on page 140.)

Carley, E. P., Hayes, L. A., Murray, S. A., et al. 2019, Nature Communications, 10, 2276 (Cited on pages 87 and 128.)

Carley, E. P., Reid, H., Vilmer, N., & Gallagher, P. T. 2015, Astronomy & Astrophysics, 581, A100 (Cited on page 83.)

Chandrasekhar, S. 1952, Monthly Notices of the Royal Astronomical Society, 112, 475 (Cited on pages 20, 41, 42, 43 and 108.)

Chen, W., Barr, E., Karuppusamy, R., Kramer, M., & Stappers, B. 2021, arXiv e-prints, arXiv:2110.01667 (Cited on page 63.)

Chrysaphi, N., Kontar, E. P., Holman, G. D., & Temmer, M. 2018, The Astrophysical Journal, 868, 79 (Cited on pages 42, 103 and 105.)

Clark, B. G. 1980, *Astronomy & Astrophysics*, 89, 377 (Cited on page 66.)

Clarke, B. P., Morosan, D. E., Gallagher, P. T., et al. 2019, Astronomy & Astrophysics, 622, A204 (Cited on pages 15 and 128.)

Cliver, E. W. & Ling, A. G. 2009, The Astrophysical Journal, 690, 598 (Cited on page 12.)

Coles, W. A. & Harmon, J. K. 1989, The Astrophysical Journal, 337, 1023 (Cited on pages xvi, 21, 42, 92, 93 and 108.)

Condon, J. J. J. J. & Ransom, S. M. 2016, Essential radio astronomy (Princeton University Press), 361 (Cited on pages 60 and 65.)

Cornwell, T. J. 2008, IEEE Journal of Selected Topics in Signal Processing, 2, 793 (Cited on page 97.)

de Gasperin, F., Dijkema, T. J., Drabent, A., et al. 2019, Astronomy & Astrophysics, 622, A5 (Cited on pages 67, 95 and 103.)

de La Noe, J. 1975, Astronomy and Astrophysics, 43, 201 (Cited on page 91.)

de La Noe, J. & Boischot, A. 1972, Astronomy and Astrophysics, 20, 55 (Cited on page 91.)

Dewdney, P., Hall, P., Schilizzi, R., & Lazio, T. 2009, Proceedings of the IEEE, 97, 1482 (Cited on page 92.)

Donner, J. Y., Verbiest, J. P. W., Tiburzi, C., et al. 2019, Astronomy & Astrophysics, 624, A22 (Cited on pages 72 and 129.)

Driessen, L. N., Janssen, G. H., Bassa, C. G., Stappers, B. W., & Stinebring, D. R. 2019, Monthly Notices of the Royal Astronomical Society, 483, 1224 (Cited on page 131.)

Eastwood, J. P., Biffis, E., Hapgood, M. A., et al. 2017, Risk Analysis, 37, 206 (Cited on page 10.)

Edler, H. W., de Gasperin, F., & Rafferty, D. 2021, Astronomy & Astrophysics, 652, A37 (Cited on page 87.)

Ellis, G. 1969, Australian Journal of Physics, 22, 177 (Cited on pages 15, 83 and 91.)

Ellis, G. & McCulloch, P. 1967, Australian Journal of Physics, 20, 583 (Cited on pages 83 and 91.)

Enriquez, J. E., Siemion, A., Foster, G., et al. 2017, The Astrophysical Journal, 849, 104 (Cited on page 136.)

Fokker, A. D. 1965, Bulletin of the Astronomical Institutes of the Netherlands, 18, 111 (Cited on pages 20, 41, 42, 90, 107 and 108.)

Foreman-Mackey, D., Hogg, D. W., Lang, D., & Goodman, J. 2013, Publications of the Astronomical Society of the Pacific, 125, 306 (Cited on page 114.)

Foukal, P. V. 2013, Solar Astrophysics, 3rd, Revised Edition, 480 (Cited on page 2.)

Fox, N. J., Velli, M. C., Bale, S. D., et al. 2016, Space Science Reviews, 204, 7 (Cited on pages 22, 46, 91 and 147.)

Gajjar, V., Siemion, A., Croft, S., et al. 2019, in Bulletin of the American Astronomical Society, Vol. 51, 223 (Cited on page 136.)

Ginzburg, V. L. & Zhelezniakov, V. V. 1958, Astronomicheskii Zhurnal, 35, 694 (Cited on pages 16, 39 and 83.)

Goodman, J. & Weare, J. 2010, Communications in Applied Mathematics and Computational Science, 5, 65 (Cited on page 114.)

Gopalswamy, N. & Thompson, B. 2000, Journal of Atmospheric and Solar-Terrestrial Physics, 62, 1457 (Cited on page 10.)

Gordovskyy, M., Kontar, E., Browning, P., & Kuznetsov, A. 2019, The Astrophysical Journal, 873, 48 (Cited on pages 90 and 105.)

Hankins, T. H. & Rajkowski, J. M. 1987, Review of Scientific Instruments, 58, 674 (Cited on page 79.)

Hare, B. M., Scholten, O., Bonardi, A., et al. 2018, Journal of Geophysical Research (Atmospheres), 123, 2861 (Cited on page 51.)

Hermsen, W., Kuiper, L., Basu, R., et al. 2018, Monthly Notices of the Royal Astronomical Society, 480, 3655 (Cited on pages 73 and 129.)

Hess, S., Mottez, F., & Zarka, P. 2009, Geophysical Research Letters, 36, L14101 (Cited on page 135.)

Hess, S., Zarka, P., & Mottez, F. 2007, Planetary and Space Science, 55, 89 (Cited on page 135.)

Högbom, J. A. 1974, Astronomy & Astrophysics Supplemental, 15, 417 (Cited on pages 65 and 97.)

Hollweg, J. 1967, PhD thesis (Cited on page 42.)

Hotan, A. W., van Straten, W., & Manchester, R. N. 2004, Publications of the Astronomical Society of Australia, 21, 302 (Cited on page 80.)

Hurford, G. J., Schmahl, E. J., Schwartz, R. A., et al. 2002, Solar Physics, 210, 61 (Cited on page 97.)

Inan, U. S. & Golkowski, M. 2010, Principles of Plasma Physics for Engineers and Scientists, Vol. 9780521193 (Cambridge: Cambridge University Press), 1–270 (Cited on page 31.)

Ingale, M., Subramanian, P., & Cairns, I. 2015, Monthly Notices of the Royal Astronomical Society, 447, 3486 (Cited on page 103.)

Isaacson, H., Siemion, A. P., Marcy, G. W., et al. 2017, Publications of the Astronomical Society of the Pacific, 129, 054501 (Cited on page 136.)

Jameson, A. & van Straten, W. 2008, PSRDADA: Data Acquisition and Distributed Analysis Software (Cited on page 87.)

Johnston, S., Taylor, R., Bailes, M., et al. 2008, Experimental Astronomy, 22, 151 (Cited on page 71.)

Jonas, J. 2018, in Proceedings of MeerKAT Science: On the Pathway to the SKA — PoS(MeerKAT2016) (Trieste, Italy: Sissa Medialab), 001 (Cited on page 71.)

Karako-Argaman, C., Kaspi, V. M., Lynch, R. S., et al. 2015, The Astrophysical Journal, 809, 67 (Cited on page 132.)

Karastergiou, A., Chennamangalam, J., Armour, W., et al. 2015, Monthly Notices of the Royal Astronomical Society, 452, 1254 (Cited on pages 72 and 133.)

Karuppusamy, R., Stappers, B. W., & Lee, K. J. 2012, Astronomy and Astrophysics, 538, A7 (Cited on page 130.)

Keane, E. F. 2018, Nature Astronomy, 2, 865 (Cited on page 82.)

Keane, E. F., Kramer, M., Lyne, A. G., et al. 2011, Monthly Notices of the Royal Astronomical Society, 415, 3065 (Cited on page 132.)

Kolmogorov, A. 1941, Akademiia Nauk SSSR Doklady, 30, 301 (Cited on pages 21 and 108.)

Kolotkov, D. Y., Nakariakov, V. M., & Kontar, E. P. 2018, The Astrophysical Journal, 861, 33 (Cited on page 83.)

Kontar, E. P., Chen, X., Chrysaphi, N., et al. 2019, The Astrophysical Journal, 884, 122 (Cited on pages 20, 21, 43, 90, 91, 92, 103, 104, 105, 109, 110, 120, 121, 122, 123, 124 and 139.)

Kontar, E. P., Hannah, I. G., Jeffrey, N. L. S., & Battaglia, M. 2010, The Astrophysical Journal, 717, 250 (Cited on page 97.)

Kontar, E. P., Yu, S., Kuznetsov, A. A., et al. 2017, Nature Communications, 8, 1515 (Cited on pages xv, 18, 19, 20, 89, 90, 91, 92, 94, 102, 104, 109, 120 and 140.)

Krupar, V., Maksimovic, M., Kontar, E. P., et al. 2018, The Astrophysical Journal, 857, 82 (Cited on pages 90 and 91.)

Krupar, V., Szabo, A., Maksimovic, M., et al. 2020, The Astrophysical Journal Supplement Series, 246, 57 (Cited on pages 91 and 144.)

Lebofsky, M., Croft, S., Siemion, A. P., et al. 2019, Publications of the Astronomical Society of the Pacific, 131, 124505 (Cited on page 80.)

Lecun, Y., Bottou, L., Bengio, Y., & Haffner, P. 1998, Proceedings of the IEEE, 86, 2278 (Cited on page 144.)

Lemen, J. R., Title, A. M., Akin, D. J., et al. 2012, Solar Physics, 275, 17 (Cited on pages 5 and 99.)

Lonsdale, C. J., Cappallo, R. J., Morales, M. F., et al. 2009, Proceedings of the IEEE, 97, 1497 (Cited on pages 10, 71, 72 and 92.)

Lorimer, D. 2011, SIGPROC: Pulsar Signal Processing Programs http://ascl.net/1107.016 (Cited on page 79.)

Lorimer, D. R., Bailes, M., McLaughlin, M. A., Narkevic, D. J., & Crawford, F. 2007, Science, 318, 777 (Cited on pages 80 and 133.)

Louarn, P., Allegrini, F., McComas, D. J., et al. 2017, Geophysical Research Letters, 44, 4439 (Cited on page 134.)

Lubberhuizen, W. & Kooistra, E. 2009, RSP - CEP Beamlet Data Interface. Technical Report LOFAR-ASTRON-SDD-009, Tech. rep. (Cited on page 73.)

Lyne, A. G., Jordan, C. A., Graham-Smith, F., et al. 2015, Monthly Notices of the Royal Astronomical Society, 446, 857 (Cited on page 129.)

Maguire, C. A., Carley, E. P., McCauley, J., & Gallagher, P. T. 2020, Astronomy & Astrophysics, 633, A56 (Cited on pages 55, 82 and 83.)

Maguire, C. A., Carley, E. P., Zucca, P., Vilmer, N., & Gallagher, P. T. 2021, *Astrophysical Journal*, 909, 2 (Cited on page 69.)

Manchester, R. N. 2017, Journal of Physics: Conference Series, 932, 012002 (Cited on page 82.)

Mann, G. 1995, in Lecture Notes in Physics, Berlin Springer Verlag, Vol. 444, Coronal Magnetic Energy Releases, ed. A. Benz & A. Krüger, 183 (Cited on page 13.)

Marques, M. S., Zarka, P., Echer, E., et al. 2017, Astronomy and Astrophysics, 604 (Cited on page 135.)

McConnell, D. 1980, Publications of the Astronomical Society of Australia, 4, 64 (Cited on pages 12, 15 and 20.)

McKay-Bukowski, D., Vierinen, J., Virtanen, I. I., et al. 2015, IEEE Transactions on Geoscience and Remote Sensing, 53, 1440 (Cited on page 54.)

McKee, J. W., Lyne, A. G., Stappers, B. W., Bassa, C. G., & Jordan, C. A. 2018, Monthly Notices of the Royal Astronomical Society, 479, 4216 (Cited on page 131.)

McKenna, D. 2020, David-McKenna/udpPacketManager: 0.5.0 – Limit Processed Beamlets, Add Test Cases, Numerous Small Fixes/QOL https://github.com/David-McKenna/udpPacketManager (Cited on page 78.)

McLaughlin, M. A., Lyne, A. G., Lorimer, D. R., et al. 2006, Nature, 439, 817 (Cited on page 80.)

McLean, D. J. & Labrum, N. R. 1985, Solar radiophysics: Studies of emission from the sun at metre wavelengths (Cited on pages 2, 4, 13, 14, 15, 16, 18, 38, 39 and 90.)

McMullin, J. P., Diamond, P. J., McPherson, A. M., et al. 2020, in Ground-based and Airborne Telescopes VIII, ed. H. K. Marshall, J. Spyromilio, & T. Usuda, Vol. 11445 (SPIE), 243 (Cited on pages 10, 72 and 148.)

Melnik, V. N., Konovalenko, A. A., Rucker, H. O., et al. 2010a, Solar Physics, 264, 103 (Cited on pages 15 and 83.)

Melnik, V. N., Rucker, H. O., Konovalenko, A. A., et al. 2010b, in AIP Conference Proceedings, Vol. 1206, 445–449 (Cited on page 91.)

Melrose, D. B. 1982, Solar Radio Storms, CESRA Workshop #4, 182 (Cited on page 12.)

Melrose, D. B. 1987, Solar Physics, 111, 89 (Cited on pages 37, 39 and 83.)

Mereghetti, S., Kuiper, L., Tiengo, A., et al. 2016, The Astrophysical Journal, 831, 21 (Cited on pages 73 and 129.)

Meyers, B. W., Tremblay, S. E., Bhat, N. D. R., et al. 2017, The Astrophysical Journal, 851, 20 (Cited on pages 129, 130 and 131.)

Michilli, D., Bassa, C., Cooper, S., et al. 2020, Monthly Notices of the Royal Astronomical Society, 491, 725 (Cited on page 132.)

Michilli, D., Hessels, J. W. T., Donner, J. Y., et al. 2018, Monthly Notices of the Royal Astronomical Society, 476, 2704 (Cited on page 73.)

Mickaliger, M. B., Stappers, B. W., Bassa, C. G., & Fletcher, A. G. 2017, Proceedings of the International Astronomical Union, 13, 380 (Cited on page 131.)

Mondal, S., Mohan, A., Oberoi, D., et al. 2019, *Astrophysical Journal*, 875, 97 (Cited on page 67.)

Mondal, S., Oberoi, D., & Mohan, A. 2020, The Astrophysical Journal, 895, L39 (Cited on page 83.)

Morosan, D. E., Gallagher, P. T., Zucca, P., et al. 2014, Astronomy & Astrophysics, 568, A67 (Cited on page 89.)

Morosan, D. E., Gallagher, P. T., Zucca, P., et al. 2015, Astronomy & Astrophysics, 580, A65 (Cited on pages 15 and 128.)

Morosan, D. E., Kilpua, E. K. J., Carley, E. P., & Monstein, C. 2019, Astronomy & Astrophysics, 623, A63 (Cited on pages 82, 83 and 89.)

Müller, D., Cyr, O. C. S., Zouganelis, I., et al. 2020, Astronomy & Astrophysics, 642, A1 (Cited on pages 22, 46, 106 and 147.)

Müller, D., Marsden, R. G., St. Cyr, O. C., & Gilbert, H. R. 2013, Solar Physics, 285, 25 (Cited on page 106.)

Mulrey, K., Buitink, S., Corstanje, A., et al. 2020, Journal of Cosmology and Astroparticle Physics, 2020, 017 (Cited on page 51.)

Murphy, P. C., Callanan, P., McCauley, J., et al. 2021, arXiv e-prints, arXiv:2108.11251 (Cited on pages 71, 127, 128 and 140.)

Murphy, P. C., Carley, E. P., Ryan, A. M., Zucca, P., & Gallagher, P. T. 2021, Astronomy and Astrophysics, 645, A11 (Cited on pages 83, 89, 110, 120, 126, 127 and 138.)

Nelson, G. & Melrose, D. 1985, in Solar Radiophysics: Studies of Emission from the Sun at Metre Wavelengths, ed. D. McLean & N. Labrum, 333–359 (Cited on pages 12, 13 and 14.)

Newkirk, G. 1961, The Astrophysical Journal, 133, 983 (Cited on pages 16, 42 and 102.)

Newville, M., Stensitzki, T., Allen, D. B., & Ingargiola, A. 2014 (Cited on page 98.)

Nita, G. M. & Gary, D. E. 2010, Publications of the Astronomical Society of the Pacific, 122, 595 (Cited on page 80.)

Noutsos, A., Sobey, C., Kondratiev, V. I., et al. 2015, Astronomy & Astrophysics, 576, A62 (Cited on page 129.)

Offringa, A. R., McKinley, B., Hurley-Walker, N., et al. 2014, Monthly Notices of the Royal Astronomical Society, 444, 606 (Cited on page 97.)

Offringa, A. R. & Smirnov, O. 2017, Monthly Notices of the Royal Astronomical Society, 471, 301 (Cited on pages 69 and 97.)

Parker, E. N. 1960, The Astrophysical Journal, 132, 821 (Cited on page 109.)

Pastor-Marazuela, I., Connor, L., van Leeuwen, J., et al. 2021, Nature, 596, 505 (Cited on page 133.)

Pick, M. & Vilmer, N. 2008, Astronomy and Astrophysics Review, 16, 1 (Cited on page 82.)

Pleunis, Z., Michilli, D., Bassa, C. G., et al. 2021, The Astrophysical Journal Letters, 911, L3 (Cited on page 133.)

Porayko, N. K., Noutsos, A., Tiburzi, C., et al. 2019, Monthly Notices of the Royal Astronomical Society, 483, 4100 (Cited on page 72.)

Postel, J. 1980, Internet Protocol, RFC 768, USC/Information Sciences Institute (Cited on page 73.)

Rajwade, K., Seymour, A., Lorimer, D. R., et al. 2016, Monthly Notices of the Royal Astronomical Society, 462, 2518 (Cited on page 72.)

Ransom, S. M. 2001, PhD thesis, Harvard University (Cited on page 80.)

Redmon, J. & Farhadi, A. 2016, YOLO9000: Better, Faster, Stronger (Cited on page 144.)

Reid, H. A. S. & Kontar, E. P. 2010, The Astrophysical Journal, 721, 864 (Cited on page 91.)

Reid, H. A. S. & Kontar, E. P. 2017, Astronomy & Astrophysics, 606, A141 (Cited on pages 20 and 89.)

Reid, H. A. S. & Kontar, E. P. 2018, Astronomy & Astrophysics, 614, A69 (Cited on page 86.)

Reid, H. A. S. & Kontar, E. P. 2021, Nature Astronomy, 5, 796 (Cited on pages xvi, 12, 18, 83, 146 and 147.)

Reid, H. A. S. & Ratcliffe, H. 2014, Research in Astronomy and Astrophysics, 14, 773 (Cited on pages 16, 18, 20, 37, 38, 90 and 98.)

Reiner, M., Kaiser, M., Fainberg, J., Bougeret, J.-L., & Stone, R. 1997, in ESA Special Publication, Vol. 415, Correlated Phenomena at the Sun, in the Heliosphere and in Geospace, ed. A. Wilson, 183 (Cited on page 14.)

Riddle, A. C. 1974, Solar Physics, 35, 153 (Cited on pages 41 and 90.)

Ryan, A. M., Gallagher, P. T., Carley, E. P., et al. 2021, *Astronomy & Astrophysics*, 648, A43 (Cited on pages 7 and 69.)

Sanidas, S., Cooper, S., Bassa, C. G., et al. 2019, Astronomy & Astrophysics, 626, A104 (Cited on page 132.)

Sasikumar Raja, K., Ingale, M., Ramesh, R., et al. 2016, Journal of Geophysical Research: Space Physics, 121, 11,605 (Cited on pages 91, 118 and 120.)

Scaife, A. M. M. 2020, Philosophical Transactions of the Royal Society A: Mathematical, Physical and Engineering Sciences, 378 (Cited on page 72.)

Schoonderbeek, G. W., Szomoru, A., Gunst, A. W., Hiemstra, L., & Hargreaves, J. 2019, Journal of Astronomical Instrumentation, 08, 1950003 (Cited on page 140.)

Schwab, F. R. 1984, *Astronomical Journal*, 89, 1076 (Cited on page 66.)

Scully, J., Flynn, R., Carley, E., Gallagher, P., & Daly, M. 2021, in 2021 32nd Irish Signals and Systems Conference (ISSC) (IEEE), 1–6 (Cited on pages 82, 144 and 145.)

Serylak, M., Karastergiou, A., Williams, C., Armour, W., & Giles, M. 2012, in Proceedings of the International Astronomical Union No. S291, 492–494 (Cited on page 72.)

Sharma, R. & Oberoi, D. 2020, The Astrophysical Journal, 903, 126 (Cited on pages 105 and 109.)

Sharykin, I. N., Kontar, E. P., & Kuznetsov, A. A. 2018, Solar Physics, 293, 115 (Cited on pages 18, 83 and 90.)

Smerd, S., Sheridan, K., & Stewart, R. 1974, in IAU Symposium, Vol. 57, Coronal Disturbances, ed. G. Newkirk, 389 (Cited on page 13.)

Stansby, D., Yeates, A., & Badman, S. T. 2020, Journal of Open Source Software, 5, 2732 (Cited on page 117.)

Stappers, B. W., Hessels, J. W. T., Alexov, A., et al. 2011, Astronomy & Astrophysics, 530, A80 (Cited on page 129.)

Steinberg, J. L., Aubier-Giraud, M., Leblanc, Y., & Boischot, A. 1971, Astronomy and Astrophysics, 10, 362 (Cited on pages 20, 41, 42, 90 and 108.)

Stewart, R. T. 1972, Publications of the Astronomical Society of Australia, 2, 100 (Cited on pages 90 and 108.)

Suzuki, S., Stewart, R. T., & Magun, A. 1980, Symposium - International Astronomical Union, 86, 241 (Cited on page 14.)

Takakura, T. & Yousef, S. 1975, Solar Physics, 40, 421 (Cited on pages 91, 102 and 145.)

Tan, C. M., Bassa, C. G., Cooper, S., et al. 2020, Monthly Notices of the Royal Astronomical Society, 492, 5878 (Cited on page 132.)

Tarter, J. 2001, Annual Review of Astronomy and Astrophysics, 39, 511 (Cited on page 80.)

Taylor, G. B., Carilli, C. L., & Perley, R. A. 1999, in Astronomical Society of the Pacific Conference Series, Vol. 180, Synthesis Imaging in Radio Astronomy II (Cited on page 58.)

ter Veen, S., Enriquez, J. E., Falcke, H., et al. 2019, Astronomy & Astrophysics, 621, A57 (Cited on page 133.)

Thejappa, G. & MacDowall, R. J. 2008, The Astrophysical Journal, 676, 1338 (Cited on pages 20, 90 and 105.)

Thejappa, G., MacDowall, R. J., & Kaiser, M. L. 2007, The Astrophysical Journal, 671, 894 (Cited on pages 20, 42, 90 and 108.)

Thornton, D., Stappers, B., Bailes, M., et al. 2013, Science, 341, 53 (Cited on page 80.)

Tian, H. 2017, Research in Astronomy and Astrophysics, 17, 110 (Cited on page 5.)

Tiburzi, C., Verbiest, J. P. W., Shaifullah, G. M., et al. 2019, Monthly Notices of the Royal Astronomical Society, 487, 394 (Cited on page 72.)

Treumann, R. A. 2006, The Astronomy and Astrophysics Review, 13, 229 (Cited on page 134.)

Turner, J. D., Grießmeier, J.-M., Zarka, P., & Vasylieva, I. 2019, Astronomy & Astrophysics, 624, A40 (Cited on page 135.)

Turner, J. D., Zarka, P., Grießmeier, J.-M., et al. 2021, Astronomy & Astrophysics, 645, A59 (Cited on page 135.)

van Diepen, G., Dijkema, T. J., & Offringa, A. 2018, ascl, ascl:1804.003 (Cited on pages 67 and 95.)

van Haarlem, M. P., Wise, M. W., Gunst, A. W., et al. 2013, Astronomy & Astrophysics, 556, A2 (Cited on pages 10, 45, 52, 53, 72, 82, 90 and 136.)

Van Leeuwen, J., Mikhailov, K., Keane, E., et al. 2020, Astronomy and Astrophysics, 634, A3 (Cited on page 130.)

van Straten, W. & Bailes, M. 2011, Publications of the Astronomical Society of Australia, 28, 1 (Cited on page 79.)

Vedenov, A. A. 1963, Journal of Nuclear Energy. Part C, Plasma Physics, Accelerators, Thermonuclear Research, 5, 169 (Cited on page 37.)

Virtanen, I. I. 2018, ASTRON document LOFAR-ASTRON-MAN-064, 51 (Cited on page 73.)

Virtanen, P., Gommers, R., Oliphant, T. E., et al. 2020, Nature Methods, 17, 261 (Cited on page 112.)

Voronkov, M. 2020, EPJ Web of Conferences, 245, 01038 (Cited on page 72.)

Vršnak, B., Magdalenić, J., Aurass, H., & Mann, G. 2002, Astronomy & Astrophysics, 396, 673 (Cited on page 13.)

Wild, J. 1950a, Australian Journal of Scientific Research A Physical Sciences, 3, 541 (Cited on page 121.)

Wild, J., Murray, J., & Rowe, W. 1954, Australian Journal of Physics, 7, 439 (Cited on page 16.)

Wild, J. P. 1950b, Australian Journal of Chemistry, 3, 399 (Cited on page 121.)

Wild, J. P. & McCready, L. L. 1950, Australian Journal of Scientific Research A, vol. 3, p.387, 3, 387 (Cited on pages 12 and 82.)

Wild, J. P., Sheridan, K. V., & Trent, G. H. 1959, URSI Symp. 1: Paris Symposium on Radio Astronomy, 9, 176 (Cited on pages 12 and 82.)

Woo, R., Armstrong, J. W., Bird, M. K., & Pätzold, M. 1995, Geophysical Research Letters, 22, 329 (Cited on page 92.)

Worden, S. P., Drew, J., Siemion, A., et al. 2017, Acta Astronautica, 139, 98 (Cited on page 136.)

Wu, C. 1985, Space Science Reviews, 41, 215 (Cited on page 134.)

Wu, C. S. & Lee, L. C. 1979, The Astrophysical Journal, 230, 621 (Cited on page 134.)

Wucknitz, O. 2019, in Proceedings of 14th European VLBI Network Symposium & Users Meeting — PoS(EVN2018), Vol. 344 (Trieste, Italy: Sissa Medialab), 017 (Cited on page 82.)

Zarka, P. 1998, Journal of Geophysical Research: Planets, 103, 20159 (Cited on page 134.)

Zhang, P., Wang, C., & Kontar, E. P. 2021, *Astrophysical Journal*, 909, 195 (Cited on pages 43, 122, 123, 124 and 139.)

Zhang, P., Zucca, P., Sridhar, S. S., et al. 2020, Astronomy & Astrophysics, 639, A115 (Cited on pages xvi, 83, 86, 109, 120, 146 and 148.)

Zucca, P., Carley, E. P., McCauley, J., et al. 2012, Solar Physics, 280, 591 (Cited on pages xv, 16 and 17.)

Zucca, P., Morosan, D. E., Rouillard, A. P., et al. 2018, Astronomy & Astrophysics, 615, A89 (Cited on page 89.)